Non-Adiabatic Ion Acceleration caused by Electromagnetic Waves (Cluster and Double Star observations) and Geomagnetic Field Response to the Variations of the Solar Wind Dynamic Pressure

Zhiqiang Wang

Université de Toulouse

THÈSE

En vue de l'obtention du

DOCTORAT DE L'UNIVERSITÉ DE TOULOUSE

Délivré par :
Université Toulouse 3 Paul Sabatier (UT3 Paul Sabatier)

Cotutelle internationale avec :
National Space Science Center (NSSC), Chinese Academy of Sciences (CAS)

Présentée et soutenue par :
Zhiqiang WANG
Le mardi 19 février 2013

Titre :
Accélération Non Adiabatique des Ions causée par des Ondes électromagnétiques (Observations de Cluster et Double Star) et réponse du champ géomagnétique aux variations de la pression dynamique du vent solair

---

ED SDU2E : Astrophysique, Sciences de l'Espace, Planétologie

Unité de recherche :
Institut de Recherche en Astrophysique et Planetologie (IRAP) - CNRS

Directeur(s) de Thèse :

Prof. Henri REME, Prof. Jinbin CAO

Rapporteurs :

Prof. Dominique DELCOURT, Prof. Chao SHEN

Autre(s) membre(s) du jury :

Prof. Henri REME, Prof. Jinbin CAO, Dr. Iannis DANDOURAS, Prof. Dominique DELCOURT, Prof. Aimin DU, Prof. Chao SHEN (President)

Accélération Non Adiabatique des Ions causée par des Ondes électromagnétiques (Observations de Cluster et Double Star) et réponse du champ géomagnétique aux variations de la pression dynamique du vent solaire

Non-Adiabatic Ion Acceleration caused by Electromagnetic Waves (Cluster and Double Star observations) and Geomagnetic Field Response to the Variations of the Solar Wind Dynamic Pressure

par/by Zhiqiang WANG

Acknowledgements

It would not have been possible to write this doctoral thesis without the help and support of many people around me. I would like to express my sincere gratitude to all of them.

I am extremely grateful to my research supervisor Professor Henri Rème. During the time when I was in France, he not only gave me much guidance in my research subject, but also took very care of my daily life. His kindness and enthusiasm make my study in France to be a very comfortable and pleasant memory. I also express my sincere gratitude to Dr. Iannis Dandouras. His advises greatly help me to finish my research, and his erudition and amicability impressed me a lot. I was quite honored to work with them.

I would also like to give a heartfelt thanks to my supervisor in China Professor Jin-bin Cao for all of his guidance and support to my research. He leaded me to the research field of space science, and supplied many good opportunities for me. Without his help, this dissertation could not be finished.

I also appreciate the valuable advises from Dr. Dominique Delcourt, and the help from Dr. Christian Mazelle, Dr. Sandrine Grimald, Mr. Emmanuel PENOU who have developed the cl software and many other colleagues in IRAP. I am also thankful to the faculty members in CSSAR, Dr. Liuyuan Li, Dr. Yuduan Ma, Dr. Xinhua Wei, Dr. Junying Yang, Dr. Huishan Fu, Weizhen Ding, Aiying Duan, and Dong Zhang.

Thanks for the scholarship of ‘Joint Doctoral Promotion Programme’ between China and France funded by the Chinese Academy of Sciences (CAS) to financially support my study in France, as well as the support from IRAP/CNRS.

I am thankful to CROUS of Toulouse for supplying my accommodation in France, and the members in the office of graduate student in CSSAR, Teacher Zuohe Zhang, Yanqiu Li and Henan Xu for their countless effort to assist my student life.

Finally, I give my deepest thanks to my parents. They create a good environment for me to grow up and encourage me whenever I was in frustration. Their love is the solid foundation for my progress each day. Thank you with all my heart and soul.

Table des matières/Table of contents

Résumé

Cette thèse comporte deux thèmes principaux: l'un concerne l'accélération non adiabatique des ions dans la couche de plasma proche de la Terre, l'autre les pulsations géomagnétiques dues à la décroissance de la pression dynamique du vent solaire.

L'accélération nonadiabatique des ions de la couche de plasma est importante pour comprendre la formation du courant annulaire et les injections énergétiques des sous-orages. Dans la première partie de cette thèse, nous présentons des études de cas d'accélération non adiabatique des ions de la couche de plasma observés par Cluster et TC-1 Double Star dans la queue magnétique proche de la Terre (par exemple à (X, Y, Z)=(-7.7, 4.6, 3.0) R_T lors de l'évènement du 30 octobre 2006), beaucoup plus près de la Terre que ceux qui avaient été précédemment observés. Nous trouvons que les variations du flux d'énergie des ions, qui sont caractérisées par une décroissance entre 10 eV et 20 keV et une augmentation entre 28 keV et 70 keV, sont causées par l'accélération non adiabatique des ions associée étroitement avec les fortes fluctuations du champ électromagnétique autour de la gyrofréquence des ions H^+. Nous trouvons aussi que les ions après l'accélération non adiabatique sont groupés en phase de gyration et c'est la première fois que ceci est trouvé dans la couche de plasma alors que cet effet a été observé dans le vent solaire dans les années 1980. Nous interprétons les variations de flux d'énergie des ions et les groupements en phase de gyration en utilisant un modèle non adiabatique. Les résultats analytiques et les spectres simulés sont en bon accord avec les observations. Cette analyse suggère que cette acceleration nonadiabatique associée aves les fluctuations du cham magnétique est un mécanisme efficace pour l'accélération des ions dans la couche de plasma proche de la Terre. Les structures de flux d'énergie présentées peuvent être uilisées comme un proxy pour identifier ce processus dynamique.

Dans le deuxième thème, nous étudions la réponse du champ géomagnétique à une impulsion de la pression dynamique (P_{sw}) du vent solaire qui a atteint la

magnétosphère le 24 août 2005. En utilisant les données du champ géomagnétique à haute résolution fournies par 15 stations au sol et les données des satellites Geotail, TC-1 et TC-2, nous avons étudié les pulsations géomagnétiques aux latitudes aurorales dues à la décroissance brusque de P_{sw} dans la limite arrière de l'impulsion. Les résultats montrent que la décroissance brutale de P_{sw} peut exciter une pulsation globale dans la gamme de fréquence 4.3-11.6 mHz. L'inversion des polarisations entre deux stations des latitudes aurorales, la densité spectrale de puissance (PSD) plus grande près de la latitude de résonance et la fréquence augmentant avec la diminution de la latitude indiquent que les pulsations sont associées avec la résonance des lignes de champ (FLR). La fréquence résonante fondamentale (la fréquence du pic de PSD entre 4.3-5.8 mHz) dépend du temps magnétique local et est maximale autour du midi local magnétique. Cette caractéristique est due au fait que la dimension de la cavité magnétosphérique dépend du temps et est minimale à midi. Une onde harmonique est aussi observée à environ 10 mHz, qui est maximale dans le secteur jour, et est fortement atténuée lorsque on va vers le coté nuit. La comparaison entre les PSDs des pulsations provoquées pas l'augmentation brutale et la décroissance brutale de P_{sw} montre que la fréquence des pulsations est inversement proportionnelle à la dimension de la magnétopause. Puisque la résonance des lignes de champ (FLR) est excitée par des ondes cavité compressée/guide d'onde, ces résultats indiquent que la fréquence de résonance dans la cavité magnétosphérique/guide d'onde est due non seulement aux paramètres du vent solaire mais est aussi influencée par le temps magnétique local du point d'observation.

Mots clés

Accélération non adiabatique, Dynamique de la couche de plasma, Sous-orage et dipolarisation, Décroissance de la pression dynamique du vent solaire, Pulsations géomagnétiques.

Abstract

This doctoral dissertation includes two main topics: one is about the nonadiabatic acceleration of ions in the near-Earth plasma sheet, the other is about the geomagnetic pulsations driven by the decrease of solar wind dynamic pressure.

The nonadiabatic acceleration of plasma sheet ions is important to understand the formation of ring current and substorm energetic injections. In the first part, we present case studies of nonadiabatic acceleration of plasma sheet ions observed by Cluster and Double Star TC-1 in the near-Earth magnetotail (e.g. at (X, Y, Z)=(-7.7, 4.6, 3.0) R_E in the 30 October 2006 event), much closer to the Earth than previously reported. We find that the ion energy flux variations, which are characterized by a decrease over 10 eV-20 keV and an increase over 28-70 keV, are caused by the ion nonadiabatic acceleration closely associated with strong electromagnetic field fluctuations around the H^+ gyrofrequency. We also find that the ions after nonadiabatic acceleration have 'bunched gyrophases', which is the first report in the plasma sheet since the 'gyrophase bunching effect' was observed in the solar wind in 1980s. We interpret the ion energy flux variations and the bunched gyrophases by using a nonadiabatic model. The analytic results and simulated spectrums are in good agreement with the observations. This analysis suggests that nonadiabatic acceleration associated with magnetic field fluctuations is an effective mechanism for ion energization in the near-Earth plasma sheet. The presented energy flux structures can be used as a proxy to identify this dynamic process.

In the second part, we investigate the response of geomagnetic field to an impulse of solar wind dynamic pressure (P_{sw}), which hits the magnetosphere on 24 August 2005. Using the high resolution geomagnetic field data from 15 ground stations and the data from Geotail, TC-1 and TC-2, we studied the geomagnetic pulsations at auroral latitudes driven by the sharp decrease of P_{sw} in the trailing edge of the impulse. The results show that the sharp decrease of P_{sw} can excite a global pulsation in the frequency range 4.3-11.6 mHz. The reversal of polarizations between

two auroral latitude stations, larger Power Spectral Density (PSD) close to resonant latitude and increasing frequency with decreasing latitude indicate that the pulsations are associated with Field Line Resonance (FLR). The fundamental resonant frequency (the peak frequency of PSD between 4.3-5.8 mHz) is magnetic local time dependent and largest around magnetic local noon. This feature is due to the fact that the size of magnetospheric cavity is local time dependent and smallest at noon. A second harmonic wave at about 10 mHz is also observed, which is strongest in the daytime sector, and is heavily attenuated while moving to night side. The comparison between the PSDs of the pulsations driven by sharp increase and sharp decrease of P_{sw} shows that the frequency of pulsations is inversely proportional to the size of the magnetopause. Since the FLR is excited by compressional cavity/waveguide waves, these results indicate that the resonant frequency in the magnetospheric cavity/waveguide is decided not only by solar wind parameters but also by magnetic local time of observation point.

Keywords

Nonadiabatic Acceleration, Plasma Sheet Dynamics, Substorm and Dipolarization, Decrease of Solar Wind Dynamic Pressure, Geomagnetic Pulsations

Introduction (en français)

Le lancement du premier satellite artificiel Spoutnik par l'URSS le 4 octobre 1957 marque l'accès à l'espace pour l'humanité. Dans le demi-siècle qui a suivi beaucoup de missions d'exploration ont été réalisées dans le monde. Beaucoup de ces missions ont été conçues pour étudier la magnétosphère de la Terre. Fondées sur ces données ainsi recueillies, on a pu construire par étapes la structure de base et les processus dynamiques significatifs de la magnétosphère.

La magnétosphère de la Terre est une entité dynamique, dont les dimensions et la forme sont déterminées par le vent solaire qui souffle sur elle et par le Champ Magnétique Interplanétaire (IMF). La direction de l'IMF, spécialement, affecte le taux de reconnexion à la magnétopause et la frontière de la queue, et ainsi contrôle la forme de la magnétosphère et indirectement le processus de transfert particules/énergie du vent solaire à la magnétosphère interne.

Un des processus de transfert d'énergie dans l'espace le plus notable et fondamental est le sous-orage magnétosphérique. Le sous-orage magnétosphérique implique un processus qui dissipe l'énergie d'origine vent solaire de la magnétosphère à l'atmosphère supérieure de la Terre. Pendant un épisode de sous-orage, un effet collectif sur le champ magnétique de la Terre, sur les courants magnétosphériques et ionosphériques, et les évènements auroraux peuvent être observés, ce qui permet d'étudier les sous-orages par différentes techniques d'observation. Pour arriver à une bonne compréhension de la dynamique des sous-orages, il faut comparer les signatures aurorales avec la dynamique de la couche de plasma. Les observations montrent clairement que le processus entier d'un sous-orage implique une phase de croissance, début et éclatement, une phase d'expansion et une phase de retour. Après 50 ans d'études intensives, différents aspects de la morphologie des sous-orages ont été qualitativement établis. Cependant il n'y a pas encore de consensus sur les

conditions physiques exactes et le mécanisme qui cause le déclenchement d'un sous-orage. qui contrôle le lieu où se produit le sous-orage, et qui détermine l'intensité des sous-orages.

Les plasmas dans l'espace sont toujours sensibles aux perturbations du champ électromagnétique. Des ondes peuvent être excitées par une grande variété d'instabilités de plasma. Par exemple, une perturbation à la magnétopause par un changement soudain de la pression du vent solaire déplacera la frontière de sa position d'équilibre et une perturbation basse fréquence sera créée et se propagera vers la Terre sous forme d'ondes d'Alfvén. Des ondes dans une grande gamme de fréquences sont détectées dans l'espace et au sol, de moins de 1 mHz à plus de 10 Hz. La nature des ondes dans le plasma dépend beaucoup des paramètres du plasma, et les modes d'ondes peuvent être identifiés à partir d'informations fournies par le plasma ambiant et les données de champ magnétique. D'autre part les ondes peuvent aussi interagir avec les particules chargées et elles seront amplifiées ou atténuées par l'interaction. L'interaction onde-particule est un moyen important de transformation de l'énergie dans l'espace. Par exemple elle peut entraîner la précipitation des particules de la magnétosphère dans l'atmosphère. La couche de plasma de la queue magnétique est aussi une région probable pour les interactions ondes-particules, parce que beaucoup d'instabilités de plasma surviennent pendant la montée du sous-orage et sa phase d'expansion, par exemple l'instabilité de courant dans la queue magnétique, l'instabilité de dérive hybride basse, l'instabilité de dérive "kink-sausage", l'instabilité d'Alfvén portée par un courant. En plus, des ondes pendant la montée du sous-orage sont aussi associées avec la reconnexion magnétique dans la couche de plasma à mi-queue, ce qui non seulement change la topologie du champ magnétique mais aussi transfère de l'énergie du champ magnétique au plasma thermique et à l'écoulement.

La mission Cluster (4 satellites, 2 lancés en juillet 2000 et 2 autres en août 2000) est un des plus remarquables projets d'exploration spatiale. La formation

en tétraèdre consiste en quatre satellites identiques et la détection très complète des paramètres physiques sur chaque satellite fournit une bonne opportunité pour étudier les régions clés de l'espace autour de la Terre, telles que l'onde de choc, la magnétopause, la queue magnétique et la magnétosphère interne. Le satellite chinois TC-1 du projet Double Star, en coopération scientifique entre l'Académie des Sciences de Chine et l'ESA a été lancé le 29 décembre 2003. Plusieurs instruments européens, identiques à ceux développés pour les satellites Cluster, ont été installés à bord de TC-1 Double Star. Dans cette thèse, nous présentons d'abord une recherche sur la dynamique de la couche de plasma de la queue magnétique pendant une dipolarisation magnétosphérique en utilisant les données de Cluster et de TC-1 Double Star. Nous présentons ensuite une recherche sur la réponse géomagnétique à la décroissance soudaine de la pression dynamique du vent solaire en utilisant les données de stations sol.

Introduction (in English)

The launch of the first unmanned satellite Sputnik by the USSR on October 4, 1957, marks the accessibility of space for human beings. In the following half century, plenty of exploratory missions were performed in the worldwide. Many of them were designed to study the Earth's magnetosphere. Based on these collected data, the basic structure and significant dynamic processes of the magnetosphere were gradually constructed.

The Earth's magnetosphere is a dynamic entity, whose size and shape are determined by the solar wind blowing against it and the Interplanetary Magnetic Field (IMF). The direction of the IMF, especially, affects the reconnection rate of the magnetopause and the boundary of the tail, thus controls the shape of the magnetosphere and indirectly, the particle/energy transfer process from the solar wind to the inner magnetosphere.

One of the most notable and fundamental energy transfer process in space is the magnetospheric substorm. The magnetospheric substorm involves a process that dissipates electromagnetic energy of solar wind origin from the magnetosphere to the Earth's upper atmosphere. During an episode of substorm, a collective effect on the Earth's magnetic field, magnetospheric and ionospheric currents, and auroral displays can be observed, which allows substorms to be studied by various observational techniques. To reach a comprehensive understanding of substorm dynamics, a comparison of auroral signatures with the plasma sheet dynamics is required. The observations clearly demonstrate that the entire substorm process involves a growth phase, onset and breakup, expansion phase and recovery phase. After 50 years of intensive studies, various aspects of substorm morphology have been qualitatively established. However, there is still no consensus on the exact physical conditions and mechanism that cause the initiation of a substorm, what controls the location for substorms to occur, and what determines the strength of the substorms.

Plasma in space is always sensitive to the perturbations of the electromagnetic field. Waves can be excited by a variety of plasma instabilities. For example, a perturbation at the magnetopause by sudden change in the solar wind pressure will move the boundary from its equilibrium position, and a low frequency disturbance will be created and propagate to the Earth in the form of Alfvén waves. A broad range of wave frequencies is detected both in space and on ground, from less than 1 mHz to more than 10 Hz. The nature of waves in plasma strongly depends on the plasma parameters, and wave modes can be identified from information provided by the ambient plasma and magnetic field data. On the other hand, waves can also interact with charged particles, and they will be amplified or damped by the interaction. Wave-particle interaction is an important energy transformation pattern in space. For example, it can make particles to precipitate from the magnetosphere to the atmosphere. Magnetotail plasma sheet is also a probable region for wave-particle interactions, because plenty of plasma instabilities are excited there during substorm onset and expansion phase, e.g. cross-field current instability, lower-hybrid-drift instability, drift kink/sausage instability and current-driven alfvénic instability. Besides, waves during substorm onset are also associated with magnetic reconnection at mid-tail plasma sheet, which not only change the magnetic field topology but also convert energy from magnetic field energy to plasma thermal and flow energies.

Cluster mission, (4 spacecraft, 2 launched in July 2000 and 2 others in August 2000), is one of the most remarkable space exploratory projects. The tetrahedral formation consist of four identical spacecraft and the very complete detection of physical parameters on each spacecraft supplies a good opportunity to study the key geospace regions, such as bow shock, magnetopause, magnetotail and inner magnetosphere. Chinese Double Star TC-1, as a scientific cooperation between Academy of Sciences of China and ESA, was launched on 29 December 2003. Several European instruments, identical to those developed for the Cluster spacecraft, were installed on board Double Star TC-1. In this thesis, we first present a research about the dynamics of the magnetotail plasma sheet during magnetospheric

dipolarization by using the Cluster and Double Star TC-1 data. Then in the second part we present a research on the geomagnetic response to the sudden decrease of solar wind dynamic pressure by using the data of Double Star TC-1/TC-2, Geotail and ground stations.

Chapter 1 The magnetosphere and the space instruments used in this thesis

1.1 The Earth's magnetosphere

The magnetosphere of the Earth is a region in space whose shape is determined by the Earth's internal magnetic field, the solar wind plasma and the Interplanetary Magnetic Field (IMF). The boundary of the magnetosphere (magnetopause) is roughly bullet shaped, at about 10 R_E (R_E=radius of the Earth) from the Earth on the day side and on the night side (magnetotail) approaching a cylinder with a radius 20-25 R_E. The tail region stretches well past 200 R_E, and where it ends is not well known yet.

The magnetosphere is a large plasma cavity. The steaming solar wind compresses the dayside portion of the Earth's field and generates a tail which is many hundreds of R_E. The basic mechanism for the formation of the magnetosphere is fairly simple: The Earth's magnetic dipole field is exposed to a stream of charged particles. The entire magnetosphere is subject to two boundary conditions: (a) The boundary between the magnetosphere and the streaming solar wind and (b) the boundary of the magnetosphere and the neutral atmosphere. The basic structural elements of the magnetosphere are: the bow shock and the magnetosheath, the magnetopause, the magnetotail, and the inner magnetosphere [*Otto*, 2005].

The inner magnetosphere includes the plasmasphere, the radiation belts and the ring current. The plasmasphere consists of cold (~1 eV) and relatively dense (10^3 cm^{-3}) plasma of ionospheric origin, which co-rotates with the Earth. Its boundary is called the plasmapause and it is close to the boundary between closed drift paths of the particles under the influence of the co-rotation electric field and open drift paths determined by the convection electric field. Consequently, the plasmapause is located at L-shells 3-5, depending on the magnetic activity.

There are two major radiation belts. In the inner belts, mostly at L<2, the radiation is dominated by energetic protons (0.1-40 MeV) whereas the outer belt consists of electrons in the keV-MeV range. The westward drift of energetic ions around the Earth carries the westward ring current. The most important current carriers are protons in the energy range 10-200 keV [*Koskinen*, 2005]. An overall schematic of the Earth's magnetosphere is given in Fig.1.1.

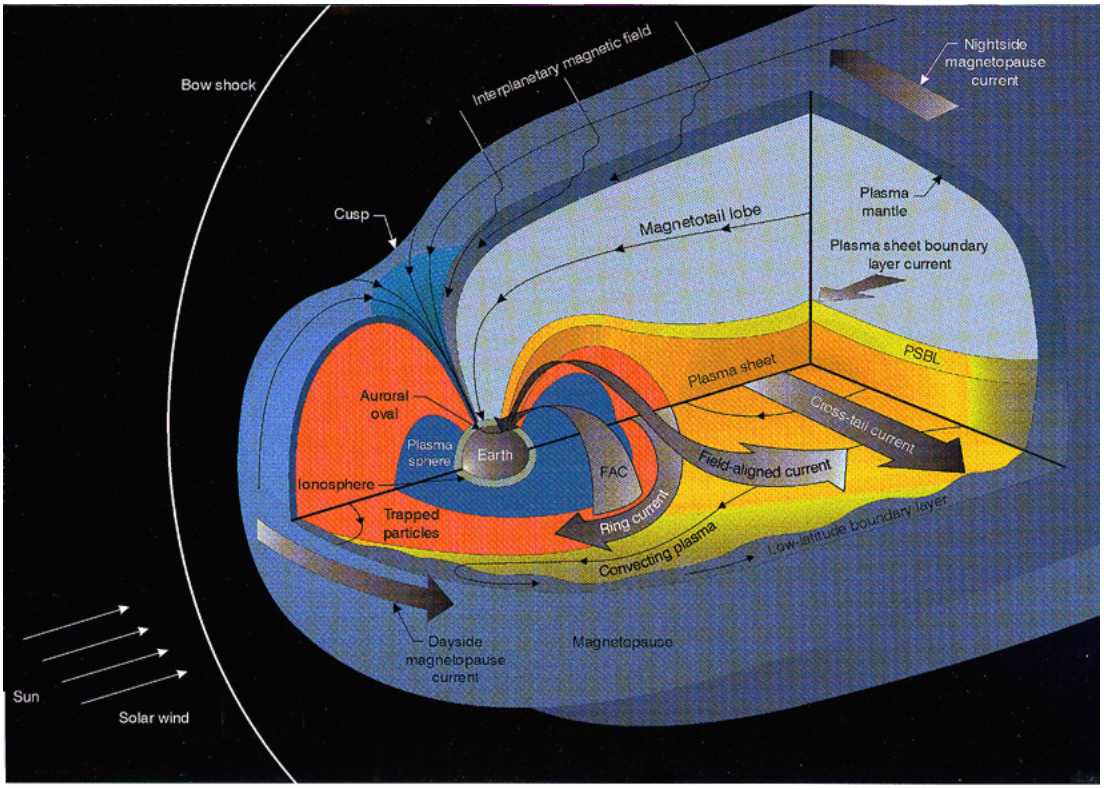

Fig.1.1 A schematic view of the Earth's magnetosphere

1.2 Plasma in the near-Earth magnetotail

Since this research is on the dynamic of the magnetotail plasma sheet, in this section we give a brief description of the three major plasma populations in the near part of the Earth's magnetic tail: tail lobes, Plasma Sheet Boundary Layer (PSBL), plasma sheet.

1.2.1 Tail Lobes

In the tail lobes, plasma densities are low, generally less than 0.1 cm^{-3} and sometimes below the level of detectability of the detectors. Ion and electron spectra are very soft, with very few particles in the 5-50 keV range. Cold ions are often observed flowing away from the earth, and their composition often suggests an ionospheric origin. There is strong evidence that the tail lobe normally lies on open magnetic-field lines [*Kivelson and Russell*, 1995].

1.2.2 Plasma Sheet Boundary Layer

The plasma sheet boundary layer is generally observed as a transition region between the almost empty tail lobes and the hot plasma sheet. Ions in this region typically exhibit flow velocities of hundreds of kilometers per second, principally parallel to or antiparallel to the local magnetic field. Frequently, counterstreaming ion beams are observed, with one beam traveling earthward, and the other traveling tailward along the field line. Densities typically are of the order of 0.1 cm^{-3}, and thermal energies tend to be smaller than the flow energies. The plasma sheet boundary layer probably lies on closed field lines [*Kivelson and Russell*, 1995].

1.2.3 Plasma Sheet

This region, often referred to as the ‘central plasma sheet’ to emphasize its distinctness from the plasma sheet boundary layer, consists of hot (kilovolt) particles that have nearly symmetric velocity distributions. Number densities typically are 0.1-1 cm^{-3}, a little bit higher than those of the plasma sheet boundary layer. Flow velocities typically are very small compared with the ion thermal velocity. The ion temperature in the plasma sheet is almost invariably about seven times the electron temperature. For the most part, the plasma sheet lies on closed field lines, although it

may sometimes contain ‘plasmoids’, which are closed loops of magnetic flux that do not connect to the Earth or solar wind.

The plasmas of the tail are dynamic. Reconnection in the distant tail converts antisunward streaming mantle plasma into beams that stream along the field lines, toward the earth; these beams mirror in the region of strong magnetic field near the earth, creating antisunward streams. The conterstreams tend to be unstable to various plasma waves, which eventually convert the streaming energy to thermal energy, creating the hot, slow flowing plasma sheet.

The composition of the plasma sheet and the outer part of the radiation belts, includes two components: H^+, which is abundant in both the solar wind and the Earth’s upper ionosphere; O^+, which is abundant in the ionosphere, but not in the solar wind. The ionospheric ion O^+, while present in modest concentrations during quiet times, is almost as abundant as H^+ during active times. These results clearly indicate that the plasma sheet ion population is a mixture of solar wind and ionospheric particles, being mostly of solar wind origin in quiet times and mostly ionospheric in active times [*Kivelson and Russell*, 1995].

1.3 The Cluster mission

Our first study is primarily based on the data obtained from instruments aboard Cluster mission and Double Star TC-1 spacecraft. These data were provided by IRAP/CNRS, CAA (Cluster Active Archive) and UK Data Centre. The data of CIS/Cluster and HIA/Double Star TC-1 were presented in the figures by using the cl software created and supplied by Emmanuel PENOU at IRAP/CNRS (http://clweb.cesr.fr/).

The Cluster mission is an ESA’s space exploration project. It was first proposed in 1982 and finally launched in the July and August of 2000. By the end of August 2000, the four Cluster satellites reached their final tetrahedral constellation [*Escoubet et al*., 2001]. The main goal of the Cluster mission is to study the small scale plasma

structures in three dimensions in key plasma regions, such as the solar wind, bow shock, magnetopause, polar cusps, magnetotail and the auroral zones, in separating, for the first time, time and space variations.

The Cluster mission is comprised of 4 identically designed spacecraft flying generally in a tetrahedral formation on similar elliptical polar orbits. The apogee is 19.6 R_E and the perigee is about 4 R_E. The constellation has an orbital period of 57 h. The plane of the orbit is fixed with respect to inertial space. The Earth, together with its magnetosphere therefore sweeps through this plane, allowing for a complete 360° scan of the magnetosphere every year.

Each Cluster satellite carries the same set of eleven instruments that allow for the measurement of electric and magnetic fields from DC to high frequencies, and the detection of electron and ion distribution functions at spin resolution.

The FluxGate Magnetometer (FGM) [*Balogh et al.*, 2001] and the Electron Drift Instrument (EDI) [*Paschmann et al.*, 1997] are dedicated to measures the magnetic and electric fields. The Wave Experiment Consortium (WEC) [*Pedersen et al.*, 1997] employs five experiments which investigate plasma waves: the Spatio-Temporal Analysis of Field Fluctuation experiment (STAFF) [*Cornilleau-Wehrlin et al.*, 1997], the Electric Field and Wave experiment (EFW) [*Gustafsson et al.*, 2001], the Waves of High frequency and Sounder for Probing of Electron density by Relaxation (WHISPER) [*Décréau et al.*, 1997] experiment, the Wide Band Data (WBD) [*Gurnett et al.*, 1997] receiver and the Digital Wave Processing (DWP) [*Woolliscroft et al.*, 1997]. The measurement for particles is executed by the Cluster Ion Spectroscopy (CIS) [*Rème et al.*, 1997, 2001] experiment, the Plasma Electron and Current Experiment (PEACE) [*Johnstone et al.*, 1997] and the Particle Imaging Detectors (RAPID) [*Wilken et al.*, 1997] instrument. The Active Spacecraft Potential Control (ASPOC) [*Riedler et al.*, 1997] experiment is responsible for the control and stabilization of the spacecraft electrostatic potential.

1.3.1 The CIS instrument

The Cluster Ion Spectrometry (CIS) experiment measures the full three-dimensional ion distribution of the major magnetospheric ions (H^+, He^+, He^{++}, and O^+) from the thermal energies to about 40 keV/e. The experiment consists of two different instruments: a COmposition and DIstribution Function analyzer (CODIF), giving the mass per charge composition with a time resolution of one spacecraft spin (4 seconds), and a Hot Ion Analyzer (HIA), which does not offer mass resolution but has a better angular resolution (5.6°) that is adequate for ion beam and solar wind measurements [*Rème et al.*, 2001].

The prime scientific objective of the CIS experiment is the study of the dynamics of magnetized plasma structures in and in the vicinity of the Earth's magnetosphere, with the determination, as accurately as possible, of the local orientation and the state of motion of the plasma structures required for macrophysics and microphysics studies.

To achieve the scientific objectives, the CIS instrumentation has been designed to satisfy the following criteria, simultaneously on the 4 spacecraft:

1. Provide a uniform coverage of ions over the entire 4π steradian solid angle with good angular resolution.

2. Separate the major ion species from the solar wind and ionosphere.

3. Have high sensitivity and large dynamic range to support high-time-resolution measurements over the wide range of plasma conditions.

4. Have the ability to routinely generate on-board the fundamental plasma parameters for major ion species and with one spacecraft spin time resolution (4 seconds).

5. Cover a wide range of energies, from spacecraft potential to about 40 keV/e.

6. Have versatile and easily programmable operating modes and data-processing routines to optimize the data collection for specific scientific studies and widely varying plasma regimes.

The Hot Ion Analyzer (HIA) instrument combines the selection of incoming ions according to the ion energy per charge by electrostatic deflection in a symmetrical, quadrispherical analyzer which has a uniform angle-energy response with a fast imaging particle detection system. This particle imaging is based on MicroChannel Plate (MCP) electron multipliers and position encoding discrete anodes. Fig.1.2 provides a cross-sectional view of the HIA electrostatic analyzer.

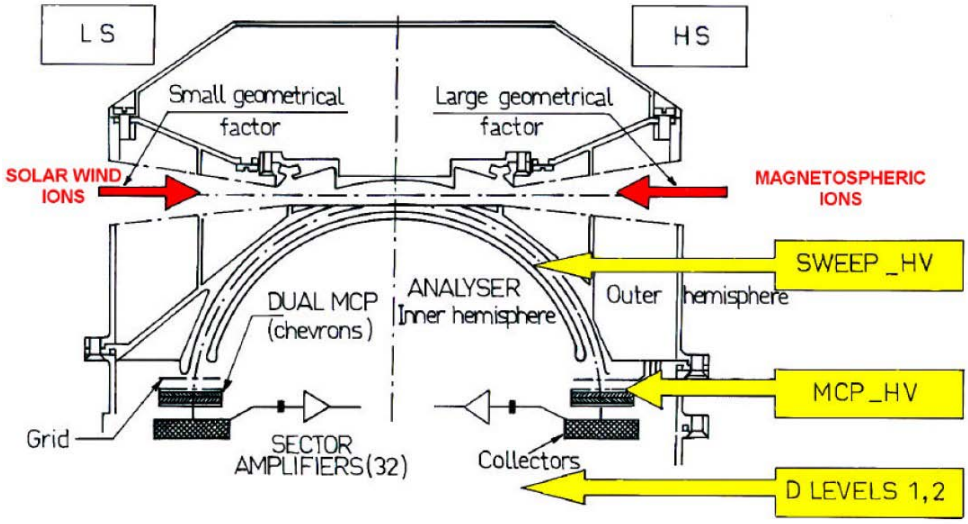

Fig.1.2 Cross sectional view of the HIA analyzer (taken from Fig.2 of [*Rème et al.*, 2001]).

The CODIF instrument is a high-sensitivity, mass-resolving spectrometer with an instantaneous 360° × 8° field of view to measure complete 3D distribution functions of the major ion species within one spin period of the spacecraft. Typically, these include H^+, He^{++}, He^+ and O^+. The sensor primarily covers the energy range between 0.02 and 38 keV/charge. With an additional Retarding Potential Analyzer (RPA) device in the aperture system of the sensor with pre-acceleration for energies below 25 eV/e, the range is extended to energies as low as the spacecraft potential. Hence, CODIF covers the core of all plasma distributions of importance to the Cluster mission.

The CODIF instrument combines the ion energy per charge selection by deflection in a rotationally symmetric toroidal electrostatic analyzer with a subsequent time-of-flight analysis after post-acceleration to larger than 15 keV/e. A cross section of the sensor showing the basic principles of operation is presented in Fig.1.3. The energy-per-charge analyzer is of a rotationally symmetric toroidal type, which is basically similar to the quadrispheric top-hat analyzer used for HIA.

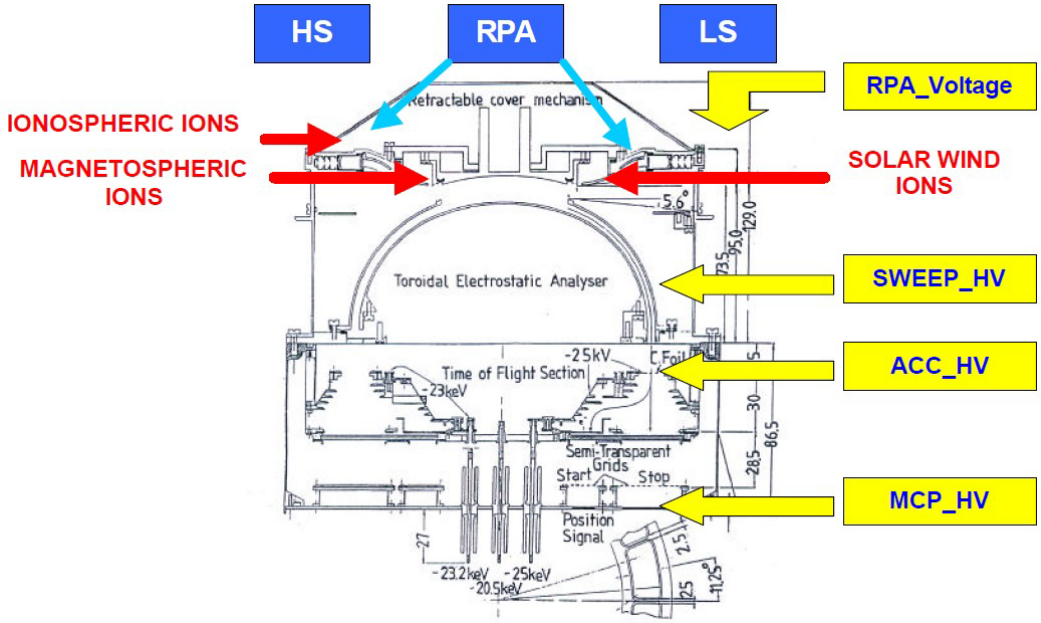

Fig.1.3 Cross sectional view of the CODIF sensor (taken from Fig.9 of [*Rème et al.*, 2001]).

1.3.2 The FGM instrument

The primary objective of the Cluster Magnetic Field Investigation (FGM) is to provide accurate measurements of the magnetic field vector at the location of the four Cluster spacecraft. The FGM instrument on each spacecraft consists of two triaxial fluxgate magnetometers and an onboard data processing unit. The magnetometers are similar to many previous instruments flown in Earth-orbit and on other planetary and interplanetary missions. The sampling of vectors from the magnetometer sensor

designated as the primary sensor is carried out at the rate of 201.75 vectors/second [*Balogh et al.*, 2001]. For this study, we use both spin and full resolution magnetic field data, provided by CAA (Cluster Active Archive).

1.3.3 The EFW instrument

The detector of the EFW instrument consists of four spherical sensors deployed orthogonally on 44 meter long wire booms in the spin plane of the spacecraft. The potential difference between two opposing sensors, separated by 88 m tip-tip, is measured to provide an electric field measurement. Since there are four sensors, the full electric field in the spin plane is measured. The potential difference between each sensor and the spacecraft is measured separately (and is often used as a high time-resolution proxy for the ambient plasma density [*Pedersen et al.*, 2008]). The potentials of the spherical sensor and nearby conductors (the so-called pucks and guards) are actively controlled in order to minimize errors associated with photoelectron fluxes to and from the spheres [*Gustafsson et al.*, 2001].

1.3.4 The RAPID instrument

The RAPID spectrometer (Research with Adaptive Particle Imaging Detectors), is an advanced particle detector for the analysis of suprathermal plasma distributions in the energy range from 20-400 keV for electrons, 30 keV-1500 keV for hydrogen ions and 10 keV/nucleon-1500 keV for heavier ions. Innovative detector concepts, in combination with pinhole acceptance, allow the measurement of angular distributions over a range of 180° in the polar angle for electrons and ions. The RAPID instrument uses two different and independent detector systems for the detection of nuclei and electrons. The Imaging Ion Mass Spectrometer (IIMS) identifies the nuclear mass of incident ions or neutral atoms from the kinetic energy equation: a time-of-flight and energy measurement determines the particle mass. One-dimensional images of spatial

intensity distributions result from the projection principle. The Imaging Electron Spectrometer (IES) is dedicated to electron spectroscopy [*Wilken et al.*, 2001].

1.4 The Double Star Program

Double Star Program (DSP) was first proposed by China in March, 1997. It is the first joint space mission between the China National Space Administration and the European Space Agency. The DSP consists of two satellites: the equatorial satellite of DSP (TC-1) and the polar satellite of DSP (TC-2). The first spacecraft, TC-1 was launched on December 29, 2003, and the second one, TC-2, was launched on July 25, 2004. TC-1 is at an eccentric equatorial orbit of 570×79000 km altitude with a 28° inclination. TC-2 is at a polar orbit of 560×38000 km altitude. The orbits have been designed to complement the Cluster mission by maximizing the time when both Cluster and Double Star are in the same scientific regions [*Liu et al.*, 2005]. The main goal of the Double Star mission is to study the effect of the Sun on the near-Earth environment, the trigger mechanism and physical models of geomagnetic storms and sub-storms. To fulfill the scientific objectives, TC-1 explores the radiation belts, the plasmasphere, the ring current, the plasma sheet, the magnetopause, the magnetosheath, and the bow shock, while TC-2 explores the radiation belts, the plasmasphere, the ring current, the polar regions (auroral oval and polar cap), the cusp and the lobe [*Shen et al.*, 2005].

Each Double Star spacecraft carries eight scientific instruments. The instruments are measuring dc and ac magnetic fields, distribution functions of electron and ions of low and high energies, and energetic neutral atoms. In addition a spacecraft potential control is included on TC-1 to keep the spacecraft close to the plasma potential. The instruments aboard the spacecraft are almost identical to those developed for the Cluster spacecraft [*Liu et al.*, 2005].

The HIA (Hot Ion Analyzer) instrument on board the TC-1 spacecraft is an ion spectrometer nearly identical to the HIA sensor of the CIS instrument on board the 4

Cluster spacecraft. However, HIA on Double Star was adapted to the TC-1 spacecraft and orbit, and has some differences with respect to the Cluster HIA:

1. The interface board has been changed.

2. In order to include radiation shielding, taking into account the orbit of TC-1, the size of the box has been increased by 4mm on each side, on the top and on the rear, and the total mass of the sensor is 3.5 kg.

3. There is a new interface for telemetry.

4. The telemetry products have some changes.

5. There is a new interface for commanding.

6. The telemetry data rate is 4.44 kbits/s (The rate for Cluster is 5.5 kbits/s in normal mode for HIA and CODIF together).

The HIA instrument onboard the Cluster mission has two sections with two different sensitivities (different geometrical factors), corresponding respectively to the 'high G' and 'low G' sections, where the 'low G' section is designed mainly for solar wind studies. For Double Star TC-1 the instrument operation is on the ‘high G’ section, since the spacecraft was planned to rarely cross the average (model-predicted) position of the bow shock. However, thanks to the higher apogee than scheduled of the TC-1 spacecraft, and to the bow shock in/out motion around its average position, the spacecraft frequently gets into the solar wind but stays near the bow shock [*Rème et al.*, 2005].

1.5 The cl software

The cl software, as an easy way to plot multi-experiment and multi-mission data, enables 3D visualization of position/orientation of spacecraft, and computation of various physical characteristics (spectra, distribution functions, etc.). It has been originally created by Mr. Emmanuel PENOU at IRAP/CNRS for the Cluster project

in the year 2000. New projects like MEX, VEX and STEREO have been regularly and naturally added. Recently, old projects like WIND and INTERBALL have also been integrated.

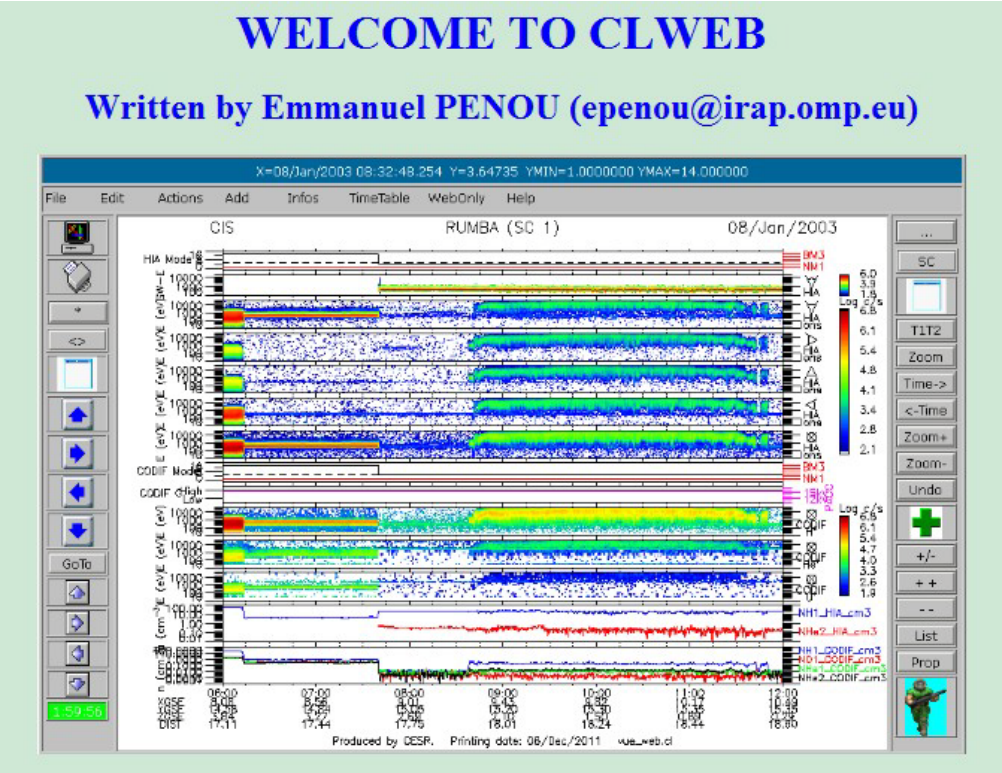

Fig.1.4 The web interface of the Clweb software.

Cl can plot a composition of panels of the following types:

1. Title

2. Text

3. External plots or images

4. Orbit data

5. Can dynamically read calibration and compute calibrated data (like count/sec, flux, distribution function) and plot these quantities in 3d spectrograms or contours

(time/energy, time/theta, time/phi, time/mass, time/pitch-angle, phi/theta, distribution function, mass/energy, RLONG/RLAT) or in 2d plot (energy, time).

6. Can also compute on-board and ground moments (Density, Velocity, Heat Flux, Pressure) and some user defined products (partial moments)

7. Can compute current for Cluster

8. Time series (header): can plot one or more curves (field of the data file or a mathematic expression with these fields)

The Clweb (http://clweb.cesr.fr/) is a web version of cl. It has been tested under “Internet explorer”, “Firefox”, “Chrome”, “Safari” and “Opera” (no right click under Opera). The web version makes it more convenient to operate for the users. Fig.1.4 shows the web interface of the Clweb software.

Chapter 2 Nonadiabatic acceleration of ions

2.1 Adiabatic invariants for charged particles in the electromagnetic field

An ion or an electron moving through the Earth's magnetosphere executes three motions: (1) cyclotron motion about the magnetic-field line, (2) bounce motion along the field line, and (3) drift perpendicular to magnetic field line. For charged particles in electromagnetic fields, an adiabatic invariant is associated with each of the three types of motions the particles can perform. This can be clearly seen in Fig.2.1.

2.1.1 First Adiabatic Invariant

A remarkable feature of the motion of charged particles in collisionless plasmas is that even though the energy changes, there is a quantity that will remain constant if the field changes slowly enough. By 'slowly enough' we mean that the field changes encountered by the particle within a single gyration orbit will be small compared with the initial field. If this condition is satisfied, then the particle's 'magnetic moment'

$$\mu = \frac{\frac{1}{2}mv_{\perp}^{2}}{B} \qquad (2.1)$$

will remain constant.

Note that if μ remains constant as the particle moves across the field into regions of different field magnitudes, some acceleration is required. The quantity μ is also called the first adiabatic invariant. Here, 'adiabatic' refers to the requirement that μ may not remain invariant or unchanged unless the parameters of the system, such as its field strength and direction, change slowly [*Kivelson and Russell*, 1995].

2.1.2 Second Adiabatic Invariant

The longitudinal invariant is associated with the $V_{\parallel}$ motion. If the field has a mirror symmetry where the field lines converge on both sides as in a dipole field,

there is the possibility for a second adiabatic invariant J. A particle moving in such a converging field will be reflected from the region of strong magnetic field and can oscillate in the field at a certain bounce frequency ω_b. The longitudinal invariant is defined by

$$J = \oint m v_{\parallel} ds \qquad (2.2)$$

where $V_{\parallel}$ is the parallel particle velocity, ds is an element of the guiding center path and the integral is taken over a full oscillation between the mirror points.

For electromagnetic variations with frequencies $w \ll w_b$, the longitudinal invariant is a constant, irrespective of weak changes in the path of the particle and its mirror points due to slow changes in the fields [*Baumjohann and Treumann*, 1996].

2.1.3 Third Adiabatic Invariant

The third invariant φ, is simply the conserved magnetic flux encircled by the periodic orbit of a particle trapped in an axisymmetric mirror magnetic field configuration when it performs closed drift shell orbits around the magnetic field axis. The drift invariant can be written as

$$\Phi = \oint v_d r d\psi \qquad (2.3)$$

where V_d is the sum of all perpendicular drift velocities, ψ is the azimuthal angle, and the integration must be taken over a full circular drift path of the particle. Whenever the typical frequency of the electromagnetic fields is much smaller than the drift frequency, $w \ll w_d$, φ is invariant and essentially equal to the magnetic flux enclosed by the orbit [*Baumjohann and Treumann*, 1996].

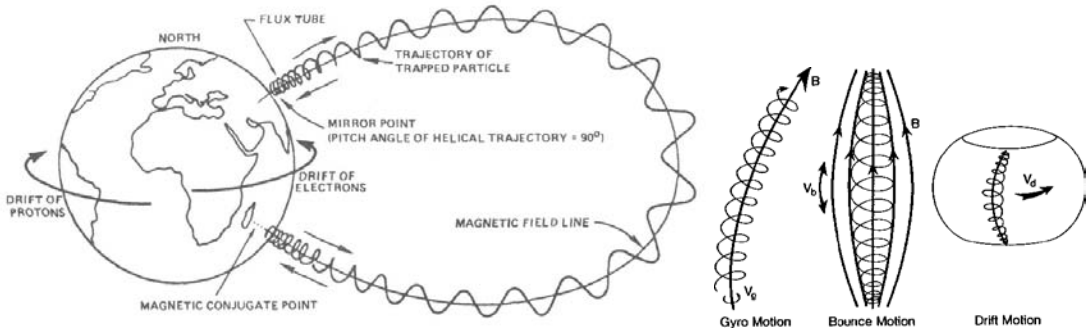

Fig.2.1 Schematic of particle motion in a magnetic field

2.2 Nonadiabatic acceleration of ions by spatial variations of the magnetic field

The energization of plasma sheet ions is a fundamental subject of the dynamics of magnetotail. Theoretical and observational studies indicate that in the plasma sheet, the ions can be non-adiabatically energized when the first adiabatic invariant is violated [e.g. *Chen*, 1992].

There are several factors that can violate the first adiabatic invariant. First, it is the spatial variation of the magnetic field that can lead to the violation of the first adiabatic invariant. In this case, the radius of curvature of field lines should be comparable to or smaller than the gyration radius of the particles. There are many studies on this subject, starting with the Speiser orbits [*Speiser et al.*, 1965]. Particles reaching the midplane were shown to execute meandering motion about the field minimum prior to be ejected from the current sheet. Since this original work, the nonadiabatic particle behavior has been regarded as of key importance for the plasma sheet formation and dynamics [*Chen*, 1992]. For these studies, the parameter κ (square root of the ratio between the minimum radius of curvature of the magnetic field lines and maximum Larmor radius for a particle of given energy) is often used to classify particle orbits in a field reversal. *Sergeev et al.* [1983] first introduced the parameter κ and they placed the onset of nonadiabatic motion in the midtail at $\kappa \approx 2.9$. If $\kappa < 3$, the magnetic moment may not be conserved, and a wide varieties of orbits (with associated energy gain) appear. Furthermore, the chaotic motion was observed

when κ approaches unity [*Chen and Palmadesso*, 1986; *Büchner and Zelenyi*, 1989; *Chen et al.*, 1990; *Birn and Hesse*, 1994].

2.3 Nonadiabatic acceleration of ions by temporal variations of the magnetic field

Second, it is the temporal variation of the magnetic field that leads to the violation of the first adiabatic invariant. In this case, the magnetic field variation period should be comparable to or shorter than the cyclotron period of charged particles. It occurs frequently during magnetospheric dipolarization, and always leads to significant energy gains. *Delcourt et al.* [1990] examined the nonadiabatic behavior of ions during magnetic field dipolarization by means of three-dimensional particle codes, and demonstrated that the large electric fields induced by the dipolarization can lead to dramatic energization and pitch angle diffusion for the midtail populations. *Delcourt et al.* [1997] more specifically examined the behavior of O^+ ions during dipolarization. Their results of numerical trajectory calculations and analytical analyses show that due to the effect of the inductive electric field, a three-branch pattern of magnetic moment jump was obtained, which depends upon the initial energy of the particles before accelerations.

2.3.1 Simulation results for parallel motion of the particles

In order to bring out key parameters in the particle orbit, the parallel and the perpendicular motions will be considered separately. Ions that are initially aligned with the magnetic field will be examined first.

For the temporal variation of the magnetic field, *Delcourt et al.* [1990] examined the nonadiabatic behavior during magnetic field dipolarization by means of three-dimensional particle codes, and demonstrated that it can lead to dramatic energization and pitch angle diffusion.

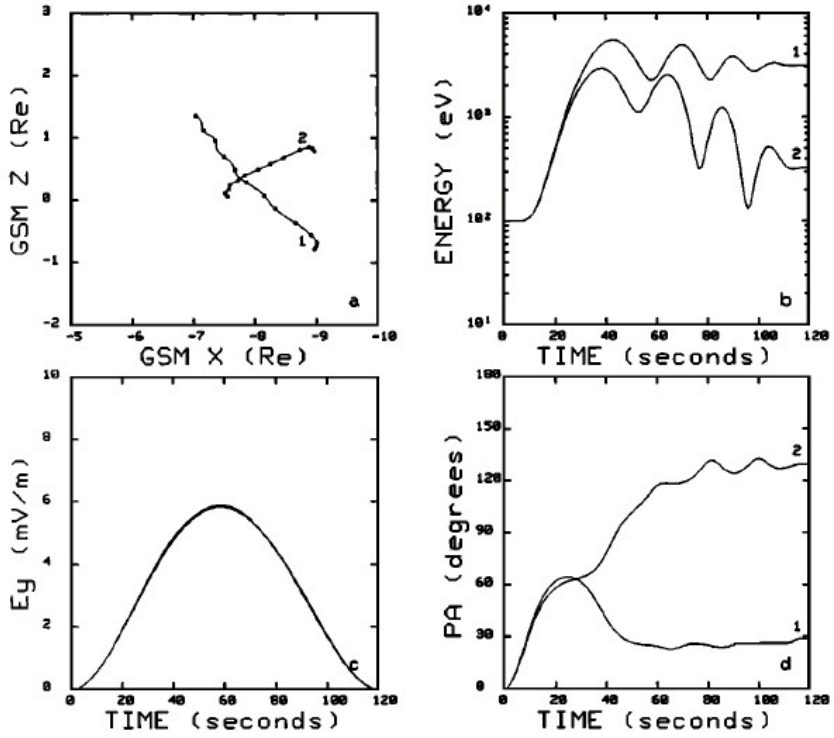

Fig.2.2 Simulation results for initially field-aligned O^+: (a) trajectory projections in the GSM XZ plane, (b) kinetic energy, (c) electric field, and (d) pitch angle versus time. The particles are injected with 100 eV energy and 0° pitch angle, at 9 R_E geodistance, 00 MLT and symmetrical positions about the equator: -5° (trajectory 1) and 5° (trajectory 2) latitude. In Fig.2.2a, dots indicate the time in 10 second steps (taken from Fig.2 of [*Delcourt et al.* 1990]).

The storm time trajectory calculations were carried out using the magnetic field model of *Mead and Fairfield* [1975]. Fig.2.2 presents the trajectory results of two O^+ ions initially aligned with the magnetic field and located at symmetrical positions about the center plane. Fig.2.2a shows the trajectory projection in the midnight meridian plane, while the respective energy and pitch angle variations are indicated in Fig.2.2b and Fig.2.2d. Also, the electric fields 'viewed' during transport are displayed in Fig.2.2c. With such zero initial pitch angle, both particles are expected to move from south to north, which is indeed the case for the southern hemisphere originating ion (trajectory 1). For this O^+, Fig.2.2b shows a net acceleration of the order of 3 keV.

Fig.2.2d reveals a substantial pitch angle scattering for this ion, up to 30° at the end of the collapse.

A drastically different behavior is noticeable for the O^+ initiated above the equator (trajectory 2) since, instead of traveling northward, it is rapidly reflected toward the opposite hemisphere (Fig.2.2a). This creation of a high-altitude mirror point is further apparent from Fig.2.2d which depicts a final pitch angle of the order of 130°. Also, it can be seen in Fig.2.2b that this latter O^+ globally experiences a weaker energization (of the order of 300 eV), though both particles experience similar electric fields during transport (Fig.2.2c), up to 6 mV/m at half-collapse (note that similar but inverted patterns are obtained using 180° initial pitch angle). These features can be qualitatively understood by examining the parallel equation of motion (details in [*Delcourt et al.* 1990]).

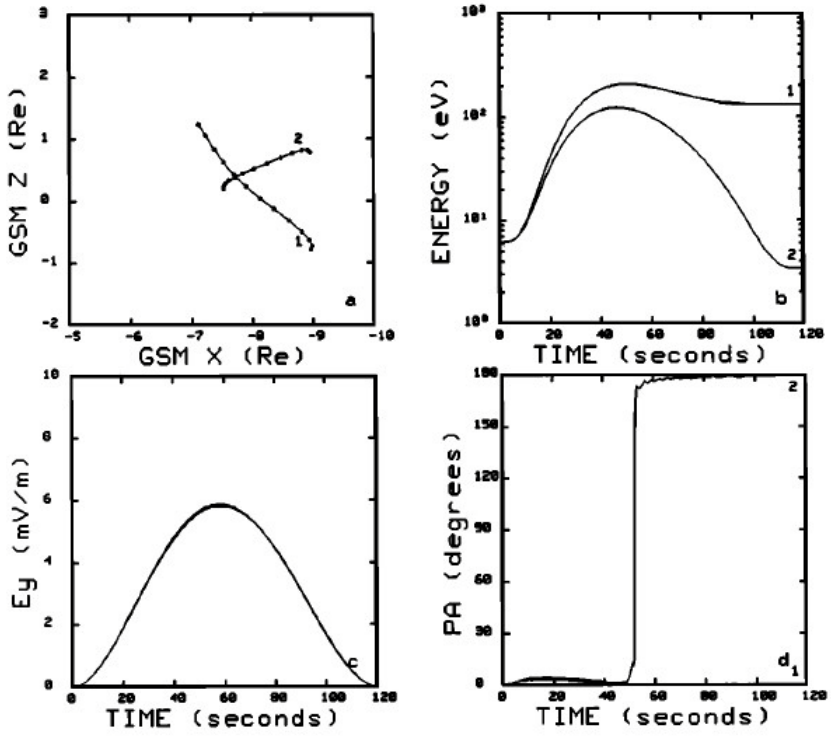

Fig.2.3 Identical to Fig.2.2, but for protons with 6 eV initial energy (taken from Fig.5 of [*Delcourt et al.* 1990]).

To further confirm these patterns, Fig.2.3 presents the results of the simulations for protons injected with velocities identical to those of O^+ (Fig.2.2), yielding an

initial energy of 6 eV. Fig.2.3a indeed displays H^+ orbits similar to those of O^+, with creation of a high-altitude mirror point for the northern hemisphere originating particle. And the final pitch angle can develop to be as high as 180° for the H^+ initiated above the equator (trajectory 2, in Fig.2.3d).

2.3.2 Simulation results for perpendicular motion of the particles

Now we discuss the particle's motion in the plane perpendicular to the magnetic field. *Delcourt et al.* [1997] investigate the dynamics of near-Earth plasma sheet ions during storm time dipolarization of the magnetospheric field lines. They more specifically examine the behavior of O^+ ions that are trapped in the equatorial vicinity. It is showed that during field lines dipolarization, these particles may be transported in a nonadiabatic manner and experience large magnetic moment enhancement together with prominent 'bunching in gyration phase' which was first observed in the solar wind at the bow shock [*Gurgiolo et al.*, 1981; *Eastman et al.*, 1981; *Fuselier et al.*, 1986]. The nonadiabatic acceleration and the gyration phase bunching effect occur below some threshold energy at the dipolarization onset, this threshold energy being controlled by the amplitude of the magnetic transition and by the injection depth in the magnetotail. In the near-Earth tail, the phase-bunched particles possibly experience intense (up to the hundred of keV range) nonadiabatic energization.

In this study, instead of the *Mead and Fairfield* [1975] model which was used in [*Delcourt et al.*, 1990], the trajectory calculations during storm time dipolarization were carried out using the magnetic field model of *Tsyganenko* [1989] (referred to be T-89), which provides an accurate average description of the various magnetospheric current contributions.

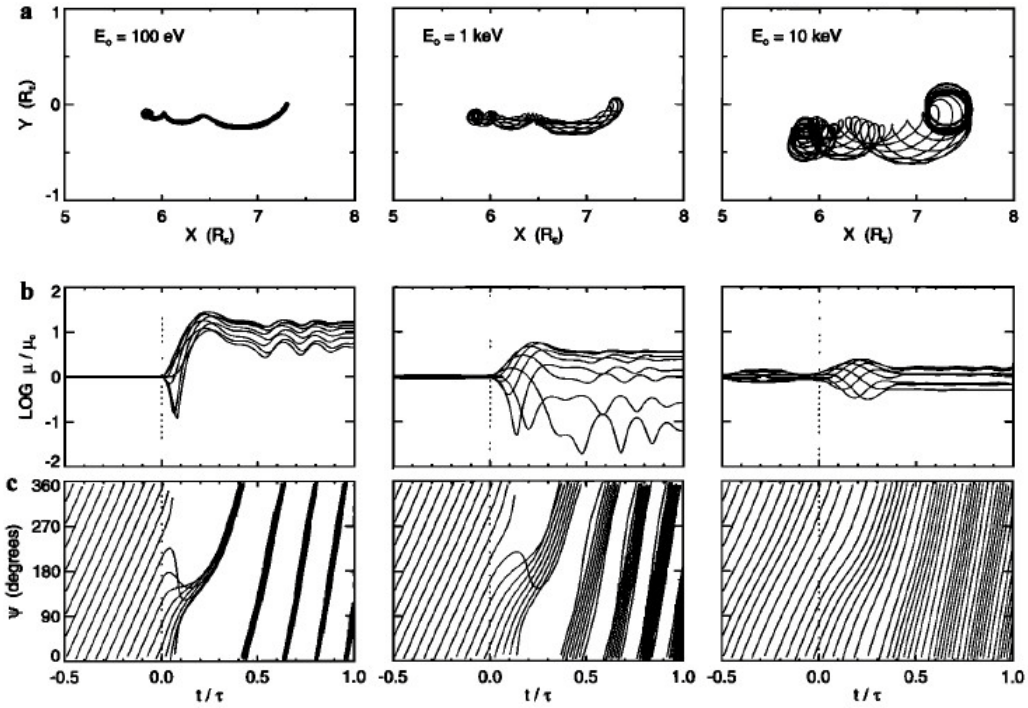

Fig.2.4 Computed trajectories of equatorially trapped O^+ ions in the time-dependent T-89 model: (a) trajectory projection in the equatorial plane, (b) magnetic moment (normalized to the initial value) versus time, (c) gyration phase versus time. The ions are launched from a guiding center position at 7.3 R_E with distinct gyration phases (from 0° to 360° by steps of 45°) and distinct energies: (from left to right) 100 eV, 1 keV, and 10 keV. In Fig.2.4c, the time is normalized to the dipolarization timescale (taken from Fig.2 of [*Delcourt et al.*, 1997]).

Fig.2.4 shows an example of equatorial trapped particle trajectories during such a reconfiguration of the magnetic field lines. They considered O^+ ions with distinct energies (from left to right: 100 eV,1 keV, and 10 keV), distinct gyration phases (from 0° to 360° by steps of 45°) and an initial guiding center position at 7.3 R_E. Fig.2.4a shows that O^+ trajectories in the X-Y plane, and it can be seen that during dipolarization, the ions are injected earthward (down to 6 R_E) under the effect of a large (up to 20 mV/m) transient electric field. Fig.2.4b shows the variation of the ion magnetic moment μ (normalized to the initial value) as a function of time (normalized to the dipolarization timescale), and it can be seen that the initially low-energy O^+ (left panel) experience μ enhancement (by about a factor 10) regardless of initial

gyration phase. In contrast, O^+ ions with initially 1 keV energy are subjected to either μ enhancement or damping depending upon initial gyrophase (middle panel), whereas the 10 keV O^+ experience negligible μ change (right panel). Fig.2.4c shows the O^+ gyration phase as a function of time, and it is apparent that the systematic μ enhancements at initially low energy (left panel) go together with prominent bunching in gyration phase. That is, although the ions initially are uniformly distributed in gyration phase, a dramatic bunching rapidly occurs after the dipolarization onset (t=0). This bunching persists throughout dipolarization and, at t=τ, the ions exhibit nearly identical phases, of the order of 90°. In Fig.2.4 (center) where one has either μ enhancement or damping, a much less pronounced bunching effect can be seen with postdipolarization phases between 0° and 180°. Finally, negligible bunching is noticeable in Fig.2.4 (right), consistently with the nearly adiabatic (magnetic moment conserving) behavior of the particles.

In order to illustrate the variability of the particle orbits with injection depth in the magnetotail, Fig.2.5 shows the results of O^+ trajectory calculations when the initial guiding center position is set at 8 R_E. In a like manner to Fig.2.4, it can be seen that the initially low-energy O^+ (left panels) experience systematic μ enhancement as well as prominent bunching in gyration phase. On the other hand, a similar behavior is now noticeable for O^+ ions with 1 keV initial energy (center panels of Fig.2.5). Both for 100 eV and 1 keV energies, the ion postdipolarization phases are now of the order of 160°. As for the 10 keV O^+ (right panels of Fig.2.5), either μ enhancement or damping is here obtained depending upon initial gyrophase and a weak bunching effect is perceptible. The nonadiabatic features shown in Fig.2.5 are thus quite similar to those of Fig.2.4 but now affect particles with larger energies. In other words, the threshold energy below which systematic μ enhancement and phase bunching are obtained is higher as the injection depth increases. Also, a closer examination of Fig.2.4 and Fig.2.5 suggests a two-step behavior of the particles during dipolarization, namely, (1) a rapid change of magnetic moment immediately after the onset of dipolarization and (2) subsequent motion at nearly constant μ (i.e., nearly adiabatic

transport). Grouping in gyration phase occurs during the first one of these sequences whereas, during the second one, the phase-bunched particles gyrate at the local Larmor frequency.

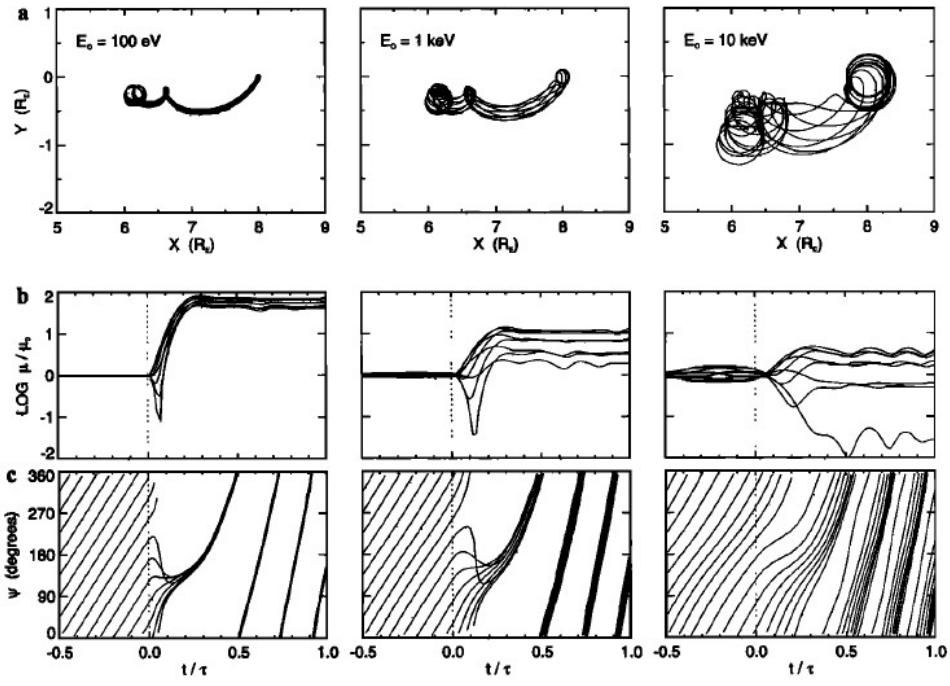

Fig.2.5 Identical to Fig.2.4 but for an initial guiding center position at 8 R_E (taken from Fig.3 of [*Delcourt et al.*, 1997]).

For proton, Fig.5 in *Delcourt et al.* [1994] showed that the protons at L=11 are accelerated below 1 keV, either accelerated or decelerated near 1 keV, no obvious change above 1 keV. The nonadiabatic acceleration region for proton is further tailward than oxygen ion, because their gyration period is much shorter than the dipolarization period in the near-Earth region.

2.3.3 Observations and statistical results

Besides simulations, here are observations: some studies [e.g. *Nosé et al.*, 2000] show that the flux and energy density of O^+ ions increase more strongly than those of H^+ ions in the plasma sheet during substorm. A possible explanation is that O^+ ions are nonadiabatically accelerated by dipolarization, while H^+ ions are not. Because that

the gyration period of O^+ ions tend to be closer to the dipolarization time scale than that of H^+ ions. Since the dipolarizations normally have timescales of several minutes, they would preferentially accelerate heavy ions (O^+ at X= -6 to -16 R_E) [e.g. *Nosé et al.*, 2000], although sometimes they can also accelerate light ions (H^+ at X= -10 to -15 R_E) [*Delcourt et al.*, 1990]. In comparison with O^+, the H^+ ions in the near-Earth have shorter gyration periods (several seconds). Consequently they are more inclined to be accelerated adiabatically (see in Fig.2.6).

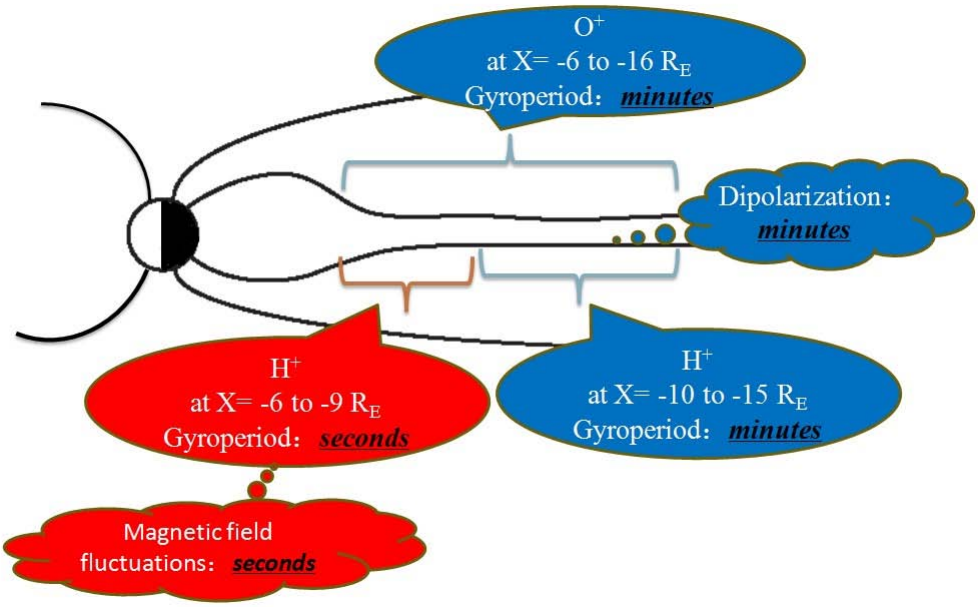

Fig.2.6 Occurring regions of nonadiabatic acceleration for H^+ and O^+ ions

All the simulations and observations above are based on the idea that nonadiabatic accelerations occur when the ion cyclotron periods are close to the dipolarization time scale. However, *Ono et al.* [2009] and *Nosé et al.* [2012] statistically demonstrate that magnetic field fluctuations (normally have timescales of several seconds), whose periods are much shorter than the dipolarization time scales, do nonadiabatically accelerate H^+ ions in the near-Earth plasma sheet (see in Fig.2.6).

First, they found that the energy spectrum of H^+ ions sometimes becomes harder than that of O^+ ions during dipolarization. Fig.2.7 shows two examples of dipolarization observed by Geotail spacecraft in 2003. Fig.2.7b and Fig.2.7d show the energy spectrum of H^+ and that of O^+ for 15 min intervals before (triangles) and after

(diamonds) the dipolarization. The 15 min intervals are indicated in the gray shadings of Fig.2.7a and Fig.2.7c. In Fig.2.7b the energy spectrum of O^+ changes more drastically than that of H^+, implying that O^+ ions are more accelerated after the onset, as reported in the previous studies. In contrast, Fig.2.7d shows the opposite result; that is, the energy spectrum of H^+ changes more drastically than that of O^+.

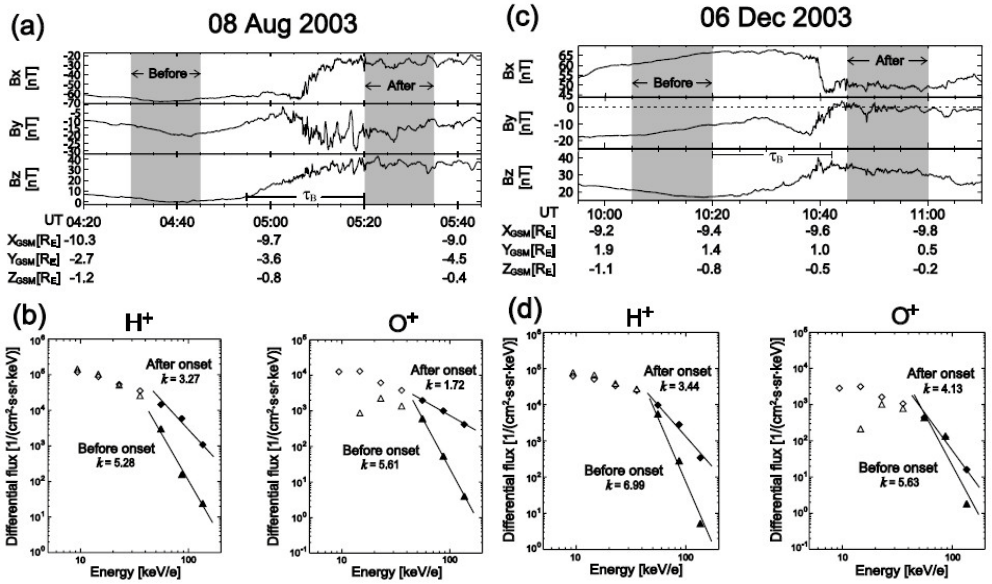

Fig.2.7 Two examples of substorm-associated dipolarization events. (a and c) Magnetic field in GSM coordinates. (b and d) Fifteen minute averages of the energy spectrum of H^+ and that of O^+ ions before (triangles) and after (diamonds) substorm onsets, where the time periods are shown by gray shadings in Fig.2.7a and Fig.2.7c (taken from Fig.3 of [*Ono, et al.*, 2009]).

In order to discuss above mentioned properties quantitatively, they fit $J = J_0 E^{-k}$, where k and J_0 are constant, to differential fluxes at three energy levels (56, 87, 136 keV/e) and estimate spectral index k before and after onsets. In Fig.2.7b and Fig.2.7d the filled triangles and the filled diamonds indicate the spectrum used for the fittings. The fitting results are shown by the lines. Then they calculate the k ratio (before/after onset). If the k ratio is greater than 1, which means that the spectrum becomes harder after an onset, ions with high energy are considered as nonadiabatically accelerated [*Christon et al.*, 1991]. If the ratio is near 1, they are regarded as adiabatically accelerated.

In the case of Fig.2.7b index k varies from 5.28 to 3.27 for H^+ ions and from 5.61 to 1.72 for O^+ ions so that the k ratios are 1.61 and 3.26, respectively; that is, both ions are considered to be accelerated nonadiabatically and the energy spectrum of O^+ becomes harder after the onset than that of H^+. In contrast, in the case of Fig.2.7d the k ratios are 2.03 for H^+ and 1.36 for O^+; that is, the energy spectrum of H^+ becomes harder after the onset than that of O^+. In order to examine which case is dominant, they statistically examine the energy spectra of the ions and calculate spectral index k.

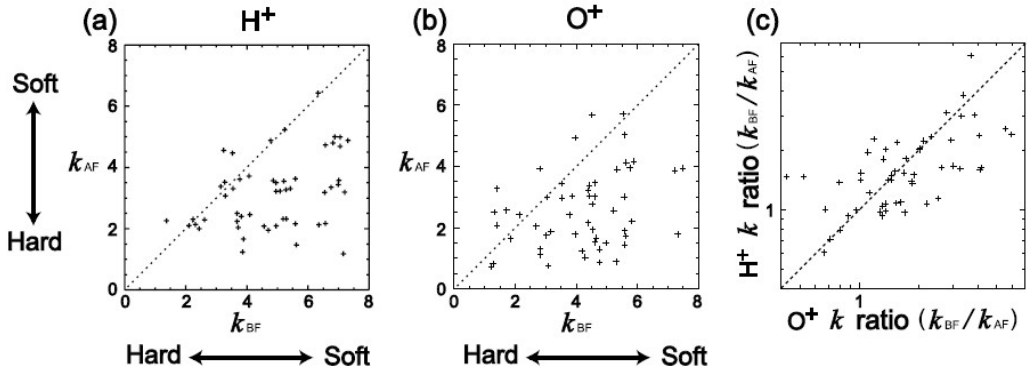

Fig.2.8 (a and b) The relationship between spectral index before onset (k_{BF}) and that after onset (k_{AF}). (c) The relationship between k ratio (K_{BF}/K_{AF}) of H^+ and that of O^+. The number of events used in each plot is 54 (taken from Fig.4 of [*Ono, et al.*, 2009]).

The total number of events found for this analysis is 54. The results are summarized in Fig.2.8. In Fig.2.8a and Fig.2.8b the horizontal and vertical axes show the index before (K_{BF}) and after (K_{AF}) an onset, respectively. Almost all events are distributed below the diagonal line, implying that the energy spectra of H^+ and O^+ become harder after a substorm onset than before in almost all events. Fig.2.8c shows the k ratio (K_{BF}/K_{AF}) of H^+ ions versus that of O^+ ions. There are 30 events in which the k ratio of O^+ is larger than that of H^+ (the events located below the diagonal line) and 24 events otherwise (the events located above the line). It has been considered by previous studies that most events are distributed below the diagonal line. However, the present statistical analysis finds almost the same number of events located below and above the diagonal line.

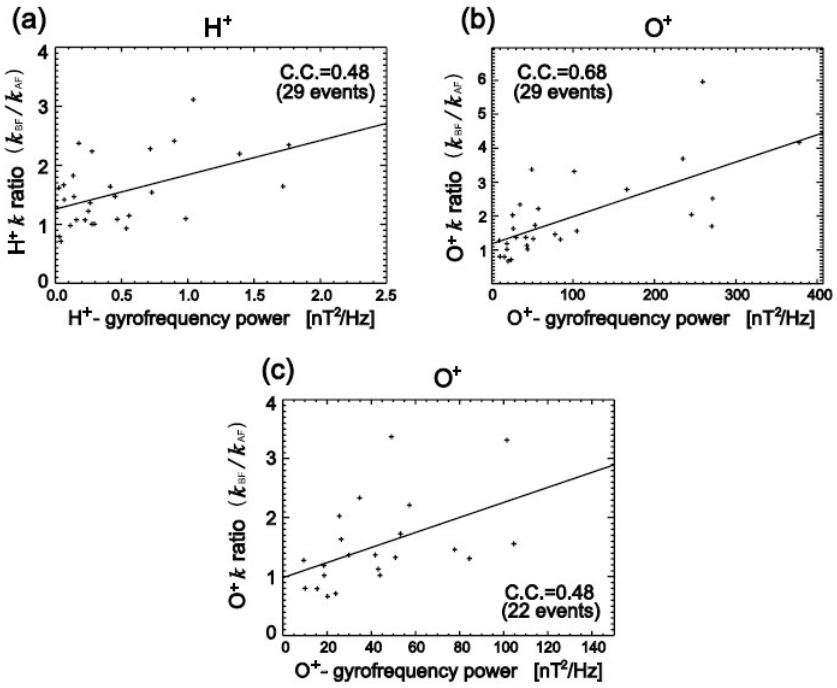

Fig.2.9 The relationship between (a) the H^+ k ratio and the H^+ gryofrequency power and (b) the O^+ k ratio and the O^+ gyrofrequency power. (c) Enlargement of a part of Fig.2.9b with O^+ gyrofrequency power$\leq$ 150 nT ^{2}/Hz and O^+ k ratio≤ 4 (taken from Fig.9 of [*Ono, et al.*, 2009]).

Why is the spectral index ratio (K_{BF}/K_{AF}) of H^+ larger than that of O^+ in some cases, and smaller in others? By statistics, they found that a magnetic field change with the field-reconfiguration time scale (a few to tens of minutes) does not affect the energy spectrum (see Fig.7 of *Ono, et al.*, 2009). Then they focus on fluctuations with a shorter time scale (i.e., magnetic field fluctuations) frequently observed during dipolarization [*Lui et al.*, 1988; *Ohtani et al.*, 1995]. The relationship between the H^+ (or O^+) gyrofrequency power and the H^+ (or O^+) k ratio for 29 events is shown by Fig.2.9. The linear-correlation coefficients (C.C.) are obtained to be 0.48 for H^+ and 0.68 for O^+. Therefore the H^+ (or O^+) gyrofrequency power and the H^+ (or O^+) k ratio are correlated to each other. Since most events (22 events out of 29 events) in Fig.2.9b have power less than 150 nT^2/Hz and smaller k ratios than 4, they calculate the correlation for only these events (Fig.2.9c). Consequently, they again find a positive correlation: the coefficient is 0.48. Thus, they conclude that the k ratio of each ion is positively correlated with the power of waves whose frequencies are close to the

ion-gyrofrequency. Finally, they conclude that ions are nonadiabatically accelerated by the electric field induced by the magnetic field fluctuations whose frequencies are close to ion gyrofrequencies.

The above studies inspire us that the nonadiabatic acceleration can occur in regions much closer to the Earth than previous view, because the magnetic field fluctuations can possibly have the same frequency as the gyration frequency of the ions in the near-Earth region. In Chapter 3, we present a specific energy flux structure of ions that were closely associated with the magnetic field fluctuations. We found that the observed energy spectrum of ions after “wave induced” nonadiabatic acceleration well fits to a spectrum derived from the equation of particle motion presented by *Delcourt et al.* [1997].

Chapter 3 Specific energy flux structures formed by the nonadiabatic accelerations of ions

We examine the Cluster and Double Star TC-1 data from 2005 to 2009 when the spacecraft have an orbit crossing the plasma sheet in the range of 5-10 R_E of the tail. A specific ion energy flux decrease/hole structure, which was associated with the magnetic field fluctuations during dipolarization phase, was frequently observed. In this Chapter, we choose a typical case observed on 30 October 2006 and present its characteristics in detail. The CIS instruments aboard Cluster 1 (SC1), SC3 and SC4 have similar observations (CIS aboard SC2 has no data).

3.1 Observations by CIS instrument

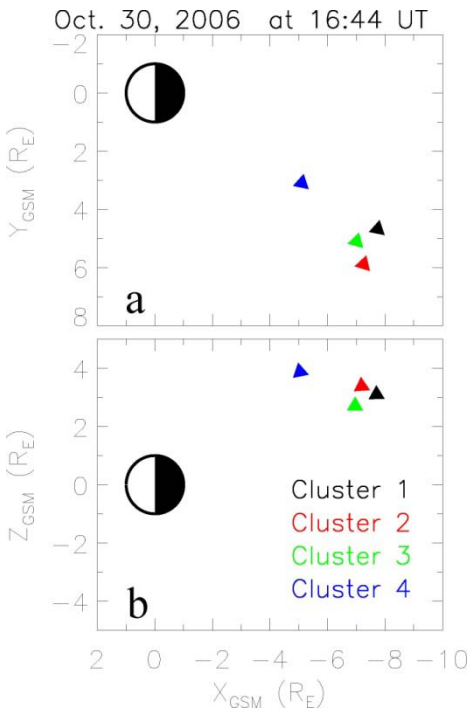

Fig.3.1 Cluster spacecraft positions projected to the X-Y and X-Z planes in GSM coordinates at 16:44 UT on 30 October 2006.

Fig.3.1 shows the relative positions of the Cluster spacecraft in GSM coordinates at 16:44 UT on 30 October 2006. Panel (a) and (b) are the projections of positions in

the X-Y and X-Z planes. The black, red, green and blue colors represent Cluster spacecraft SC1, SC2, SC3 and SC4 respectively.

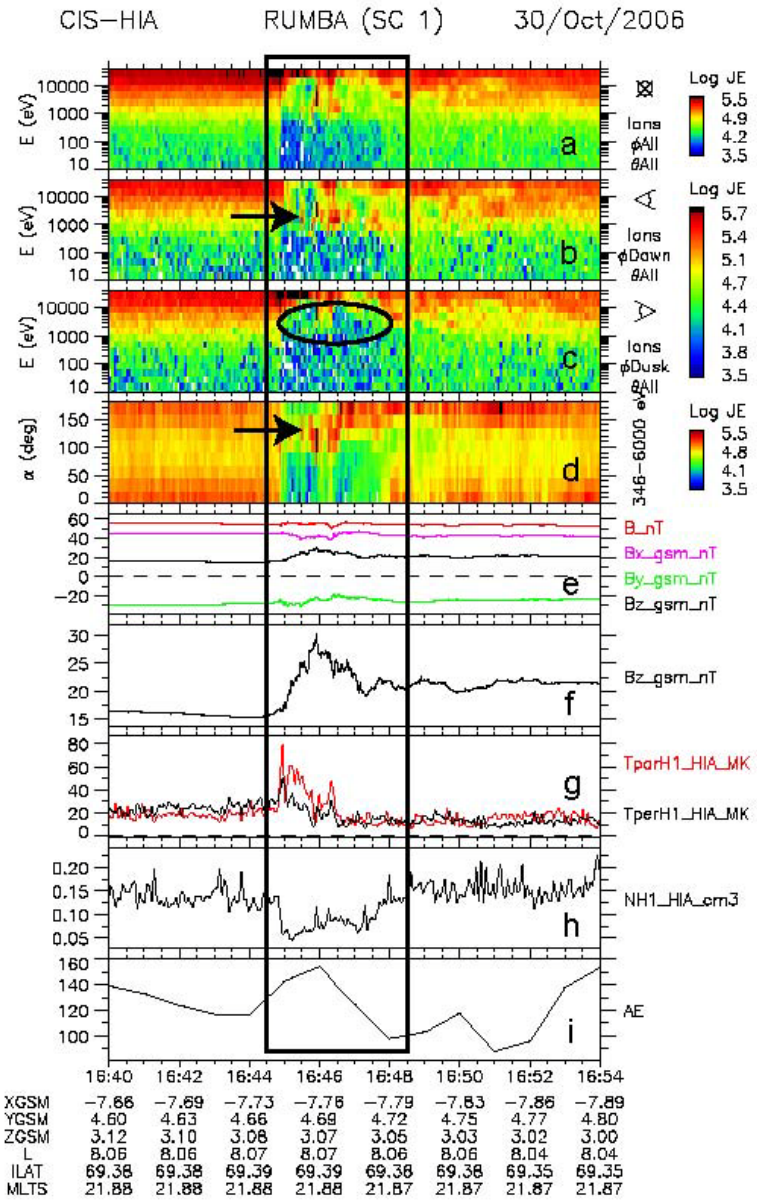

Fig.3.2 The energy-time spectrograms by HIA data of SC1 on 30 October 2006. Panel (a) is the omni-directional ion energy flux. Panels (b) and (c) are the profiles for particles arriving from the dawn (b) and from the dusk (c). Panel (d) is the pitch angle for the particles in the 346 eV-6 keV energy range. Panel (e) is the magnetic field magnitude and the three components in GSM coordinates. Panel (f) shows alone the B_z component. Panel (g) shows the parallel and perpendicular temperatures. Panel (h) is the ion number density. Panel (i) is the AE index.

Fig.3.2 shows the ion measurements recorded by CIS-HIA onboard SC1 from 16:40 UT to 16:54 UT on Oct. 30, 2006. The spacecraft trajectory in GSM coordinates and L index are listed at the bottom of the figure. The black rectangle window denotes the time interval (16:44:30 UT-16:48:30 UT) within which the ion energy flux variations were observed.

The magnetosphere was weakly disturbed during this time since the AE index was between 120 and 150 nT (see Panel (i)). SC1 was located at a tail distance of ～8 R_E above the equatorial plane. The ion spectrum had an energy abundance ranging from 1 keV to 40 keV and the ion number density was between 0.1~0.2, indicating that SC1 was in the plasma sheet. The B measurements show that during the interval 16:45-16:48 UT magnetic field had strong wave activities (see Panel (e)). We calculated the wave propagation direction by using the MVA (minimum variation analysis) method. The angle between the ambient magnetic field and the wave propagation direction is 5.5°, indicating that the wave propagates along magnetic field. Besides, the steep decrease of B_x and increase of B_z at 16:45 UT show that it was a dipolarization process.

Panel (a) also shows that during the interval 16:45-16:48 UT, there was a prominent energy flux decrease of ions over 10 eV-20 keV (referred to as 'energy flux holes' hereinafter), which was accompanied by rapid variations of B field. SC3 and SC4 observed the similar incidents almost at the same time. Since the inter-satellites distance was very large (～3000 km), the structure was a temporal variation. The missing of ions over 10 eV-20 keV was due to the nonadiabatic acceleration of particles caused by the simultaneous wave activities in the B field, which was evidenced later by simulations. Since the missing ions were accelerated up to higher energy, the RAPID instrument recorded sudden proton differential flux increase over 28-70 keV (show in the following section).

We notice that inside the energy flux holes, some ions sporadically appeared over 500 eV-5 keV (referred to as 'sporadic ions' hereinafter). The pitch angle spectrogram for the ions in the energy range 346 eV-6 keV in Panel (d) shows that

these particular ions had pitch angles mainly between 130° and 180° as indicated by the arrow in Panel (d). This means that the ions were moving basically anti-parallel with respect to magnetic field lines. Considering the directions of the field lines on the dusk side of the north magnetotail where SC1 was located, and the ion moving direction, it is easy to understand why the sporadic ions can be observed only in the energy spectrum of the dawn-arriving ions in Panel (b) (indicated by the arrow). In the energy spectrum of the dusk-arriving ions in Panel (c), there is no sporadic ion. Therefore, the isotropic energy flux holes can be more clearly seen in the energy spectrum of Panel (c) (indicated by the ellipsoid).

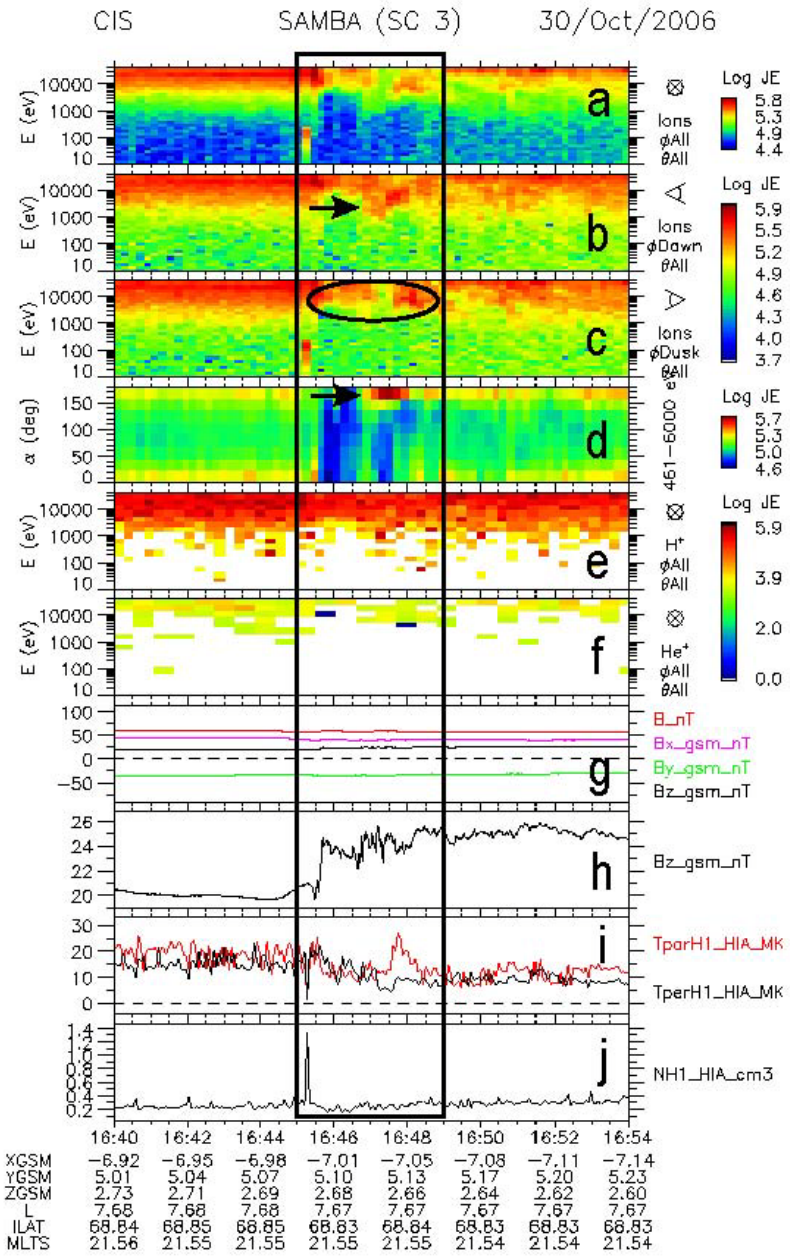

Fig.3.3 The energy-time spectrograms by CIS data of SC3 on 30 October 2006. Panel (a) is the omni-directional ion energy flux. Panels (b) and (c) are the profiles for particles arriving from the dawn (b) and from the dusk (c). Panel (d) is the pitch angle for the particles in the 461 eV-6 keV energy range. Panel (e) is the H^+ energy flux. Panel (f) is the He^+ energy flux. Panel (g) is the magnetic field magnitude and the three components in GSM coordinates. Panel (h) shows alone the B_z component. Panel (i) shows the parallel and perpendicular temperatures. Panel (j) is the ion number density.

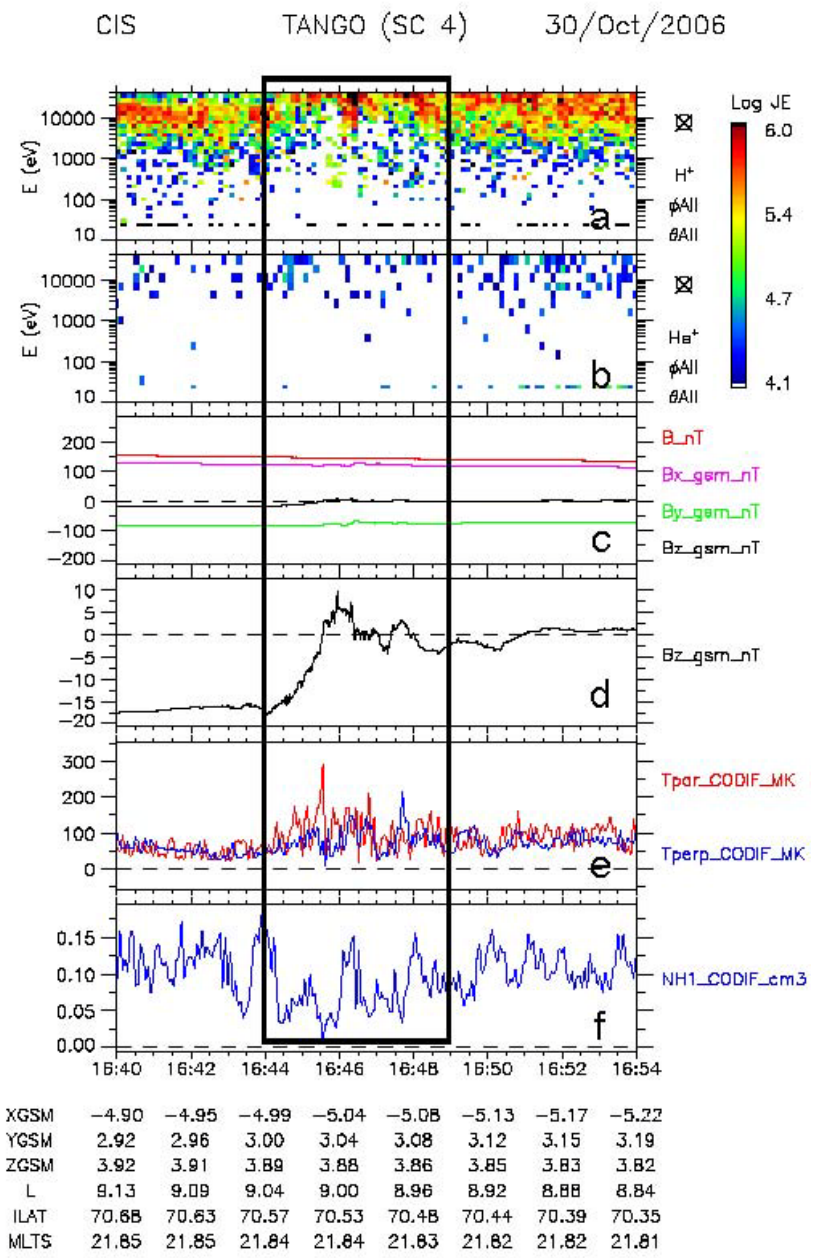

Fig.3.4 The energy-time spectrograms by CIS/CODIF data of SC4 on 30 October 2006. Panel (a) is the H^+ energy flux. Panel (b) is the He^+ energy flux. Panel (c) is the magnetic field magnitude and the three components in GSM coordinates. Panel (d) shows alone the B_z component. Panel (e) shows the parallel and perpendicular temperatures. Panel (f) is the proton number density.

At the same time, SC3 also observed the specific energy flux variations of ions. Fig.3.3 shows the observations of SC3. The magnetic field increased more suddenly than SC1 (see in panel (h)). The ‘energy flux holes’ and the ‘sporadic ions’ inside the

holes seen in SC1 were also clearly observed by SC3 (see in panel (a, b, c)). The pitch angles of the sporadic ions were distributed more focused on 180° (see in panel (d)). We add spectrum of H^+ and He^+ components in panel (e) and (f) of Fig.3.3, thanks to the available data of CIS/CODIF aboard SC3 during that period. Similar energy flux variations can be viewed in the two components as well.

Besides, CODIF/CIS aboard SC4 also recorded the specific energy flux structures of ions almost at the same time. Fig.3.4 gives the observations of SC4. Only the CODIF data were given in the Figure due to the lack of HIA data. During the period when the B_z increased (see in panel (d)), the energy flux of H^+ decreased obviously over 10 eV-20 keV (see in panel (a)). However the energy flux variations of He^+ were not clearly identified in the figure due to the very small amount of He^+ ions detected (see in panel (b)).

3.2 Observations by EFW and RAPID instruments

Fig.3.5 shows measurements of proton differential flux (a) and 28-92 keV flux (b) by RAPID, and duskward electrical field (c) by EFW onboard SC1. As seen in Panels (a) and (b), the proton differential flux increased evidently over 28-70 keV during dipolarization. Unfortunately, the ions 3-D distributions are not available, because of the 'donut' effect (lack of data within 30° of the ecliptic plane) of the detector. At the same time the duskward electric field (E_{dusk}) measured by EFW instrument suddenly increased up to 30 mV/m (see Panel (c)). The large enhancement of E_{dusk} is deemed to be a transient electric field induced by the magnetospheric dipolarization. Specifically the E_{dusk} modulated by the satellite spin with a period of 4s data was characterized by periodic impulse. The frequency distributions of the magnetic and electric field fluctuations reveal that there is a close correlation between them (see below). Moreover, we calculated the value of $-(V\times B)_y$ and the large discrepancies between E_{dusk} and $-(V\times B)_y$ indicate that the plasma frozen condition was broken down during that interval.

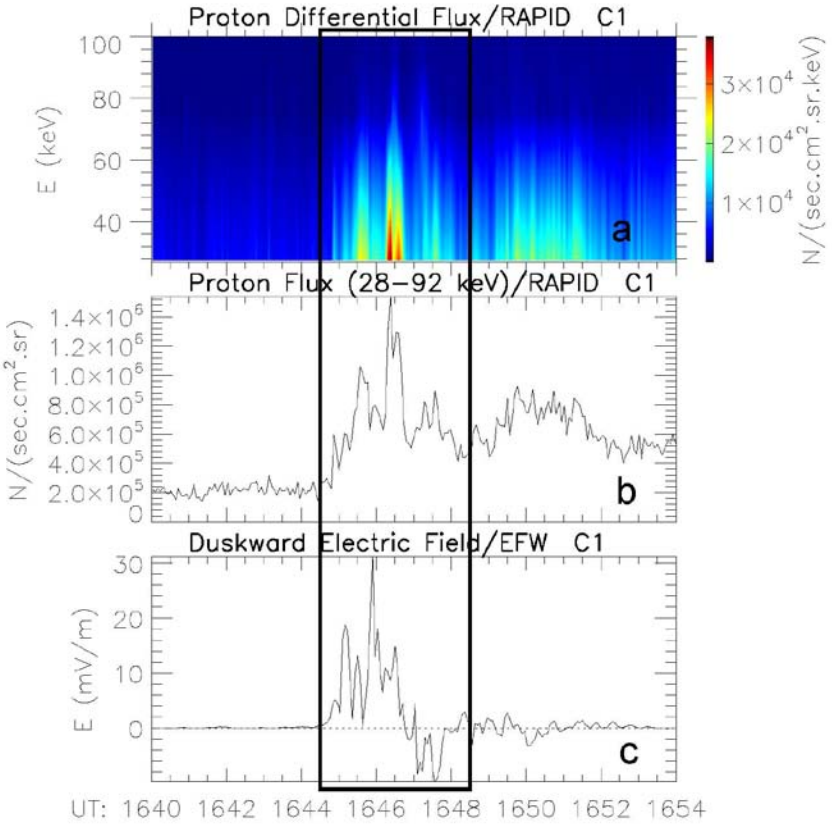

Fig.3.5 Proton differential flux (a), 28-92 keV proton flux (b) and the duskward electric field (c) observed by RAPID and EFW instruments onboard SC1 on 30 October 2006.

Fig.3.6 shows the same observations by RAPID and EFW aboard SC3. The differential flux of H^+ also increased distinctly over 28-92 keV during magnetic field dipolarization. The primary dissimilarity is that the duskward electric field enhancement was only 5 mV/m (see Panel (c)), much smaller than the observations of SC1. Similar differential flux increase of ions and duskward electric field enhancement were also observed by RAPID and EFW aboard SC4 (see in Fig.3.7).

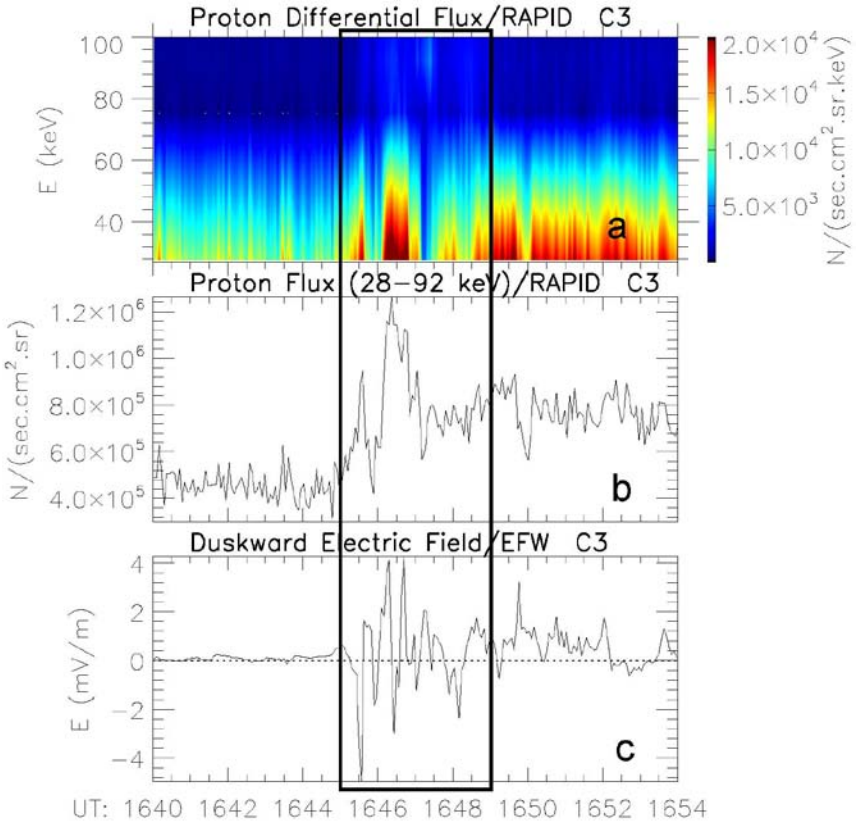

Fig.3.6 Proton differential flux (a), 28-92 keV proton flux (b) and the duskward electric field (c) observed by RAPID and EFW instruments onboard SC3 on 30 October 2006.

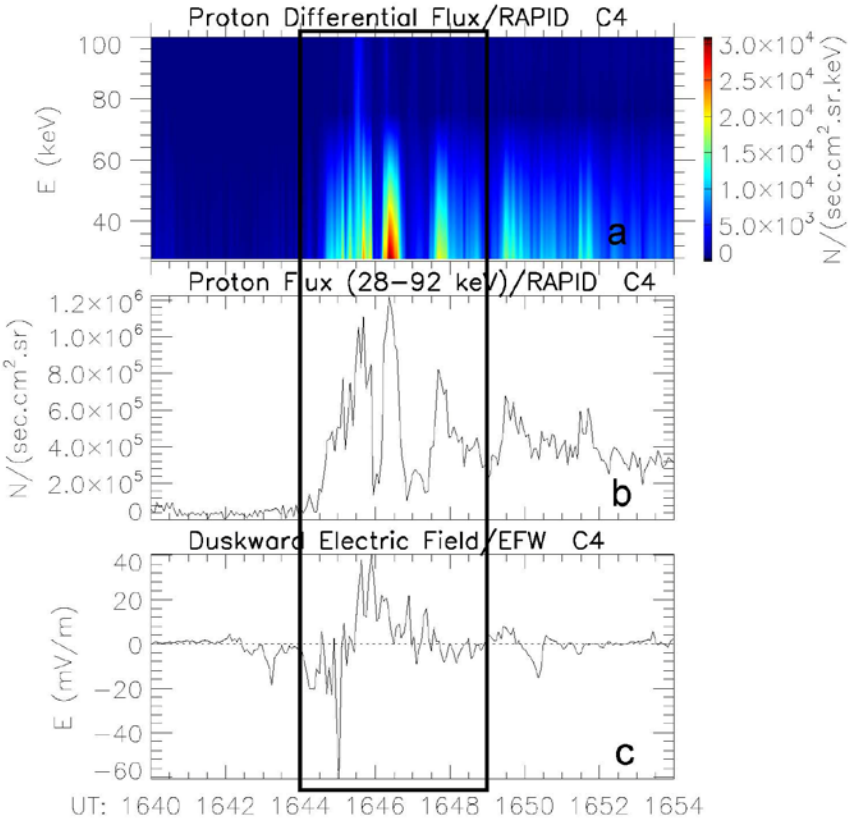

Fig.3.7 Proton differential flux (a), 28-92 keV proton flux (b) and the duskward electric field (c) observed by RAPID and EFW instruments onboard SC4 on 30 October 2006.

3.3 Wavelet analysis of the magnetic and electric field

To more clearly investigate the B and E field fluctuations, we perform the wavelet analysis on the two fields. Fig.3.8 illustrates the Power Spectral Densities (PSDs) calculated from the full resolution magnetic field data (22.417 vectors/s) of SC 1. The magnetic field data are rotated into the field-aligned coordinate system, in which the compressional component (B_{com}) is aligned with the ambient magnetic field direction B (positive northward), the toroidal component (B_{tor}) is transverse to B in the azimuthal direction (positive eastward), and the poloidal component (B_{pol}) is transverse to B in the magnetic meridian plane (positive inward). The black solid and dashed lines in Panels (a)-(c) represent the gyrofrequencies of H^+ and He^+ respectively. Panel (d) shows the magnetic field B_z component with the black solid lines scaled to

the left axis, and the magnetic elevation angle θ with the red solid lines scaled to the right axis, which is defined as $\theta = \tan^{-1}(B_z/(B_x^2 + B_y^2)^{1/2})$. The magnetic field fluctuations and dipolarization can be distinctly seen from this panel.

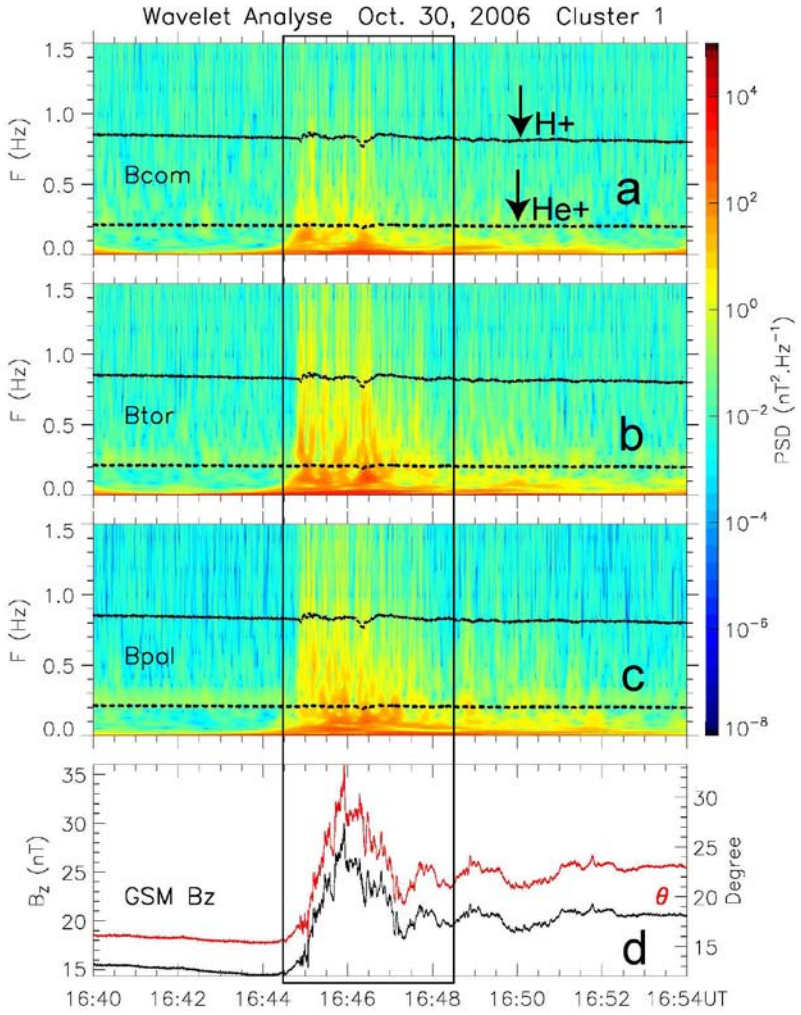

Fig.3.8 Wavelet analyses for magnetic field of SC1 in the field-aligned coordinate system on 30 October 2006 (a, b, c). The black solid and dashed lines represent the gyrofrequencies of H^+ and He^+. The black and red lines in Panel (d) show the magnetic field B_z component and the magnetic elevation angle θ in GSM coordinates.

As seen in the Panels (a)-(c), intensive Ultra Low Frequency (ULF) waves emerge right at the interval when the "energy flux hole" structure arose. They are more dominant in the toroidal and poloidal components than in the compressional component. This implies that they are mainly transverse MHD waves propagating

along the field lines. The broadband wave power starts from the extremely low frequency and extends up to the gyrofrequency of H^+ around 1 Hz. The main wave power of the compressional component (Panel (a)) is right below the gyrofrequency of He^+. For the toroidal (Panel (b)) and poloidal (Panel (c)) components, the most intense wave packets are also below the gyrofrequency of He^+, and the broadband waves extend up to the gyrofrequency of H^+. SC3 and SC4 have similar observations as SC1 (see Fig.3.9 and Fig.3.10).

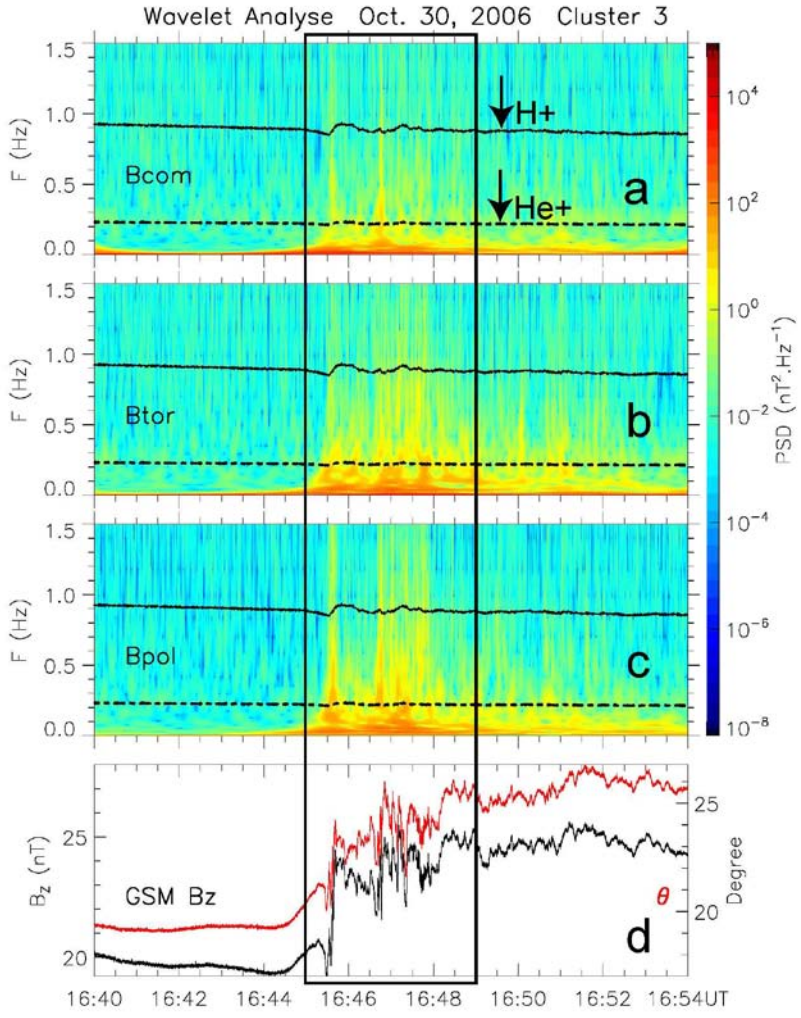

Fig.3.9 Wavelet analyses for magnetic field of SC3 in the field-aligned coordinate system on 30 October 2006 (a, b, c). The black solid and dashed lines represent the gyrofrequencies of H^+ and He^+. The black and red lines in Panel (d) show the magnetic field B_z component and the magnetic elevation angle θ in GSM coordinates.

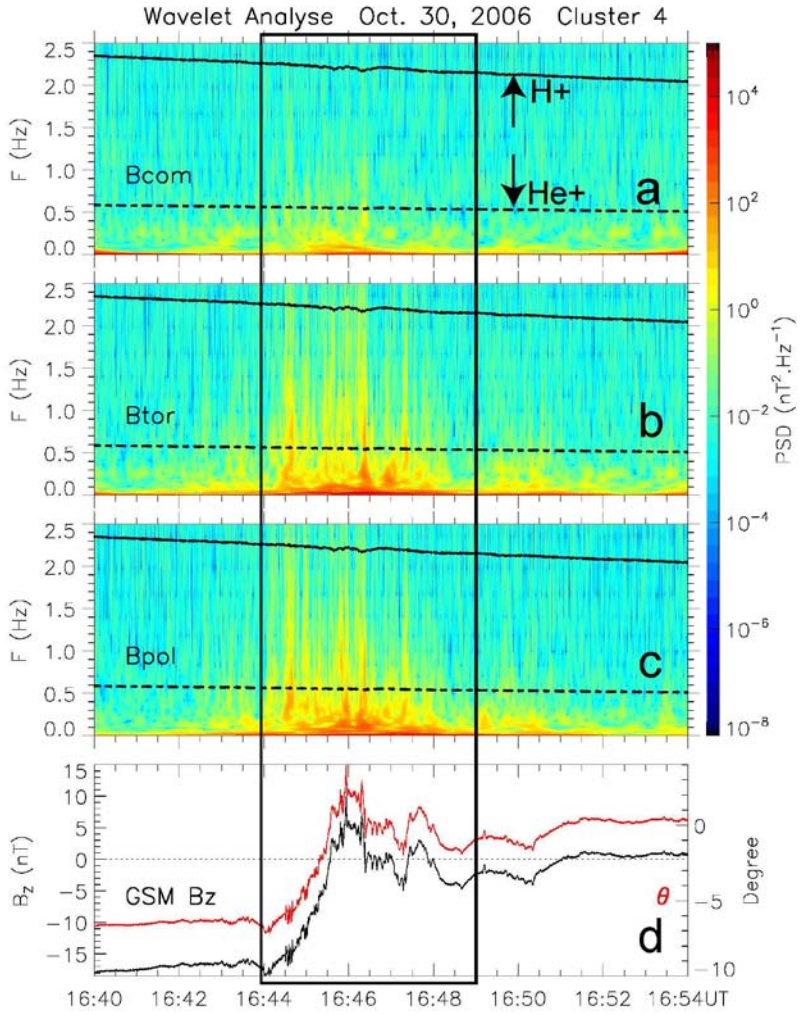

Fig.3.10 Wavelet analyses for magnetic field of SC4 in the field-aligned coordinate system on 30 October 2006 (a, b, c). The black solid and dashed lines represent the gyrofrequencies of H^+ and He^+. The black and red lines in Panel (d) show the magnetic field B_z component and the magnetic elevation angle θ in GSM coordinates.

These features indicate that the waves belong to the ElectroMagnetic Ion Cyclotron (EMIC) waves (0.1-5 Hz), which normally exhibit spectral power right below the hydrogen (H^+), helium (He^+) and oxygen (O^+) ion gyrofrequencies [*Summers et al.*, 2003]. The EMIC source region is typically confined near the geomagnetic equator [*Thorne*, 2010]. The wave group velocity is closely aligned with the magnetic field direction, allowing the waves to propagate to the Earth where they are observed in the Pc1 and Pc2 bands [*Engebretson et al.*, 2008]. Newly generated

EMIC waves are transverse, left-hand polarized waves [*Kennel and Petschek*, 1966]. These characteristics are consistent with our observations mentioned above.

A main source of free energy for the excitation of magnetospheric EMIC wave is the anisotropic distribution of hydrogen ions ($T_{perp}>T_{paral}$) [*Summers et al.*, 2003]. Fig.3.2g shows that the temperature of the two components were basically equal during dipolarization, sometimes the parallel temperature was even larger than the perpendicular one. Therefore the generation conditions of anisotropic ion distribution for EMIC waves are not satisfied. However, *Lui et al.* [2008] proposed that the EMIC instability can be driven by gradient B drift of ions. They derived the dispersion relation to identify plausible wave modes on the basis of a two-fluid approach. Here we introduce the situation with a finite ion drift and ion temperature isotropy. In the case of parallel propagation, two unstable solutions are found. One is a direct analog of the EMIC instability, while the other is an electromagnetic version of the Weibel instability which is driven by the cross-field drift rather than the temperature anisotropy [*Lui et al.*, 1991]. For the perpendicular propagation, they find an ordinary mode instability which is also excited by the cross-field ion drift. Since the EMIC waves presented in our observations have parallel propagation direction and ion temperature isotropy, the drift-induced EMIC instability may be highly relevant to the excited magnetic fluctuations in the vicinity of the local ion cyclotron frequency that coincides with the dipolarization.

Besides the magnetic field, we also perform the wavelet analyses for the full resolution data (22.417 vectors/s) of duskward electric field E_y, because they have distinct impulsive feature. In Fig.3.11, the PSDs of the duskward electric field of SC3 (although have some regular spiky noise) was shown to be highly analogous to that of the magnetic field in terms of the broadband wave power starting from the extremely low frequency and extending up to the gyrofrequency of H^+. The PSDs both in E and B fields indicates that broadband electromagnetic waves were excited in the plasma sheet at that interval. Consequently the gyromotions of ions were possibly perturbed due to the existence of the electric field disturbances around H^+ gyrofrequency, which

is a favorable condition for the ions to be accelerated in nonadiabatic mechanism. Similar results were also found on E_y of SC4 (see Fig.12). The lack of the same analyses for SC1 was due to the absent of high resolution electric field data during that period.

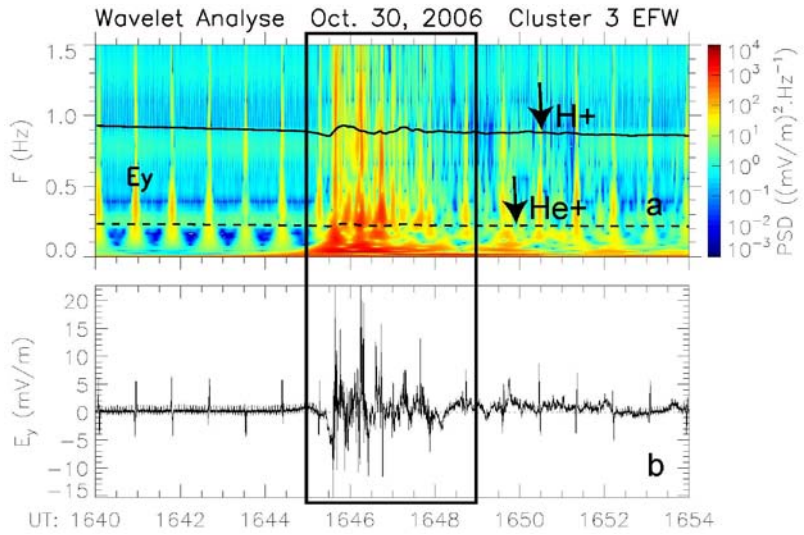

Fig.3.11 Wavelet analyses for the duskward electric field E_y of SC3 on 30 October 2006. The black solid and dashed lines represent the gyrofrequencies of H^+ and He^+.

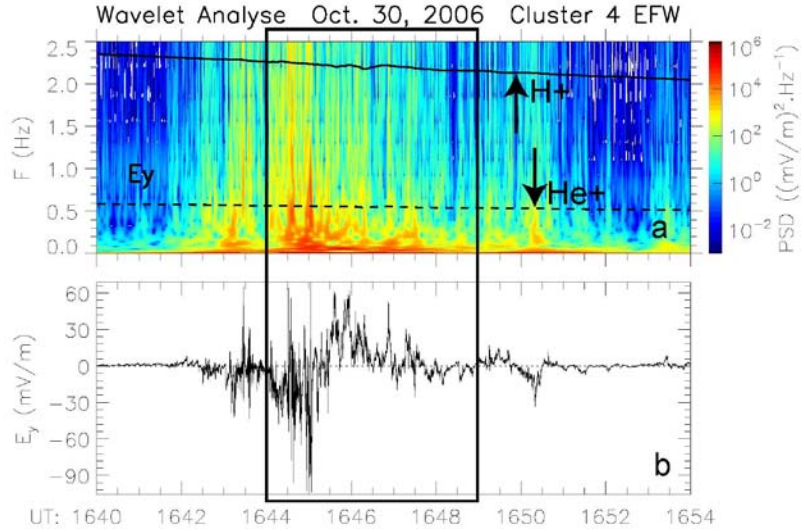

Fig.3.12 Wavelet analyses for the duskward electric field E_y of SC4 on 30 October 2006. The black solid and dashed lines represent the gyrofrequencies of H^+ and He^+.

3.4 Discussion about the formation of the 'energy flux holes'

In Section 3.1-3.3, we presented the observation of an energy flux decrease/hole structure of ions over 10 eV-20 keV in the energy spectrum. The 28-70 keV proton differential flux was observed to increase simultaneously. Moreover, the ion flux variations both in low and high energy range were found to correlate well with the broadband magnetic field fluctuations. The good correlations imply that the magnetic field fluctuations during magnetospheric dipolarization are directly related to the ion energy flux variations. In this section we will give a more detailed discussion about their generation mechanisms.

The previous studies have found that the EMIC waves take effect only with electrons or low energy ions. E.g. *Ukhorskiy et al.*, [2010] showed that the resonant interaction of the electrons in the radiation belt with the EMIC waves can scatter the electrons into the atmospheric loss cone. Also the EMIC waves can interact resonantly with low energy He^+ (energized from tens of eV up to 1 keV) [*Zhang et al.*, 2010]. It was found that, the He^+ heating by the EMIC waves is preferential [e.g. *Anderson and Fuselier*, 1994; *Fuselier and Anderson*, 1996]. In other words, the EMIC waves interact resonantly with He^+ but non-resonantly with H^+ [*Zhang et al.*, 2010]. Many other wave modes can potentially heat ions via resonant interaction near ion gyrofrequencies. However, the energy of the accelerated ions is low, e.g., H^+ below 200 eV [*Bogdanova et al.*, 2004].

Now we discuss the possible formation mechanism of the energy flux holes by using the non-adiabatic acceleration theory. As mentioned in the introduction, the nonadiabatic behavior normally occurs in two ways: spatial and temporal.

3.4.1 Possibility of nonadiabatic acceleration by spatial variations of the magnetic field

First, to verify whether the first adiabatic invariant is conserved spatially, we need calculate the κ parameter (square root of the ratio between the minimum radius

of curvature of the magnetic field lines and maximum Larmor radius for a particle of a given energy). Then the radius of the field line curvatures have to be calculated first. We use the analysis technique of MRA (Magnetic Rotation Analysis) designed by *Shen et al.* [2003, 2007] to calculate the radius of curvature.

It is based on estimating the gradient tensor of four-point measurements of the magnetic field, which have been taken by the Cluster mission. The method first constructs the symmetrical magnetic rotation tensor and in general terms deduces the rotation rate of magnetic field along one arbitrary direction. The value of the curvature of a magnetic field line is given by the magnetic rotation rate along the magnetic unit vector and its corresponding radius of curvature is readily obtained. Generally the constraint to MRA is L/D <1, and the relative errors of the curvature value and curvature radius of the field lines are both at the first order of L/D, where D is the typical spatial scale of the magnetic structures, and L is the size of the Cluster tetrahedron. Note that we only consider H^+ in the following discussion because H^+ is the dominant component of the plasma sheet. In the event on 30 October 2006, D is 8 R_E (estimated by the calculated radius of curvature), L is 20000 km (estimated by the maximum distance between the spacecraft). L/D=0.39<1, then the technique is applicable for our event and the calculated value is valid.

In this event (based on the observations of SC1), the Larmor radius of proton for 1-10 keV is 60-190 km. We calculated the larmor radius by using the average magnetic fields of the 4 spacecraft, because the radius of the curvature is also obtained by using the measurements of 4 spacecraft. The radius of the curvature calculated by using MRA is 8 R_E. Then the parameter κ is 15-30, larger than 3. So the first adiabatic invariant is conserved in spatial consideration.

3.4.2 Possibility of nonadiabatic acceleration by temporal variations of the magnetic field

Second, we check whether the magnetic moment and energy of H^+ were conserved in a temporal impulsive electric field induced by the magnetic field fluctuations which was evidently seen in Fig.3.5. It is well know that the charged particle in the constant E×B field will obtain a drift velocity with the magnitude E/B in the gyration plane (see Fig.3.13). How the gyromotion of particles become when the constant E field changed into an impulsive one? *Delcourt et al.* [1997] examined this situation by taking the impulsive electric field of the form

$$E(t) = \frac{E_m}{2}[1 - \cos(\omega_E t)] \qquad (1)$$

where E_m is the maximum electric field and ω_E is the impulse frequency of electric field.

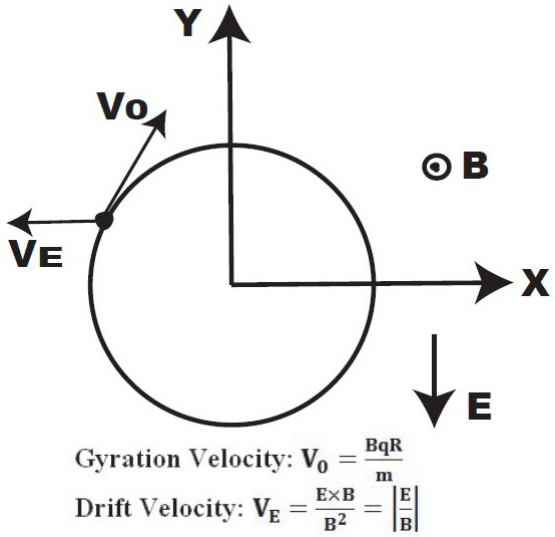

Fig.3.13 The schematic diagram to show the motion of the charged particle in the constant E×B field

They applied *E(t)* into the equation of motion in the gyration plane which is defined as:

$$\dot{V}_X = \omega_c V_Y \qquad (2)$$

$$\dot{V}_Y = -\frac{qE(t)}{m} - \omega_c V_X \qquad (3)$$

where ω_C is the cyclotron frequency. Solving the equations, a first-order description of the two gyrovelocity components can be readily obtained as (more details of the derivation were given in the appendix of their paper):

$$V_X(t) = V_0 \sin(\omega_E \chi t + \psi_0) - \frac{E_m}{2B}\frac{1}{\chi^2-1}[\cos(\omega_E \chi t) - \chi^2 \cos(\omega_E t)] - \frac{E_m}{2B} \quad (4)$$

$$V_Y(t) = V_0 \cos(\omega_E \chi t + \psi_0) + \frac{E_m}{2B}\frac{1}{\chi^2-1}[\sin(\omega_E \chi t) - \chi \sin(\omega_E t)] \quad (5)$$

where χ denotes the ω_C/ω_E ratio, ψ_0 the initial gyration phase and V_0 the initial velocity.

Here we give a physical interpretation about the equation of motion to more clearly understand the electric field acceleration processes. Apparently the motions of the particles are significantly controlled by the crucial parameter χ. So we simplify the equations into three limiting cases according to the variations of χ relative to 1.

(1) $\chi \gg 1$, the electric field variation is much slower than the cyclotron of particles. This enables the equation of motion to be reduced to

$$V_X(t) = V_0 \sin(\omega_C t + \psi_0) - \frac{E_m}{2B}[1 - \cos(\omega_E \chi t)] \quad (6)$$

$$V_Y(t) = V_0 \cos(\omega_C t + \psi_0) \quad (7)$$

The motion of particle described in the equations is highly analogous to that under the constant E×B field except that the drift velocity becomes variable (the second term in (6)).

(2) $0 < \chi \ll 1$ or $\chi \sim 0$, the electric field variation is much faster than the cyclotron of particles. This condition yields

$$V_X(t) = V_0 \sin(\omega_C t + \psi_0) \quad (8)$$

$$V_Y(t) = V_0 \cos(\omega_C t + \psi_0) \quad (9)$$

One can see that the electric field would have no impact on the cyclotron of particles if the impulse frequency was extremely high relative to the cyclotron frequency. Thus it can be expected by this result that the high frequency electric field

impulse in the gyration plane can be ignored when considering the accelerations of particles.

(3) χ~1, the electric field variation is almost in the same frequency as the cyclotron of particles. The motion equations become

$$V_X(t) = V_0 \sin(\omega_E t + \psi_0) + \frac{E_m}{2B}\cos(\omega_E t) - \frac{E_m}{2B} \quad (10)$$

$$V_Y(t) = V_0 \cos(\omega_E t + \psi_0) - \frac{E_m}{4B}\sin(\omega_E t) \quad (11)$$

We denote by V_E the peak E×B drift speed ($V_E = \frac{E_m}{B}$). If $V_0 \gg V_E$, the last terms of the two equations can be ignored. Thus one can find that particles would gyrate with the initial velocity nearly the same as the E impulse absent. In short the high energy particles (relative to the drift velocity) keep adiabatic. If $V_0 \ll V_E$, the first terms of the two equations can be ignored. The equations indicate that besides a drift speed $V_E/2$, the particles would gyrate in a quasi-circular orbit with the increased speed close to $V_E/2$. In short the low energy particles (relative to the drift velocity) are non-adiabatically accelerated when χ~1. If $V_0 \sim V_E$, the orbits of the particles would strongly depend on another parameter the initial gyration phase ψ_0. We take two examples to show the effect:

If $\psi_0=\pi/2$, the motion equations become

$$V_X(t) = (V_0 + \frac{V_E}{2}) \sin\left(\omega_E t + \frac{\pi}{2}\right) - \frac{V_E}{2} \quad (12)$$

$$V_Y(t) = (V_0 + \frac{V_E}{4}) \cos\left(\omega_E t + \frac{\pi}{2}\right) \quad (13)$$

If $\psi_0=3\pi/2$, the motion equations become

$$V_X(t) = (V_0 - \frac{V_E}{2}) \sin\left(\omega_E t + \frac{3\pi}{2}\right) - \frac{V_E}{2} \quad (14)$$

$$V_Y(t) = (V_0 - \frac{V_E}{4}) \cos\left(\omega_E t + \frac{3\pi}{2}\right) \quad (15)$$

These deduced equations illustrate that besides a drift speed $V_E/2$, the particles would gyrate in a quasi-circular orbit with a increased/decreased speed close to

($V_0 \pm V_E/2$), which further reveals that it is possible for the particles to be non-adiabatically accelerated or decelerated in the gyration plane depending on ψ_0 varying between 0° and 360° when $\chi \sim 1$ and $V_0 \sim V_E$.

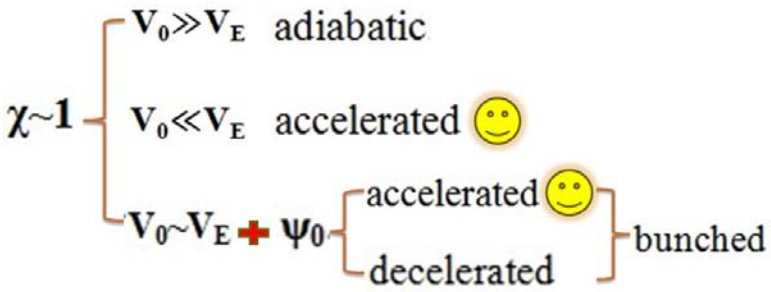

Fig.3.14 The occurring conditions of the non-adiabatic acceleration of ions

We summarize the previous analysis below. Particles have opportunities to be accelerated in the gyration plane under the condition that the cyclotron frequency is close to the impulse frequency of electric field ($\chi \sim 1$) and the initial energy/velocity is lower than the drift energy/velocity ($V_0 \leqslant V_E$). Moreover, the acceleration will also depend on the phase difference between the cyclotron of the particles and the impulsive electric field when $V_0 \sim V_E$ (summarized in Fig.3.14). This process can be more easily understood from the perspective of the energy transfer. When the impulse of the electric field reaches to the same frequency as the cyclotron of the particles, the condition of resonance between each other is satisfied. If the kinetic energy of the particles is lower than the potential energy of the E and B field at that time, energy will certainly transfer from the E and B field to the particles which are consequently accelerated. Yet if the two energies of the particles and field happen to be the same order of magnitude, they start to reconcile each other through the modulation of the gyration phase, which leads to the acceleration/deceleration of the particles depending on their gyrophases. Furthermore, the acceleration/deceleration of particles finally contributes to the gyrophase 'bunching' patterns of the particles, which were supposed to be randomly distributed in gyrophases (see Fig.3.15).

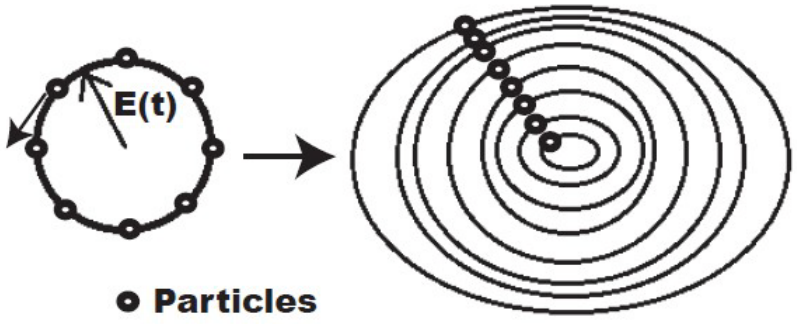

Fig.3.15 The sketch map to show the 'gyrophase bunching effect'

Note that the impulsive electric field in *Delcourt et al.* [1997] was assumed to be induced by the dipolarization of the magnetic field, so the ω_E had the same frequency as the dipolarization. In fact, the impulsive electric field can also be induced by the magnetic field fluctuations with certain frequencies. The key point is the existence of an impulsive electric field which can perturb the gyromotion of particles. Therefore the equations discussed above are still valid for the impulsive electric fields induced by the magnetic field fluctuations. Specifically to the event on 30 October 2006, the proton gyroperiod observed by SC1 was about 1.2s. During the interval of energy flux hole, there were strong broadband impulses of the electric field induced by the magnetic field fluctuations (from tens of mHz to 1.0 Hz), among which including a wave period of 1.1s (0.9 Hz) that was rightly comparable to the gyroperiod of the H^+ (1.2s), therefore the condition of χ~1 was satisfied and the ions were possibly accelerated non-adiabatically by these waves.

Based on equations (4) and (5), equation (16) can be deduced to describe the relationship between the final velocities of ions with the initial gyration velocity V_0 in the course of nonadiabatic acceleration (more details of the derivation were given in *Delcourt et al.* [1997], and the validity of this analytical estimation was confirmed by its good agreement with the numerical trajectory calculations in their paper as well):

$$(V_{final}^2)_{\pm} = \frac{B_{final}}{B_{initial}}\left[V_0 \pm V_E \frac{\sin\pi\chi}{(\chi^2-1)}\right]^2 \qquad (16)$$

$B_{initial}$ and B_{final} are the initial and final magnetic field magnitudes, respectively. V_{final}^2 has both positive and negative values are because of the particle initial phase ψ_0 varying between 0° and 360°.

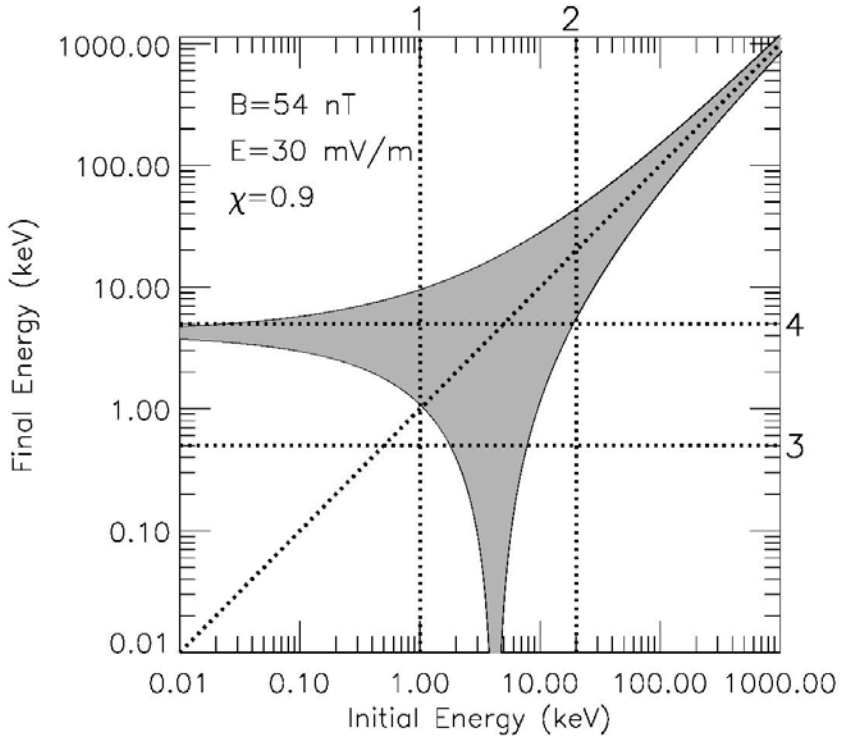

Fig.3.16 Final energy versus initial energy for H^+. For each initial energy, the shaded area gives the final energy range depending on the initial gyration phase of the particles. The two vertical dashed lines 1 and 2 indicate 1 keV and 20 keV initial energies; the two transverse dashed lines 3 and 4 indicate 5 keV and 500 eV final energies.

By using equation (16), we have checked the effect of the broadband frequencies of electric field disturbances on the accelerations of H^+. The results indicate that the acceleration effects reduce remarkably when the frequencies of electric field fluctuations differ considerably from the gyrofrequency of H^+. Specifically, in this event electric field disturbances below 0.5 Hz basically have no influence on the accelerations of H^+ and the most effective accelerations stem from the disturbances near the gyrofrequency of H^+ (0.9 Hz), as is in accordance well with the expectation from the discussions above. So in the calculations of Fig.3.16, 1.1s (0.9 Hz) was

adopted as the impulsive E period. The gyroperiod of the H^+ was 1.2s. Thus we had χ=1.1s/1.2s$\approx$0.9. $B_{initial}$=B_{final}=54 nT (see Fig.3.2e); E_m=30 mV/m (see Fig.3.5c), then V_E can be obtained (V_E=E_m/B). V_0 is variable according to the given initial energy of proton. By using Equation (16) and the parameters above, we plot the final energy versus initial energy for H^+ between 10 eV and 1000 keV in Fig.3.16.

In Fig.3.16, the shaded area gives the range of the final energy depending on the initial energy and gyration phase of the particles. The two vertical dashed lines 1 and 2 indicate 1 and 20 keV of the initial energy (the energy flux holes we observed in Fig.1a was between 10 eV and 20 keV). It is clearly seen that if the initial energy is less than 1 keV, the H^+ is effectively accelerated up to around 4 keV; if the initial energy is more than 20 keV, the energy of the H^+ is basically invariant; if between, H^+ is either accelerated or decelerated depending on their gyration phase. These results can explain well about the formation of the energy flux holes in Fig.3.2a. Ions with energy below 1 keV were accelerated to higher energy by magnetic moment μ enhancement. The corresponding energy flux decrease below 1 keV can be clearly seen in Fig.3.2a. Ions with energy above 20 keV kept adiabatic with energy basically invariant, which creates the upper limit of the energy flux holes; In between ions were either accelerated nonadiabatically to higher energy or decelerated, which forms the energy flux decrease/holes over 1-20 keV.

3.5 Discussion about the ‘sporadic ions’ inside the energy flux holes

The transverse dashed lines 3 and 4 in Fig.3.16 indicate 500 eV and 5 keV of the final energy, which is the main energy range of the sporadic ions inside the energy flux holes. As seen in Fig.3.16, these ions are composed of the accelerated ions from the lower energy (<1 keV) and the decelerated/accelerated ions over 1-20 keV. To identify which part is the dominant component, we plot the particle flux measured by HIA instrument on board SC1 in Fig.3.17. Note that the unit of the particle flux is particles/(sec•cm2•sr•keV), different from the energy flux in Fig.3.2a whose unit is

keV/(sec•cm2•sr•keV). An apparent particle flux decrease was observed below 1 keV during the interval of black rectangle, which suggests that the sporadic ions in Fig.3.2a were mainly the accelerated ions from below 1 keV.

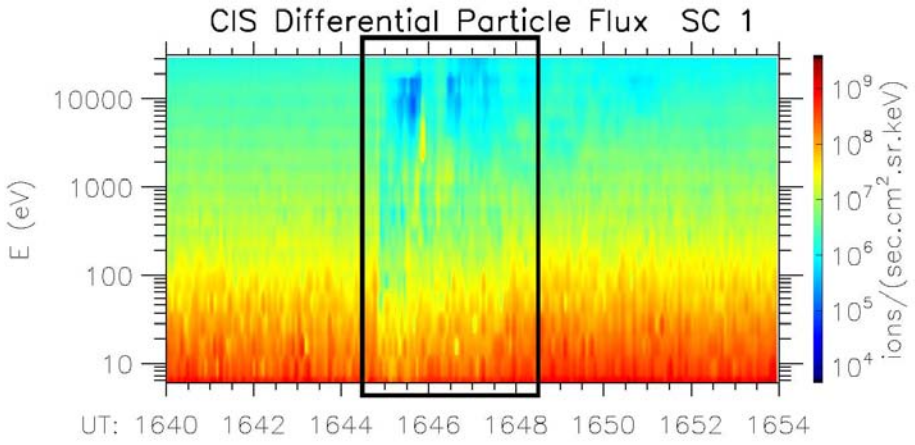

Fig.3.17 The particle flux measured by HIA instrument on board SC1 on 30 October 2006.

As mentioned in Chapter 2, *Delcourt et al.* [1990] examined the ion trajectories during dipolarization by means of three-dimensional particle codes. In the direction parallel to the magnetic field, a centrifugal acceleration related to the rapid E×B transport account for the creation of new high-altitude mirror points. It is showed that particles initiated above the equator, instead of traveling northward, they are rapidly reflected toward the opposite hemisphere following high-altitude mirroring, with the final pitch angle of 130°-180° (trajectory 2 in Fig.2.2d, Fig.2.3d). Since our observations were also at the north of the plasma sheet, this result well explains the observed pitch angle distributions of the sporadic ions.

What is more, *Delcourt et al.* [1997] found that ions transported in a nonadiabatic manner, not only experience large magnetic moment variations but also prominent bunching in gyration phase. So, if the sporadic ions inside the energy flux holes experienced nonadiabatic acceleration by the magnetic field fluctuations, they should also experienced gyrophase bunching effect, with the final phase identical regardless of their initial phase.

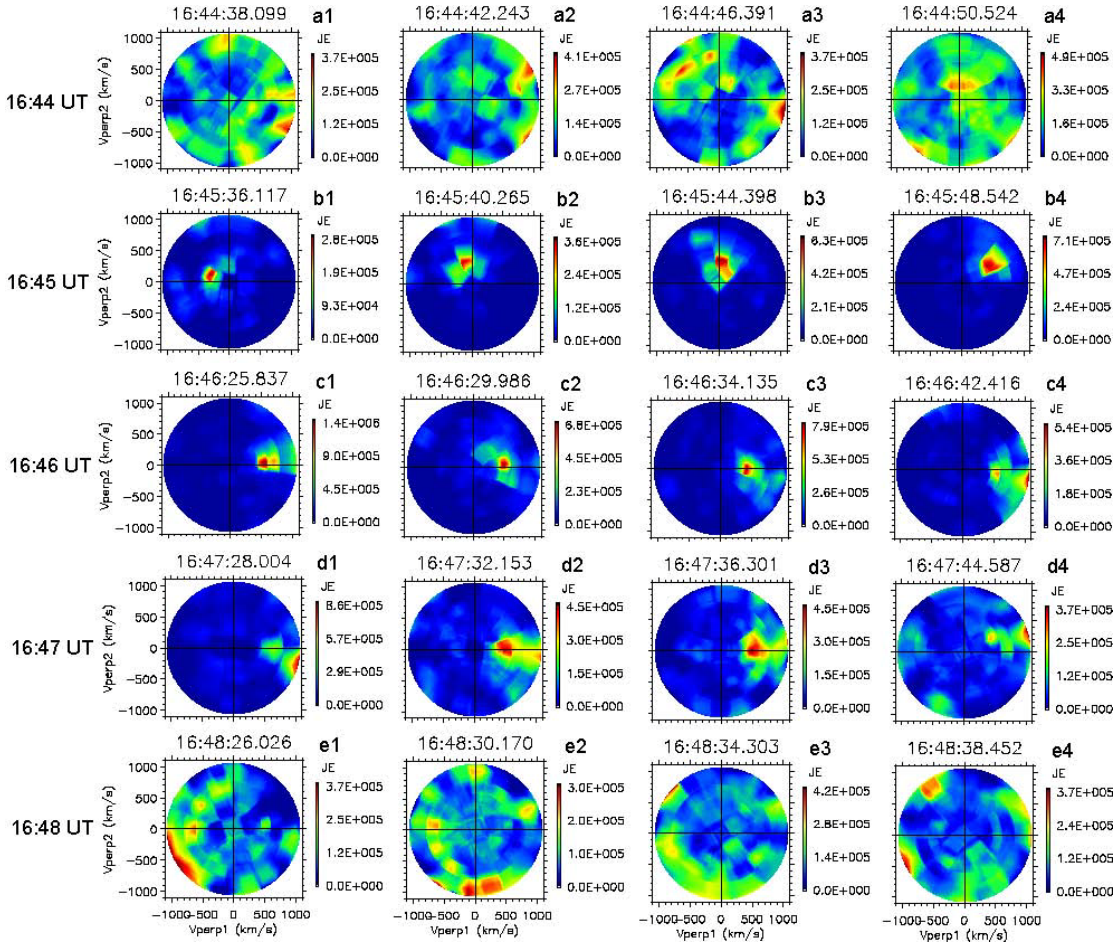

Fig.3.18 Ion distribution functions in the plane perpendicular to the magnetic field for ions between 500 eV and 5 keV. The data are obtained from HIA instrument onboard SC1 during 16:44-16:48 UT on 30 October 2006.

To examine the gyration phase patterns of the sporadic ions, we plot the ion distribution functions in the plane perpendicular to the magnetic field for ions between 500 eV and 5 keV during 16:44-16:48 UT in Fig.3.18. Initially at 16:44 UT, the ions were in chaotic distribution. Next when the magnetic field fluctuations and the sporadic ions began to appear during 16:45-16:47 UT, these ions became evidently concentrated at a certain phase space, i.e. they were bunched in gyrophase. Until the magnetic field fluctuations gradually disappeared at 16:48 UT, the ions restored to be chaotic distribution. These signatures further demonstrate that the sporadic ions had experienced nonadiabatic acceleration caused by the magnetic field fluctuations. Moreover the observed gyrophase bunching patterns of ions correspond

well to the theory expectations mentioned above, which has never been reported in the plasma sheet.

Particles underwent nonadiabatic acceleration have two-step behavior (*Delcourt et al.* 1997): "(1) a rapid change of magnetic moment immediately after the onset of dipolarization and (2) subsequent motion at nearly constant μ (i.e., nearly adiabatic transport). Grouping in gyration phase occurs during the first one of these sequences, whereas during the second one the phase-bunched particles gyrate at the local Larmor frequency". In our study, the nonadiabatic acceleration is caused by the magnetic field fluctuations near the ion gyrofrequencies, not the dipolarization itself. So the nonadiabatic behavior of ion including both the acceleration and the bunching effect in gyrophase would terminate only when the magnetic field fluctuations disappeared. This is consistent with what we observed in Fig.3.18.

To quantitatively examine the gyrophase variations, we plot the final gyrophase versus the initial energy for H^+ between 10 eV and 100 keV in Fig.3.19. The final phase is calculated by using Equation (17):

$$\tan\psi_{\text{final}} = \frac{\sin(\psi_0+2\pi\chi)+\frac{E_m \sin\pi\chi}{V_0 B(\chi^2-1)}\sin\pi\chi}{\cos(\psi_0+2\pi\chi)+\frac{E_m \sin\pi\chi}{V_0 B(\chi^2-1)}\cos\pi\chi} \qquad (17)$$

Equation (17) is a subsequent derivation based on equation (4) and (5) to estimate the final phase ψ_{final} of the particles with initial phase ψ_0 (*Delcourt et al.* 1997). The parameters put into the equations are the same as that used in Fig.3.16. The shaded area in Fig.3.18 represent the range of the final phases, which is decided not only by the initial energy but also by the initial gyration phase ψ_0 varying from 0° to 360°.

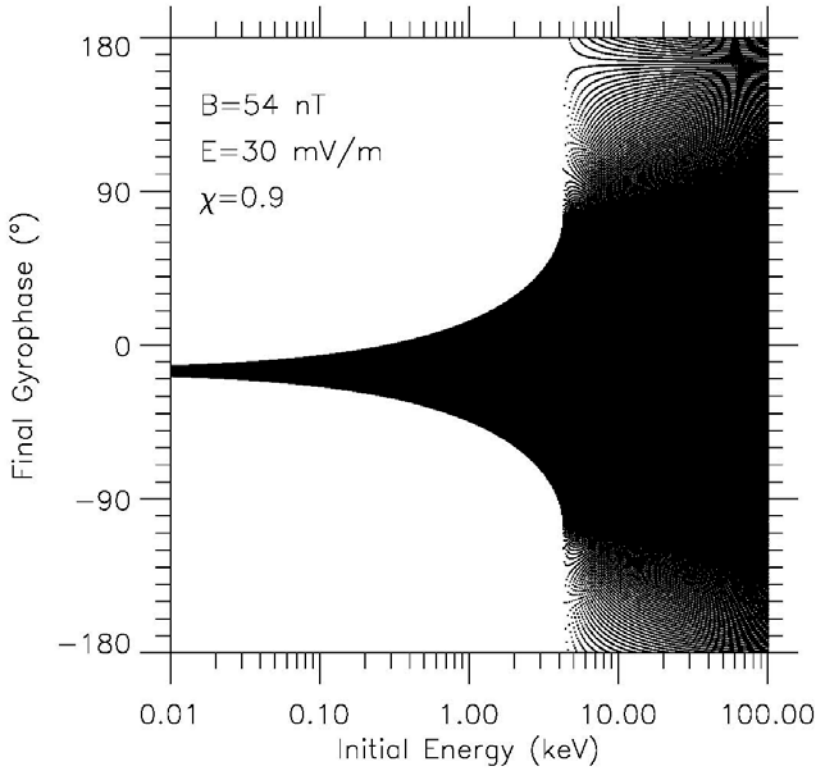

Fig.3.19 Final gyrophase versus the initial energy for H^+ between 10 eV and 100 keV. The shaded area represent the range of the final phase, which is decided not only by the initial energy but also by the initial gyration phase ψ_0 varying from 0° to 360°.

Fig.3.19 shows that the final phase of the particles is effectively bunched below 1 keV. From above 1 keV to 4 keV, the range of the final phases start to spread much wider, indicating that phase bunching effect becomes weaker with increasing energy. When the initial energy reaches over 4 keV, phase bunching effect almost totally disappears. These results illustrate that the ions accelerated from below 1 keV will have bunched gyrophase. Combined the fact the ions below 1 keV will be accelerated up to about 4 keV shown in Fig.3.16, it is easy to understand why the sporadic ions between 500 eV and 5 keV have bunched gyrophase.

3.6 Comparisons between the observed and the simulated spectrum

Moreover, in Fig.3.20 we plot the simulated energy flux spectrum of H^+ in the same interval of Fig.3.2a. Equation (16) was used again to calculate the variations of

the ion source distribution under the impulses of the magnetic and electric field observed in Fig.3.2 and Fig.3.5. The ion source distribution was given by the ion omni-directional fluxes (1D ion distribution) data of CIS/HIA at 16:40 UT. The magnetic and electric field data from 16:40 UT to 16:54 UT in Fig.3.2 and Fig.3.5 were employed in the calculations. To simplify the simulation, the parameter χ was fixed at 0.9 because the electric field disturbances near the gyrofrequency of H^+ accelerate ions most effectively as noted. The simulated spectrum was shown to agree well with the observations in Fig.3.2a, including the sporadic ions (indicated by the ellipsoid) as well as the apparent energy flux decrease/hole below 1 keV. The energy flux decrease between 1 and 20 keV was also observed in the simulated spectrum albeit not as pronounced as the observation due to the possibility that the decrease amount of the energy flux was fast refilled by the accelerated ions from the nearby energy (see Fig.3.16). And that the sudden appearance of 28-70 keV protons in Fig.3.5 was well reproduced by the simulation (see the energy flux increase above 30 keV in Fig.3.20 indicated by the arrow). These results clearly indicates that the missing ions (energy flux hole), the sporadic ions and 28-70 keV protons were all produced due to the nonadiabatic energy jump triggered by the magnetic field fluctuations.

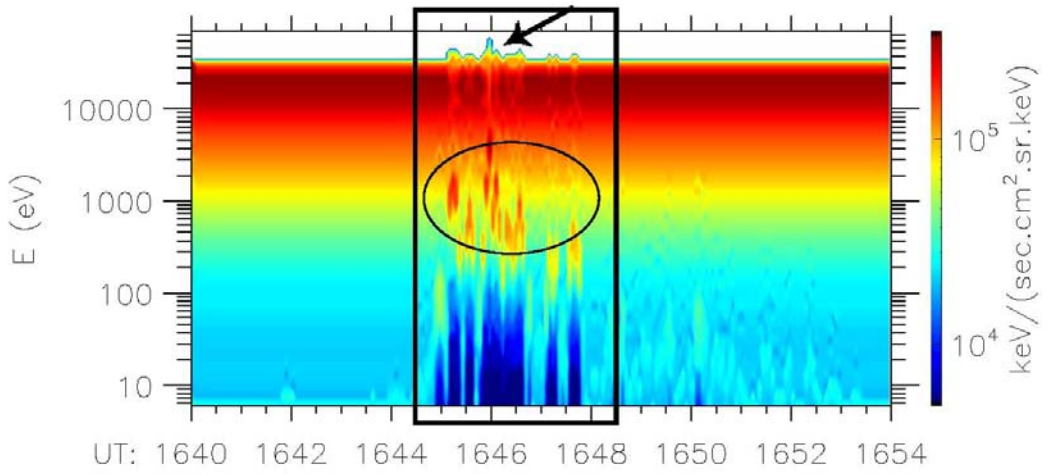

Fig.3.20 The simulated energy flux spectrum of H^+ in the same interval of Fig.3.2a.

We further display the simulated gyrophase variations with time in Fig.3.21. The color-coded spectrum gives the percent of energy over 360° gyropahse for ions between 500 eV and 5 keV (the sporadic ions). Equation (16) and (17) are used together to calculate the final gyrophase of the re-distributed ions after nonadiabatic acceleration. The other parameters put into the equations are the same as that used in Fig.3.20. The simulated spectrum shows that the dominant energy of ions are distinctly focused at a certain phase at 16:45 UT, 16:46 UT and 16:47 UT (indicated by the arrows), while the energy of ions are almost homogeneously distributed over 360° at 16:44 UT and 16:48 UT. These results well explain the gyrophase bunching patterns of the sporadic ions in Fig.3.18, and further confirm that they have experienced the nonadiabatic accelerations.

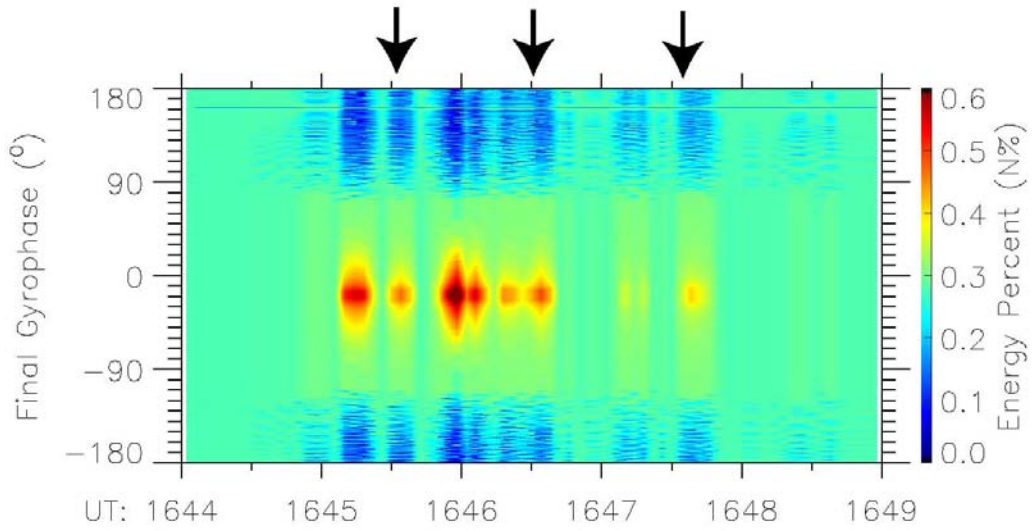

Fig.3.21 The simulated gyrophase variations with time. The color-coded spectrum gives the percent of energy over 360° gyropahse for ions between 500 eV and 5 keV (the sporadic ions).

In our calculations focusing on the electric field induced by the magnetic field fluctuations near the H^+ gyrofrequency, we found that the analytic results of the equations describing the nonadiabatic behavior of particles agree well with the energy flux variations and the gyrophase bunching patterns of ions we observed. These

analyses clearly indicate that the nonadiabatic acceleration caused by the magnetic field fluctuations near the ion gyrofrequency is reasonable.

3.7 Similar events observed by Cluster in the south of the plasma sheet

On 17 November 2009, Cluster observed similar energy flux variations of ions in the south of the plasma sheet, however, with some different characteristics.

Fig.3.22 shows the relative positions of the Cluster spacecraft in GSM coordinates at 01:12 UT on 17 November 2009. Panel (a) and (b) are the projections of positions in the X-Y and X-Z planes. The black, red, green and blue colors represent Cluster spacecraft SC1, SC2, SC3 and SC4 respectively.

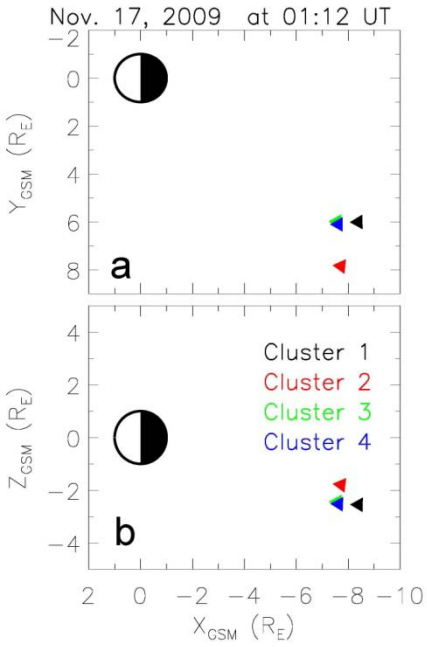

Fig.3.22 Cluster spacecraft positions projected to the X-Y and X-Z planes in GSM coordinates at 01:12 UT on 17 November 2009.

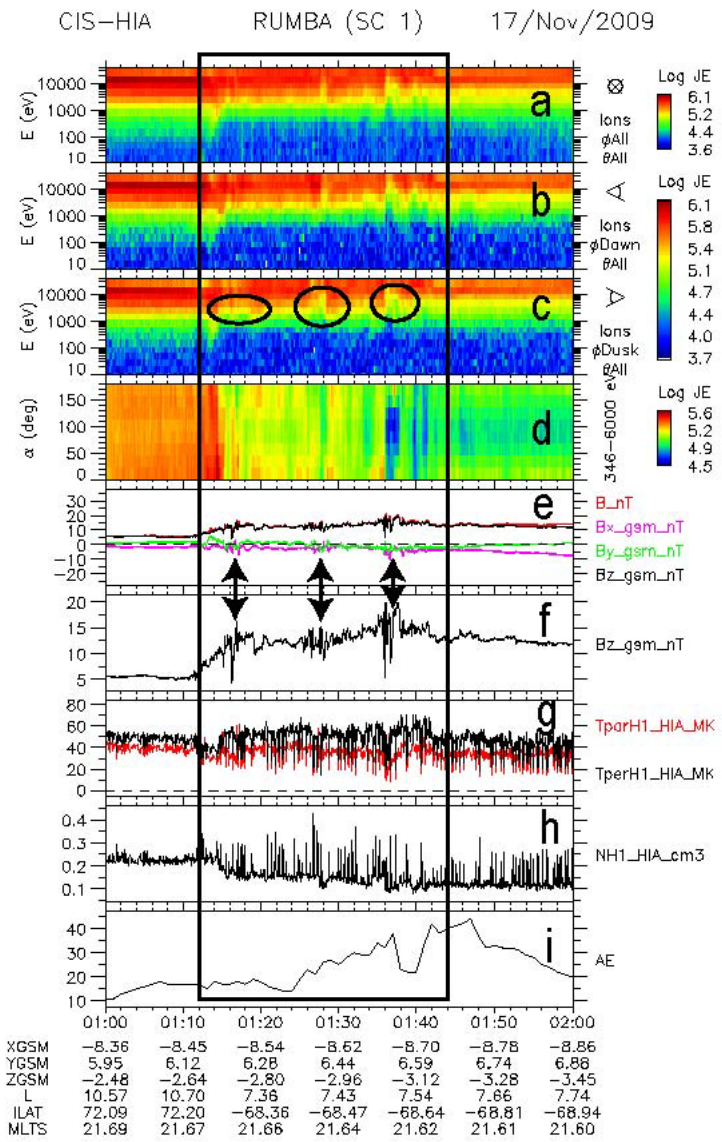

Fig.3.23 The energy-time spectrograms by HIA data of SC1 on 17 November 2009. Panel (a) is the omni-directional ion energy flux. Panels (b) and (c) are the profiles for particles arriving from the dawn (b) and from the dusk (c). Panel (d) is the pitch angle for the particles in the 346 eV-6 keV energy range. Panel (e) is the magnetic field magnitude and the three components in GSM coordinates. Panel (f) shows alone the B_z component. Panel (g) shows the parallel and perpendicular temperatures. Panel (h) is the ion number density. Panel (i) is the AE index.

Fig.3.23 shows the CIS-HIA observations on board SC1. This case is different from the first case (on 30 October 2006) in magnetospheric conditions and spatial positions of the spacecraft: it was observed during quiet magnetospheric conditions as

indicated by the AE index less than 50 nT (see Fig.3.23i, and the low AE had been lasted continually for hours); the spacecraft was located in the south-side of magnetotail plasma sheet (see the negative Z_{GSM} coordinates of the spacecraft in the bottom of Fig.3.23 and the negative B_x component in Fig.3.23e). Three energy flux holes were clearly identified from Fig.3.23c (indicated by the circles). But the sporadic ions showed up in the first case (on 30 October 2006), did not appear in this case (see in Fig.3.23b and Fig.3.23d). At 01:12 UT, B_z component started to increase clearly from 5 nT to 15 nT (see Fig.3.23f). The magnetic field also started to disturb since 01:12 UT, and the disturbance lasted for about half an hour. Intensive disturbances in the magnetic field appeared three times (indicated by the arrows in Fig.3.23e, Fig.3.23f), corresponding well to the three times energy flux holes in Fig.3.23c. In addition, the ion number density (see Fig.3.23h) was around 0.2, indicating SC1 was inside the plasma sheet.

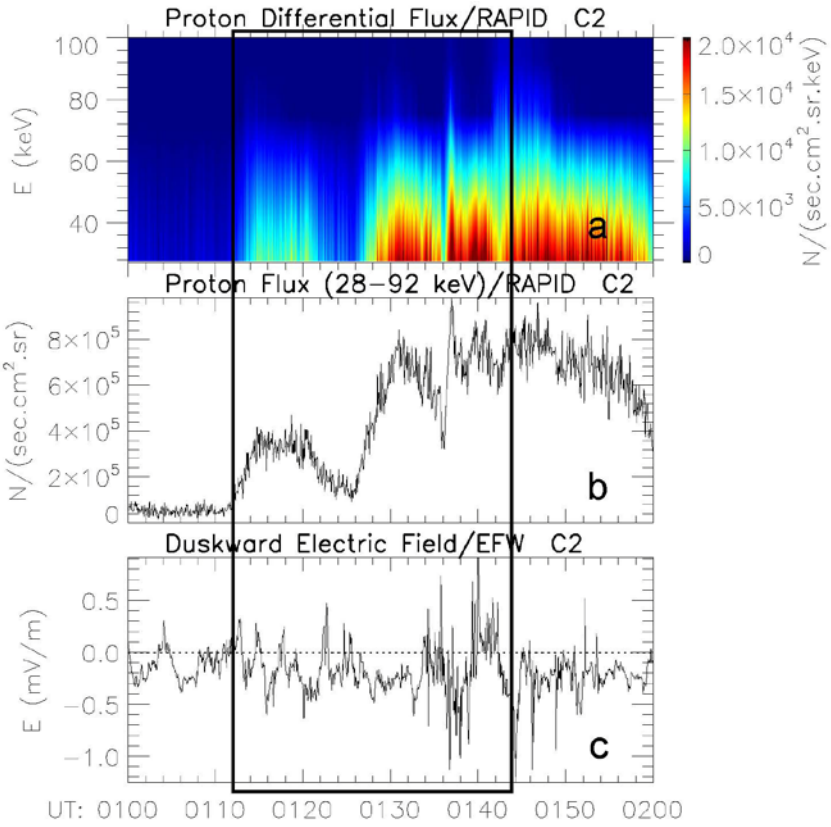

Fig.3.24 Proton differential flux (a) and 28-92 keV flux (b), and the duskward electric field (c) observed by RAPID and EFW instruments onboard SC2 on 17 November 2009.

RAPID on SC1 was deficient in data of proton differential flux during that period and only SC2 had these data. So we add SC2 measurements of proton differential flux (a) and 28-92 keV flux (b) by RAPID, and the duskward electric field by EFW in Fig.3.24. It is showed that proton differential flux obviously increased three times, and the duskward electric field was very weak (due to the quiet magnetospheric condition).

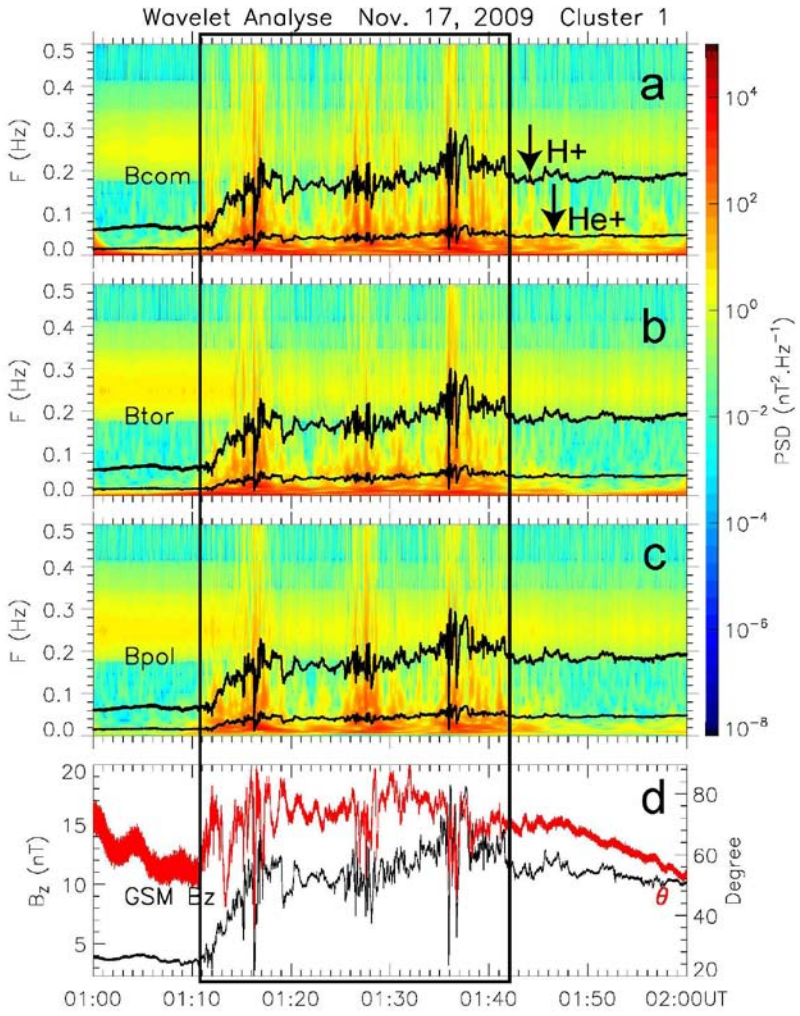

Fig.3.25 Wavelet analyses for magnetic field of SC1 in the field-aligned coordinate system on 17 November 2009 (a, b, c). The black dotted and dashed lines represent the gyrofrequencies of H^+ and He^+. The black and red lines in Panel (d) show the magnetic field B_z component and the magnetic elevation angle θ in GSM coordinates.

Fig.3.25 shows the wavelet analyses for the magnetic field of SC1 on 17 November 2009. The wave power was very large near the ion gyrofrequencies. However, the wave power was equally distributed in the three components, which is different from the first case (on 30 October 2006). It is evident the three times of wave package correlated well to the energy flux holes of ions in Fig.3.23c and the flux increase of ions in Fig.3.24.

The event observed in the south of the plasma sheet basically had the same characteristics as the one observed in the north of the plasma sheet, however different in 3 aspects:

1. The sporadic ions inside the energy flux holes did not show up as in the event on 30 October 2006. This agrees with the simulation results for the southern hemisphere originating ions in *Delcourt et al.* [1990]. The particles from the south-side plasma sheet travel northward after acceleration (see trajectory 1 in Fig.2.2a, Fig.2.3a), thus lose the opportunities to be captured by the spacecraft below the equator.

2. The PSDs of the Magnetic field fluctuations was equally distributed in the three components, not dominant in the toroidal and poloidal components as the case observed in the north of the plasma sheet. This indicates there are different wave generation mechanisms in two sides of the plasma sheet (the speculation is given based on observations of plenty of events).

3. The event was observed during quiet magnetospheric conditions. This indicates the specific energy flux variations of ions are not directly related to the substorm, but the magnetic field fluctuations near the ion gyrofrequencies are the determinant factor. The reason why the specific energy flux structures always emerge during dipolarization is that abundant of wave instabilities were excited at that time.

3.8 Similar events observed by Cluster and Double Star TC-1 in the ring current

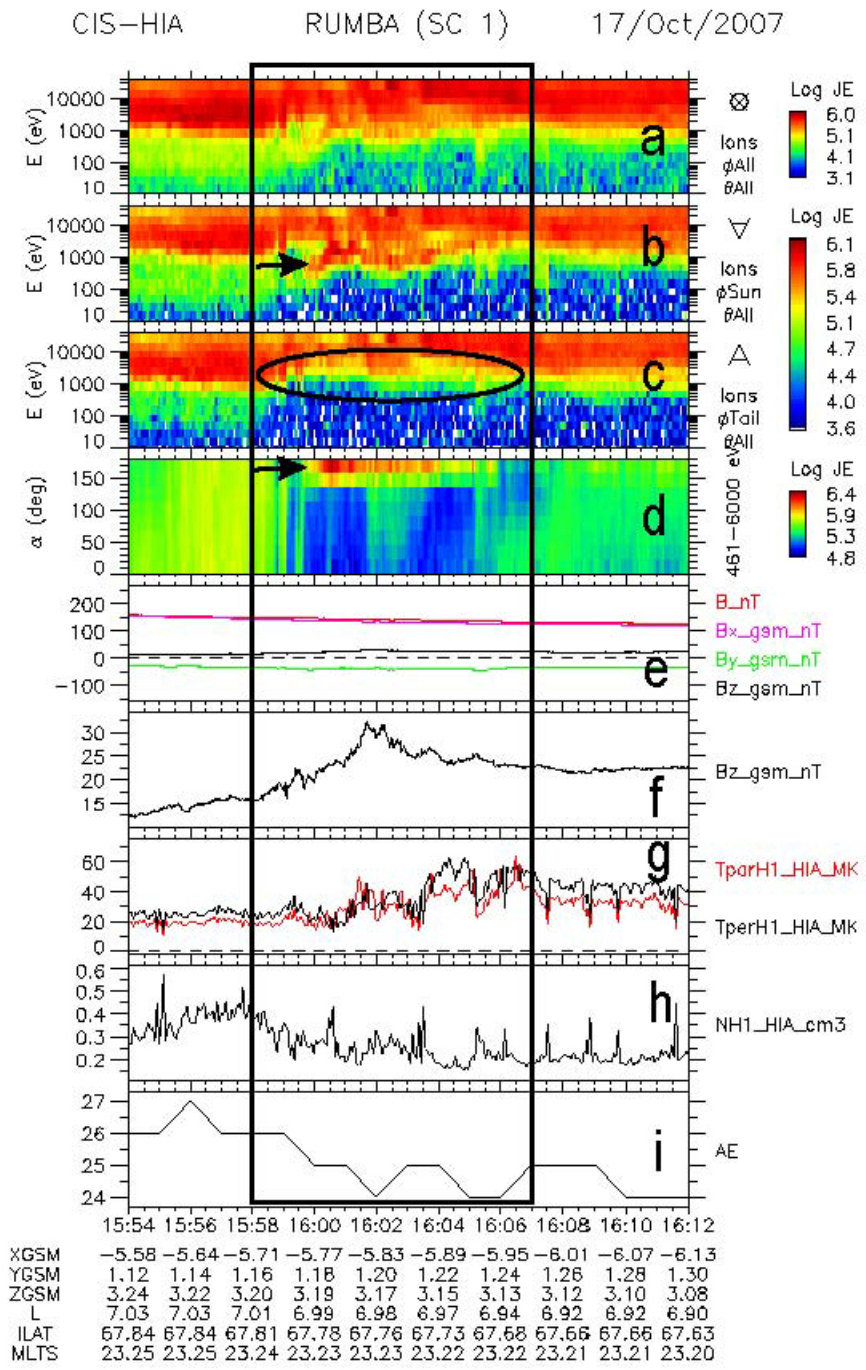

Fig.3.26 The energy-time spectrograms by HIA data of SC1 on 17 October 2007. Panel (a) is the omni-directional ion energy flux. Panels (b) and (c) are the profiles for particles arriving from the Sun (b) and from the tail (c). Panel (d) is the pitch angle for the particles in the 461 eV-6 keV energy range. Panel (e) is the magnetic field magnitude and the three components in GSM coordinates. Panel (f) shows alone the B_z component. Panel (g) shows the parallel and perpendicular temperatures. Panel (h) is the ion number density. Panel (i) is the AE index.

Besides in the plasma sheet, several similar cases are observed in regions even more close to the Earth, i.e. in the ring current. We select two events to present in this section, which are recorded by Cluster and Double Star TC-1 respectively.

Fig.3.26 shows the observation recorded by SC1 during 15:54-16:12UT on 17 October, 2007. The AE index is lower than 30 nT (see Panel (i)), indicating the quiet magnetospheric conditions. Panel (f) shows the clear magnetic field B_z increase. The characteristic energy flux decrease of ions can be seen in the energy-time spectrum in Panel (c); the sporadic ions can be seen in panel (b), which have 180° pitch angles (see in Panel (d)).

Unfortunately, RAPID aboard SC1 was also deficient in data of proton flux during that period for this event. Fig.3.27 shows the wavelet analysis for the magnetic field recorded by SC1. EMIC waves with frequency right below the He^+ gyrofrequency was observed to rise up intensively during the magnetospheric dipolarization phase.

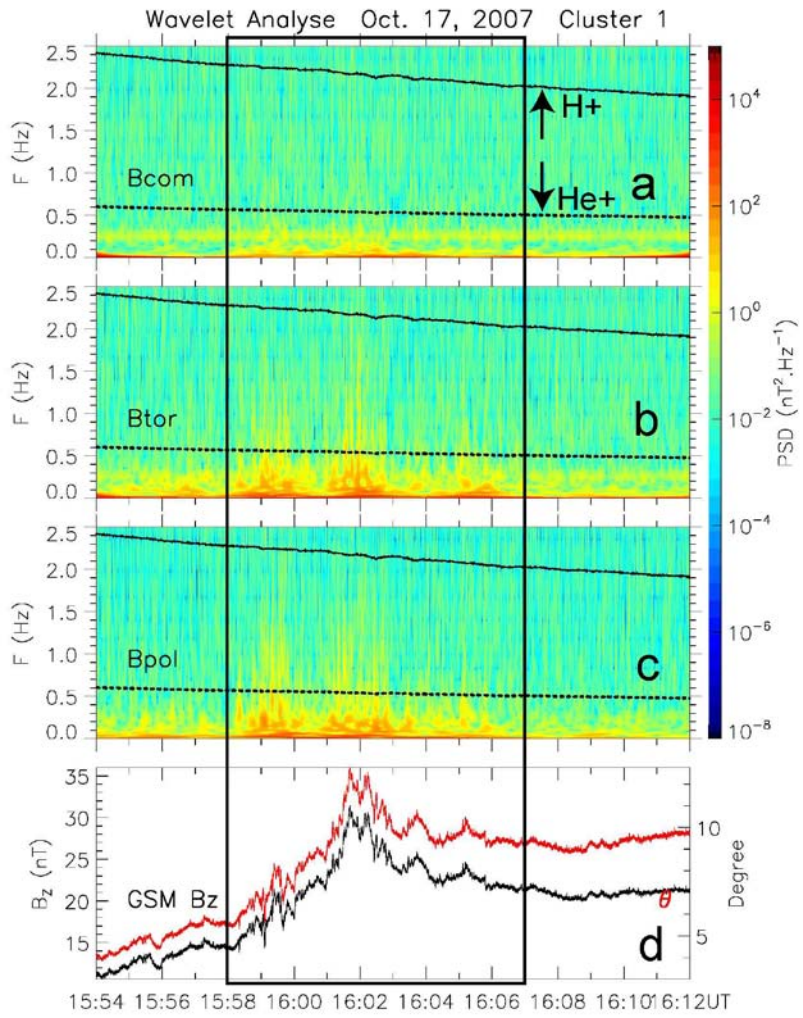

Fig.3.27 Wavelet analyses for magnetic field of SC1 in the field-aligned coordinate system on 17 October 2007 (a, b, c). The black dotted and dashed lines represent the gyrofrequencies of H^+ and He^+. The black and red lines in Panel (d) show the magnetic field B_z component and the magnetic elevation angle θ in GSM coordinates.

Fig.3.28 shows another event observed by Double Star TC-1 during 06:46-06:58 UT on 23 September, 2005. In Panel (f), we can see the B_z component of the magnetic field have successive increase for three times. At the same time, in the energy-time spectrogram (see in Panel (a) and (c)), there are also three times of energy flux decrease of ions, and sporadic ions (see Panel (b)) whose pitch angles exhibit clear tendency to focus on 130°-180° (see Panel (d)).

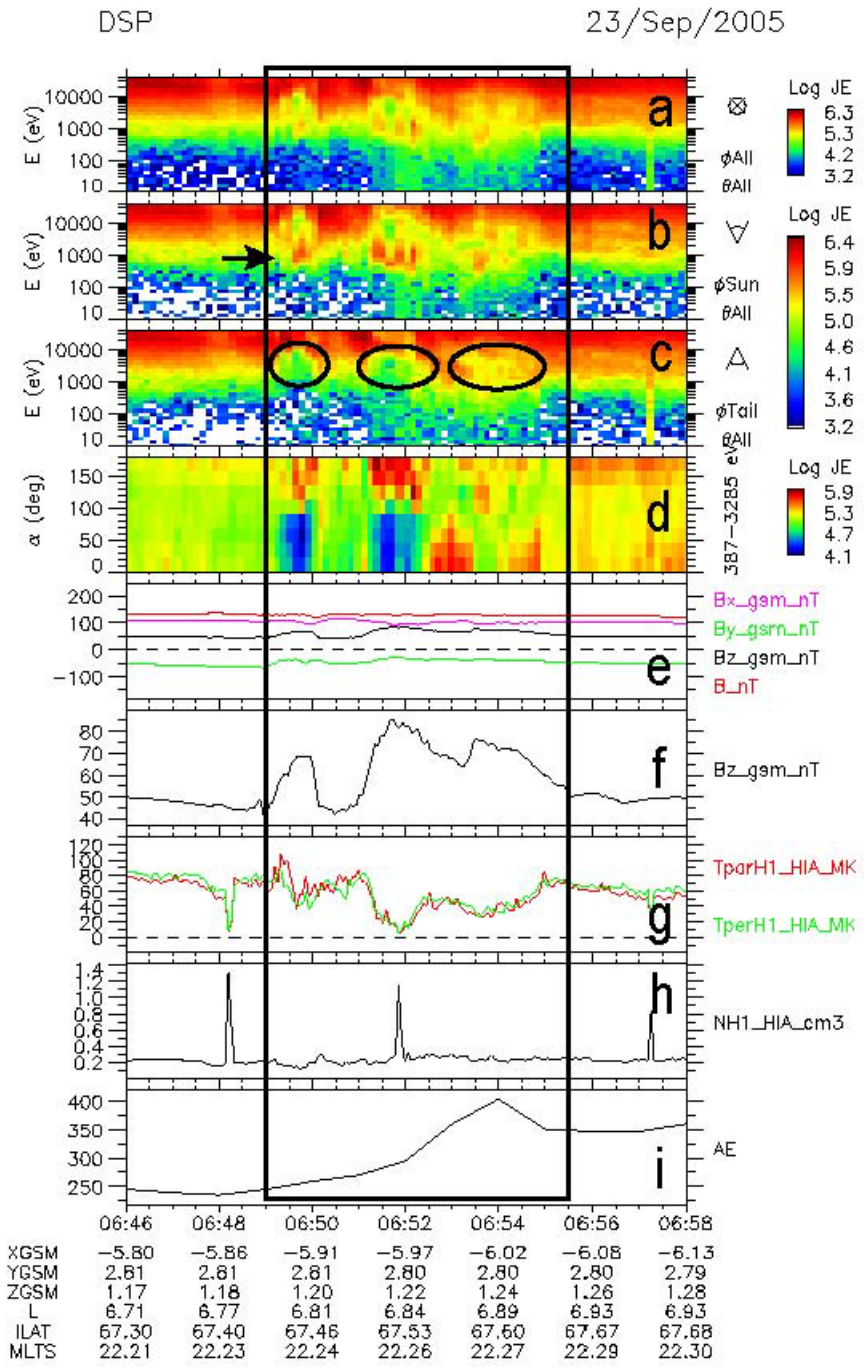

Fig.3.28 The energy-time spectrograms by HIA data of Double Star TC-1 on 23 September 2005. Panel (a) is the omni-directional ion energy flux. Panels (b) and (c) are the profiles for particles arriving from the Sun (b) and from the tail (c). Panel (d) is the pitch angle for the particles in the 387-3285 eV energy range. Panel (e) is the magnetic field magnitude and the three components in GSM coordinates. Panel (f) shows alone the B_z component. Panel (g) shows the parallel and perpendicular temperatures. Panel (h) is the ion number density. Panel (i) is the AE index.

Due to the lack of RAPID instrument aboard Double Star TC-1, the variations of the high energy ions flux (>20 keV) cannot be examined for this event. Moreover, by the lack of the high resolution magnetic field data (higher than the spin resolution), the magnetic field fluctuations near the ion gyrofrequencies cannot be investigated either.

In conclusion, these supplementary events presented above show consistent characteristics as the event (30 October, 2006) we have scrutinized. This indicates that nonadiabatic acceleration of ions by the magnetic field fluctuations near ion gyrofrequencies is not an isolated and coincidental phenomenon, but rather widely existing in the plasma sheet and ring current, especially during dipolarization phase.

3.9 Conclusions

This study presents a temporal energy spectrum structure of ions observed by Cluster and Double Star TC-1 in the plasma sheet, whose characteristics can be summarized as follows: (1) Abrupt energy flux decrease (referred to as 'energy flux holes') over 10 eV-20 keV. (2) Inside the energy flux holes scattered some ions with bunched gyrophases and pitch angles over 130°-180° (referred to as 'sporadic ions'). (3) Simultaneously the proton differential flux in higher energy (28-70 keV) had a sudden increase.

The temporal ion energy flux variations was found to occur on the condition that the impulsive electric field (with the magnitude of $V_E/V_0 \approx 4.0$ (V_E=E/B, V_0 is adopted as the velocity of H^+ in 0.1keV)) and magnetic field fluctuations near the H^+ gyrofrequency perturb the gyromotion of particles. Application of this condition to the equation describing the nonadiabatic behavior of particles presented in [*Delcourt et al.* 1997] shows that the analytic and simulative results agree well with the observations. These analyses strongly support the idea that the ions can be nonadiabatically accelerated by the electric field induced by the magnetic field fluctuations near the ion gyrofrequencies [*Ono et al.*, 2009; *Nosé et al.*, 2012]. Previous studies show that the

nonadiabatic acceleration of ions occurs mainly in mid-tail plasma sheet (H^+, at L=11) when the dipolarization timescale is comparable to the ion gyroperiod [*Delcourt et al.*, 1994]. Our results demonstrate that it can also occur in a region much closer to the Earth (H^+, at L=8) when the magnetic field fluctuations have a frequency close to the ion gyrofrequency. The newly reported ion energy flux hole structure can be used as a proxy to identify this dynamic process.

Chapter 4 Global frequency distributions of pulsations driven by sharp decrease of solar wind dynamic pressure

4.1 Introduction

4.1.1 Interplanetary shocks and the associated geomagnetic pulsations

InterPlanetary Shocks (IPS) are compressional MagnetoHydroDynamic (MHD) discontinuities propagating through the solar wind. They are mainly driven by two sources, Coronal Mass Ejections and Corotating Interaction Regions. They can be classified into four types according to the associated changes in the solar wind plasma and interplanetary magnetic field: fast forward, fast reverse, slow forward, and slow reverse shocks (see Fig.4.1). Interplanetary shocks propagate in the solar wind at almost constant speed. When arriving at the Earth's orbit, they interact with the Earth's magnetosphere [*Andréeová*, 2008].

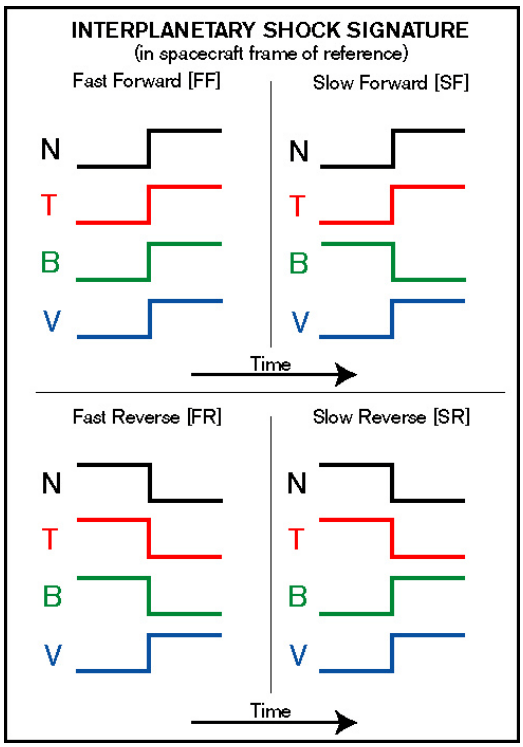

Fig.4.1 A classification of the interplanetary shocks. *N*, *T*, *B*, *V* stand for solar wind density, temperature, magnetic field magnitude, and velocity respectively.

A solar wind dynamic pressure (P_{sw}) impulse is always associated with the interplanetary shocks. When the P_{sw} impulse hits the Earth, the magnetosphere will undergo a sudden compression due to the sharp increase of solar wind dynamic pressure at the leading edge of impulse and a sudden expansion due to the sharp decrease of solar wind dynamic pressure at the trailing edge of impulse. A broad band fast mode wave which is launched by magnetopause oscillations will propagate toward the Earth and will pass through the magnetosphere [*Wilken et al.*, 1982, *Araki*, 1994, *Lysak et al.*, 1994; *Samsonov et al.*, 2006; *Andreeova et al.*, 2008]. This fast mode compression wave can be converted into Alfvén wave at points where there is a sufficient gradient in the magnetospheric plasma and magnetic field, result into a two vortex structure of currents in the ionosphere [*Araki*, 1994; *Lysak and Lee*, 1992].

The sudden magnetospheric compression easily causes global disturbance in the magnetic and electrical fields, plasma motions and energetic particle distributions in the magnetosphere [*Erlandson et al.*, 1991; *Mishin et al.*, 1993; *Taylor et al.*, 1997; *Kim et al.*, 2002; *Wing et al.*, 2002; *Li et al.*, 2003; *Zesta and Sibeck*, 2004; *Lee and Lyons.*, 2004; *Borodkova et al.*, 2008; *CoCo et al.*, 2008; *Zong et al.*, 2009; *Dandouras et al.*, 2009, *Wang et al.*, 2009]. Sudden changes in the geomagnetic field are well known as a Sudden Commencement (SC) or a Sudden Impulse (SI) depending on whether or not a magnetic storm follows. SCs and SIs have been examined in a large number of studies and result from the arrival of a compressional wave launched by an inward motion of the dayside magnetopause and propagating antisunward in the magnetosphere [*Keika*, 2008]. Contrary to the sharp increase of P_{sw}, the sharp decrease of P_{sw} can cause a sudden expansion of magnetosphere, which can also produce global disturbance in the magnetosphere, but often with opposite polarity.

Previous studies show that the sharp variations of P_{sw} can excite a broad spectrum geomagnetic pulsations (P_{sc}) [*Chen and Hasegawa*, 1974; *Farrugia et al.*, 1989; *Korotova and Sibeck*, 1994; *Parkhomov et al.*, 1998; *Sato et al.*, 2001; *Takeuchi et al.*, 2002; *Kepko et al.*, 2002; *Zolotukhina et al.*, 2007; *Zhang et al.*, 2010].

Recently, the pulsations driven by sharp decrease of solar wind dynamical pressure begin to attract people's attention. *Parkhomov et al.* [1998] once reported a long-period geomagnetic pulsation recorded at pre-night stations driven by sharp decrease of P_{sw}. They found two types of pulsations: one is latitude independent (T >400 s) which are forced pulsations associated with magnetopause oscillations, and the other is latitude-dependent (T <200 s) pulsations which come from field line resonance. *Sato et al.* [2001] found also that the geomagnetic pulsations around 1600 LT driven by the decrease of P_{sw} have characteristics of field-line resonance. *Zhang et al.* [2010], using magnetic field data of geosynchronous satellites GOES series, performed a statistical study about ULF waves at geosynchronous orbit excited by both positive and negative solar wind dynamic pressure pulses. Their results show that the ULF oscillations at geosynchronous orbit are in general stronger around local noon than those in the dawn and dusk flanks. However a case study of geomagnetic response to a decrease of P_{sw} on 1 April 1995 indicated that sometimes the geomagnetic response has only characteristics of SI^- (Negative Sudden Impulse) and lack of pulsation [*Takeuchi et al.*, 2002]. Therefore the generation mechanism and generation conditions of pulsations driven by sharp decrease of P_{sw} are still open questions. In addition, although previous studies have made important progress, the pulsations they studied are mainly limited in a narrow local time range. The global characteristics of pulsations driven by sharp decrease of P_{sw} are still unclear.

4.1.2 The theory of Field Line Resonance (FLR)

For several decades ULF pulsations have been observed using ground based magnetometer measurements. Pioneering work in interpreting these pulsations was first done by *Dungey* [1954], who found eigensolutions of a dipole magnetosphere assuming spatially constant plasma density. Later *Tamao* [1965] showed the possibility of excitation of resonant ULF waves within the magnetosphere. Experimental work by *Samson et al.* [1971] was crucial in determining amplitude and phase structures of the observed pulsations and finally led to the theoretical

approaches of *Chen and Hasegawa* [1974] and *Southwood* [1974], who developed a theory for Field Line Resonances (FLR) consistent with the observations.

Chen and Hasegawa [1974a] and *Southwood* [1974] have shown that when a monochromatic source with frequency ω_0 is present in the magnetosphere, magnetic pulsations can be excited at the frequency of the source, with the intensity maximum at the L-shell value of the resonant field line, where the Alfvén resonance condition is satisfied. The theory not only predicts that the wave amplitude peaks at the resonant field lines, but also the polarization of the waves. The polarization is linear near the peak, and the ellipticity gradually decreases away from the peak. Furthermore, the sense of polarization is opposite in the two sides of the resonant peak, as is shown in Fig.4.2.

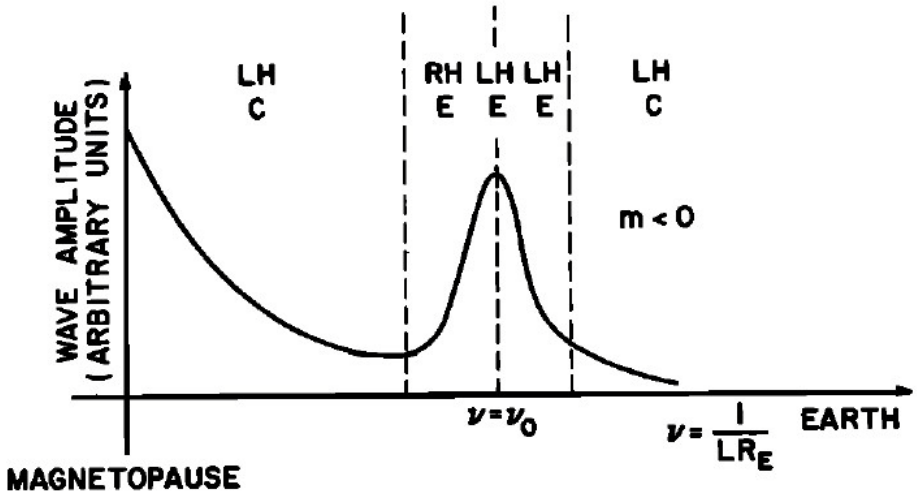

Fig.4.2 Sketch of the wave amplitude and sense of polarization versus radius in the equatorial plane for m < 0 (local morning). When it is projected along the field line to the ground, it can be viewed as a plot versus latitude. The C and E stand for Circular and Elliptical polarization, respectively. The results are opposite for m > 0 (local afternoon). The v_0 is the location of the resonant field line. The ellipticity is large (linear polarization) near the resonant field lines and decreases away (taken from Fig.4 of *Chen and Hasegawa*, 1974a).

Chen and Hasegawa [1974b] showed that since an inhomogeneous plasma does not provide a discrete set of eigenfrequencies (for incompressible modes), the only way in which a discrete mode can be excited is through a surface eigenmode if the source does not have a monochromatic frequency. These theories have successfully explained a majority of ground and spacecraft measurements in which the same frequency is observed at different latitudes for a given event with variations in the polarization and amplitude.

Hasegawa et al. [1983] made a development for the Field Line Resonances (FLR) theory and explained certain observations of magnetic pulsations where the frequency is found to vary continuously as a function of latitude for a given event. It is shown that in the presence of a broad band source, a local field line can oscillate at its Alfvén resonance frequency if the frequency band of the source covers the resonance frequency. The result showed that it is theoretically possible to observe an L-dependence in magnetic pulsations during a given event.

4.1.3 The theory of cavity resonance mode

Although Field Line Resonance (FLR) model explained well the toroidal resonances commonly observed by spacecraft in a wide range of L, Pc5 pulsations observed by ground based magnetometers and HF (High Frequency) radar data rarely exhibit this frequency spreading [e.g. *Hughes*, 1994]. A possible solution to this inconsistency was offered by *Kivelson et al.* [1984], who proposed that the magnetosphere may resonate with its own set of eigenfrequencies (i.e. the cavity/waveguide mode model). *Kivelson and Southwood* [1985, 1986] further developed this idea, postulating that a frequency-dependent turning point and the magnetopause form the inner and outer boundaries of this cavity, respectively. The model predicts energy transport from the magnetopause to the turning point for waves that propagate with the cavity eigenfrequencies (which are determined by magnetospheric boundary conditions). The theoretical models for the cavity mode

include a simple box geometry with perfectly reflecting boundaries [*Kivelson and Southwood*, 1986], a rectangular wave guide [*Samson et al.*, 1992], a cylindrical magnetosphere [*Allan et al.*, 1986] or a dipole magnetosphere [*Lee and Lysak*, 1989]. The differences in the magnetospheric geometry lead to different mode structures.

A multiharmonic cavity mode may be excited by a broad-band solar wind pressure wave. According to computer simulations, assuming perfectly reflecting boundaries [e.g. *Lee and Lysak*, 1991a], not only the cavity mode but also the multiharmonic toroidal resonances (Alfvén continuum) are excited by the impulsive source. According to numerical simulations [*Lee and Lysak*, 1991b], the compressional oscillations can couple to toroidal-mode standing Alfvén waves at the locations where the driver frequency matches the local toroidal-mode Alfven frequency.

Harrold and Samson [1992] and *Samson et al.* [1992] proposed that pulsations with discrete frequencies of 1.3, 1.9, 2.6, 3.4, and 4.2 mHz observed by high-latitude radar arise from a waveguide mode on the flankside of the magnetosphere. Usually pulsations are observed under a large range of solar wind conditions, a large set of magnetospheric configurations, a variety of boundary conditions applied to the waveguide and consequently, the eigenfrequencies may change accordingly [*Baker et al.*, 2003].

In addition, there is a class of Pc5 pulsations that are directly driven by periodic disturbances in the solar wind (e.g. [*Sarafopoulos*, 1995]). Since the disturbances in the solar wind can be a direct cause of low-frequency pulsations observed on the ground, the wave guide modes are not necessarily the only cause of Pc5 pulsations. Not only does solar wind directly drive magnetospheric pulsations, but it should also control the frequency of magnetospheric resonances. As for the waveguide mode, *Sarafopoulos* [2005] note that the distance of the outer boundary will become smaller for a larger solar wind dynamic pressure or a larger southward component of the interplanetary magnetic field.

4.1.4 Twin-vortex current system in the ionosphere

The geomagnetic Sudden Commencement (SC) is a transient magnetosphere and ground phenomenon. It has a clear onset and can be detected almost everywhere within the magnetosphere and almost simultaneously on the earth. The source of SCs is identified as the interplanetary shocks and the solar wind dynamic pressure changes.

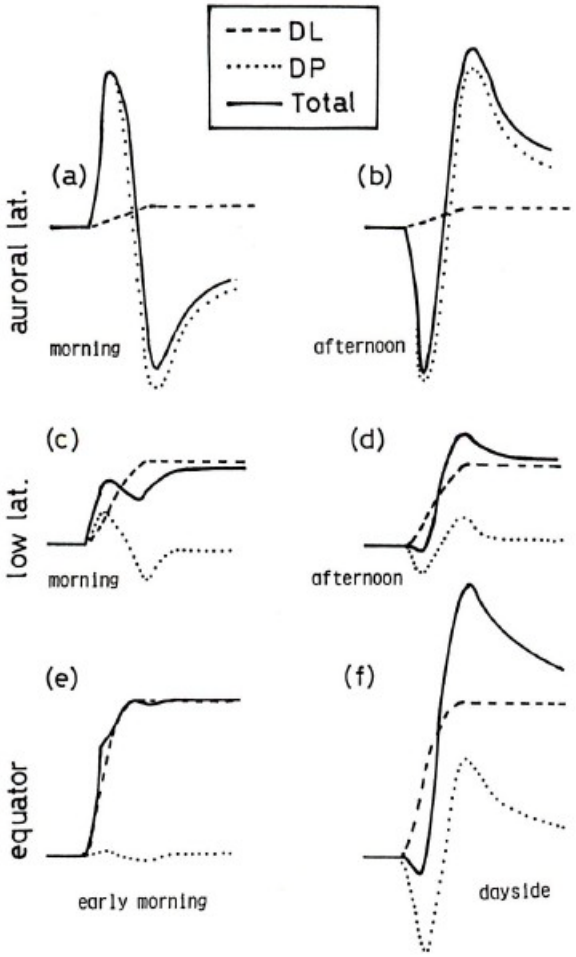

Fig.4.3 Decomposition of the SC disturbance field into DP and DL sub fields (details see in the text) (taken from Fig.11 of [*Araki*, 1994]).

A physical model to explain the global structures of the geomagnetic Sudden Commencement (SC) was proposed by *Araki* [1994]. In this model, the disturbance field of the SC is decomposed into two sub-fields DL and DP (see Fig.4.3). The DL field, which shows a monotonic increase of the H component, is produced by electric

currents flowing on the magnetopause and a propagating compressional wave front. The DP field consists of two successive pulses, the PI (Preliminary Impulse) and the MI (Main Impulse), with opposite senses, both of which are produced by twin vortex type ionospheric currents.

The PI (Preliminary Impulse) is due to the Field Aligned Currents (FACs) associated with the Alfvén wave. The perturbation of the current in the magnetopause launches a fast mode compressional wave that propagates radially towards the ionosphere. Since the plasma in the magnetosphere is inhomogeneous, regions of sharp density gradients allow for the fast mode to couple to an Alfvén mode which propagates to the ionosphere along the magnetic field lines. In the northern hemisphere, the FACs flow into the ionosphere on the dusk side and out of the ionosphere on the dawn side. This creates a twin vortex current system in the ionosphere (see in Fig.4.4), with a clockwise Hall current vortex on the afternoon side and an anti-clockwise vortex on the morning side [*Vontrat-Reberac, et al.*, 2002].

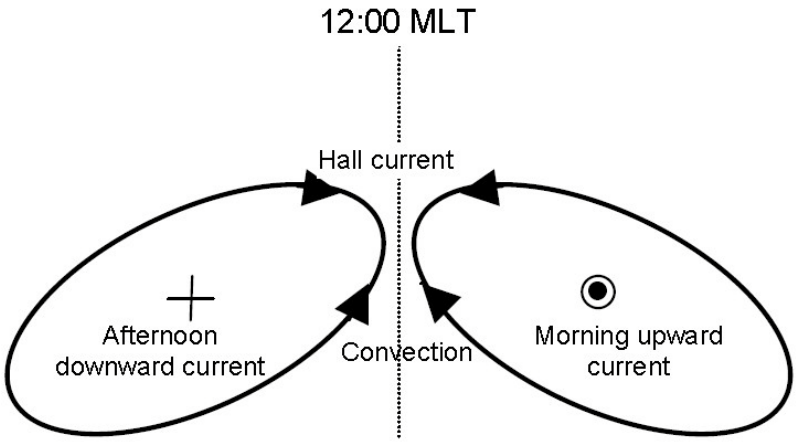

Fig.4.4 Schematics of the convection-current system in the Northern Hemisphere ionosphere during the Preliminary Impulse (*PI*). The system is reversed during the Main Impulse (MI) (taken from Fig.1 of [*Vontrat-Reberac, et al.*, 2002]).

After the compressional front has passed the Earth, the magnetospheric convection readjusts to the new compressed state. The FACs associated with this adjustment (referred as the Main Impulse, or MI) flow out of the ionosphere on the

dusk side and into the ionosphere on the dawn side. This creates an ionospheric current vortex system that has an inverse sense of rotation compared with the PI.

4.2 Observations

Stations(codes)	Geographic LAT	LONG	Geomagnetic LAT	Time Resolution
Faroes(FAR)	N62.1	W7.0	N65.3	1s
Hartland(HAD)	N51.0	W4.5	N54.5	1s
Crooktree(CRK)	N57.1	W2.64	N59.8	1s
Nagycenk (NCK)	N47.6	E16.7	N46.9	1s
Kilpisjarvi(KIL)	N69.0	E20.8	N66.1	1s
Nurmijarvi(NUR)	N60.5	E24.7	N57.7	1s
Oulujarvi(OUJ)	N64.5	E27.2	N61.0	1s
BOROK(BOR)	N58.03	E38.33	N53.0	1s
Zhigansk (ZGN)	N66.8	E123.4	N61.1	1s
Tixie Bay (TIX)	N71.6	E129.0	N 65.7	1s
Yakutsk(YAK)	N62.0	E130.0	N56.4	1s
Zyryanka(ZYK)	N65.8	E150.8	N59.6	1s
Victoria (VIC)	N48.5	E236.6	N54.26	5s
Ottawa(OTT)	N45.4	E284.4	N56.73	5s
St.Johns(STJ)	N47.6	E307.5	N58.34	5s

Table 1 List of 24 ground stations

In this chapter, using the high resolution geomagnetic field data, we study the global characteristics of power spectral densities, resonant frequencies and polarizations of geomagnetic pulsations at auroral and subauroral latitudes excited by a sharp decrease of P_{sw} on 24 August 2005. The ground-based magnetic data come from 15 stations which cover most local time range. The geographic and geomagnetic coordinates of these 15 stations are given in Table 1. Throughout the study, the GSM coordinates are adopted.

4.2.1 Observations by spacecraft

On 24 August 2005, an impulse of solar wind dynamic pressure hits the Earth, which is characterized by a sharp increase of P_{sw} in the leading edge and a sharp decrease of P_{sw} in the trailing edge. During this event, Geotail, which is located at (13.0, 23.2, 11.2) R_E, is in the solar wind and is therefore able to provide solar wind parameters. TC-1 is in the dawnside magnetosphere and located at (-1.5, 5.3, 4.2) R_E. TC-2 is in the night side magnetosphere and located at (-5.2, -1.2, -1.8) R_E. The locations of Geotail, TC1 and TC2 are displayed in Fig.4.5. The magnetic shell parameter L values of TC-1 and TC-2 are 11.9 and 7.3 respectively, which corresponds to the invariant latitudes 73.1° and 68.3°. Therefore the magnetic data recorded by FGM/TC-1 and FGM/TC-2 can be used to show the processes of compression and expansion of the magnetosphere.

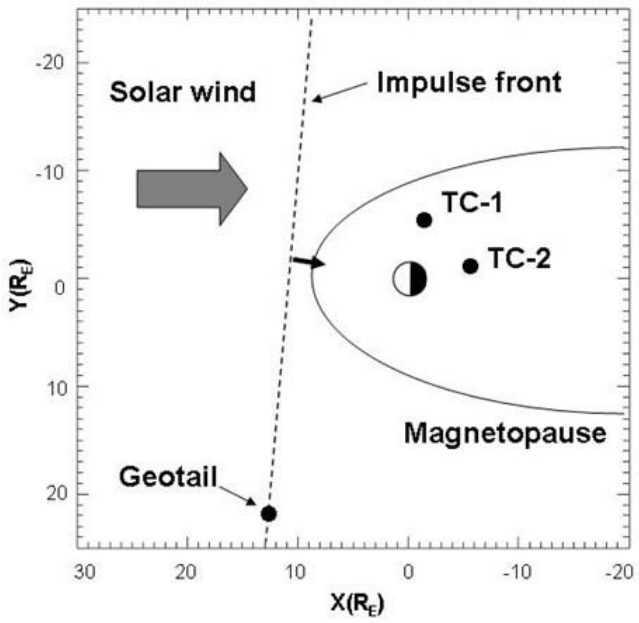

Fig.4.5 Schematic of solar wind dynamic pressure impulse front, and the positions of three satellites (Geotail, TC-1 and TC-2) in the X-Y GSM plane.

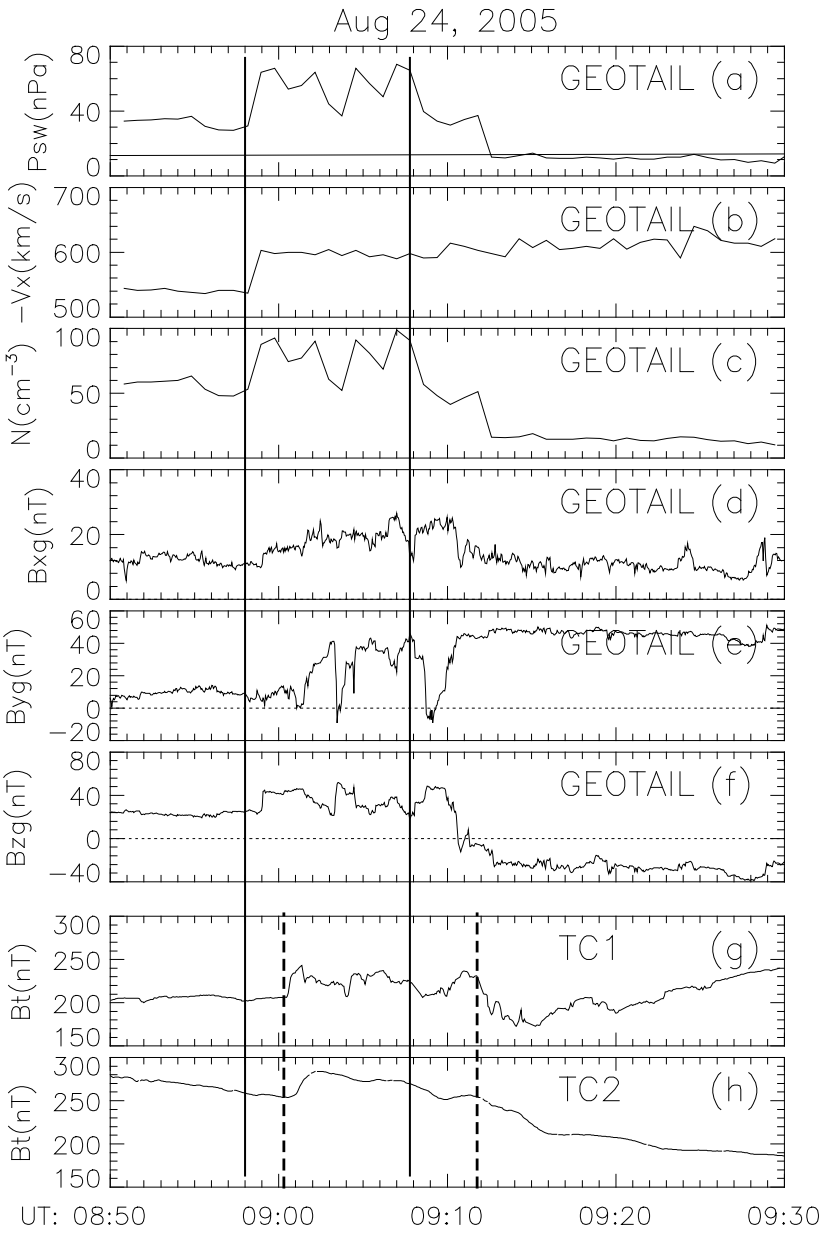

Fig.4.6 Solar wind parameters recorded by Geotail (P_{sw}, $-V_x$, N_{sw}, B_{xg}, B_{yg}, B_{zg}) and magnetic field in the inner magnetosphere recorded by TC1 and TC2. The two vertical solid lines denote the onsets of sharp increase and decrease of solar wind dynamic pressure respectively. The two dashed lines denote the onsets of increase and decrease of the magnetic field strengths recorded by TC1 respectively (throughout this study, the GSM coordinates are adopted).

Fig.4.6 shows the solar wind parameters recorded by Geotail (P_{sw}, $-V_x$, N_{sw}, B_{xg}, B_{yg}, B_{zg}) and magnetic field strength recorded by TC1 and TC2. The impulse front is characterized by sudden increases in ion density, flow velocity and dynamic pressure

of solar wind. Prior to the impulse, the solar wind dynamic pressure was stable at about 26 nPa. It started to rise at about 0858:00 UT and reached the peak of 65 nPa at 0859:30 UT. Then the solar wind dynamic pressure oscillated between 0859:50 UT and 0907:00 UT. Finally it underwent a sharp decrease, dropping from 62 nPa at 0907:50 UT to 14 nPa at 0912:30 UT.

Prior to the arrival of the impulse at 0858 UT, the IMF B_z and B_y are roughly 25 nT and 10 nT respectively. When the solar wind dynamic pressure starts to increase, the IMF B_z has a small jump at 0859UT. Soon after the solar wind dynamic pressure decreases at 0908UT, the IMF B_z encounters a rapid decrease at 0910 UT and drop to -24 nT at 0912:40 UT.

We calculate the subsolar standoff distance of magnetopause r_0 by using the stationary magnetopause models in *Shue et al.*, [1998] and *Lin et al.*, [2010]. The sudden increase of solar wind dynamical pressure at 0858:00 UT makes r_0 decrease from 6.94 R_E to 6.10 R_E. The sharp decrease of solar wind dynamical pressure at 0907:50 UT make r_0 increase from 6.11 R_E to 6.83 R_E.

In the dawnside magnetosphere, the magnetic field strength recorded by FGM/ TC1 starts to increase rapidly at 0900:26 UT, about 150s later than the onset of the sharp increase of solar wind dynamic pressure. In the nightside magnetosphere, the magnetic field strength recorded by FGM/TC2 starts to increase gradually at 0900:50 UT. The increases of magnetic field strength recoded at TC-1 and TC-2 denotes the compression of magnetosphere. The magnetic field strengths at TC-1 and TC-2 start to decrease 0911:40 UT, about 230s later than the onset of decrease of solar wind dynamic pressure. The decreases of magnetic field strength recoded at TC-1 and TC-2 are the consequences of the expansion of magnetosphere. It is reasonable that the delay time of the increase of magnetic field strength is smaller than that of decrease of magnetic field strength because the magnetosphere responds more quickly to the increase of P_{sw} than to the decrease of P_{sw}.

The detailed characteristics of this interplanetary shock and the responses of inner magnetosphere and plasma sheet have been presented by *Keika et al.* [2008] by using the data from Geotail, Cluster and DSP. Their calculations show that the normal direction is about (ϕ, θ) = (175°, 13°), where ϕ and θ are the longitude and latitude in GSM coordinates (see Fig.10 of [*Keika et al.* 2008]).

Wind satellite, which is located at (X_{GSM} = 231.2 R_E, Y_{GSM} = -98.6 R_E, Z_{GSM} = 3.2 R_E), also observed this solar wind dynamic pressure impulse at around 0825 UT. The estimated discontinuity normal is (ϕ, θ) = (173.6°, -1.3°), very close to that deduced from the data of Geotail [*Keika et al.* 2008]. Therefore the impulse front propagates anti-sunward and dusk ward. In this study we mainly focus on the pulsations at sub-auroral and auroral latitudes driven by sharp decrease of solar wind dynamic pressure.

4.2.2 Geomagnetic response at subauroral and auroral ħtitudes

Fig.4.7 shows the solar wind dynamic pressure P_{sw}, and the geomagnetic H and D components at thirteen subauroral and auroral latitude stations during the interval 0850 UT -0930 UT on 24 August 2005. The MLTs of stations are calculated at 0900 UT on 24 August 2005. A clear PPI (Preliminary Positive Impulse) can be seen at the morning stations FAR and HAD. At the noon stations BOR, OUJ, NUR and KIL, preliminary pulse is negatives (PRI). According to Araki's model [*Araki*, 1994] mentioned in the introduction, if a pressure discontinuity has a normal aligned with the Sun-Earth direction, two current systems are established at high latitudes: first, a pair of FACs comes with the magnetosonic front motion, one directed downward into the auroral zones in the afternoon, and the other directed upward out from the ionosphere in the morning; the closure currents in the high-latitude ionosphere form vortex structures, clockwise in the afternoon, and counterclockwise in the morning; The geomagnetic field below the morning and afternoon vortex current systems will display opposite signatures. In the present study, as seen in Fig.4.7, the boundary

between these two vortex current systems is located between 1015 MLT and 1203 MLT.

Geomagnetic pulsations driven by the sharp decrease of P_{sw} at 0908 UT can be clearly seen at almost all 13 stations. The periods of these geomagnetic pulsations are in the period range of Pi2, roughly between 100 and 200s.

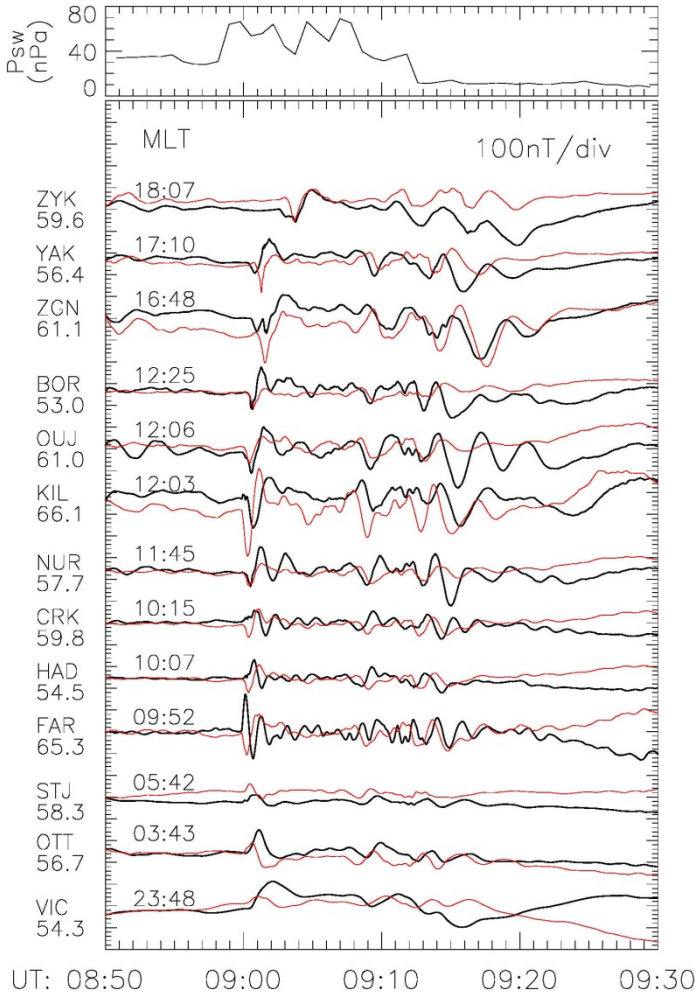

Fig.4.7 Solar wind dynamic pressure P_{sw}, H(black) and D(red) components at thirteen sub-auroral and auroral latitude stations during the interval 0850 UT-0930UT on 24 August 2005. The MLTs are calculated at 0900 UT on 24 August 2005.

4.2.3 Global characteristics of pulsations at subauroral and auroral latitudes

Fig.4.8 shows the Power Spectra Densities (PSD) of H and D components at sub-auroral and auroral latitudes at different magnetic local times. It can be seen that

the geomagnetic pulsations driven by the sharp decrease of solar wind dynamical have different frequency features at different magnetic local times.

For H component, the PSDs at stations ZYK, YAK, BOR. NUR and STJ have a peak which is located between 4.6 mHz and 5.8 mHz. The peak frequencies of PSD of H are 4.6 (ZYK), 5.4 (YAK), 5.8 (BOR), 5.8 (NUR) and 5.5 (STJ) mHz respectively. Therefore the peak frequency of PSD of H is largest around magnetic local noon and decreases when observation points move to dawn or dusk flanks. The PSDs of H at noon stations NUR and BOR have a second peak, which is located around 9.5 mHz. The two peaks overlap and form a wide frequency band ranging from 5.0 mHz to 10 mHz. The PSD of H at morning station CRK has no peak around 5.0 mHz but has a peak at 9.6 mHz. The PSDs of H at night stations OTT and VIC are very weak.

For the D component, the PSDs of D at all stations except ZYK have a peak located around 5.4 mHz. At ZYK, the PSD of D peaks at 4.8 mHz. At CRK, besides the peak at 5.4 mHz, there is a another larger peak which is located at 9.8 mHz. It is worth noting that at some stations the behaviors of PSD features of H and D are completely different. At NUR, the PSD of H has two peaks while the PSD of D has only one peak. In contrast, at CRK the PSD of H has only one peak while the PSD of D has two peaks.

The above observations indicate that the frequency features of the pulsations excited by sharp decrease of solar wind dynamical pressure are magnetic local time dependent. For all local times a pulsation at about 5.0 mHz can be observed. At dayside stations, the pulsations at about 9.8 mHz can be also observed.

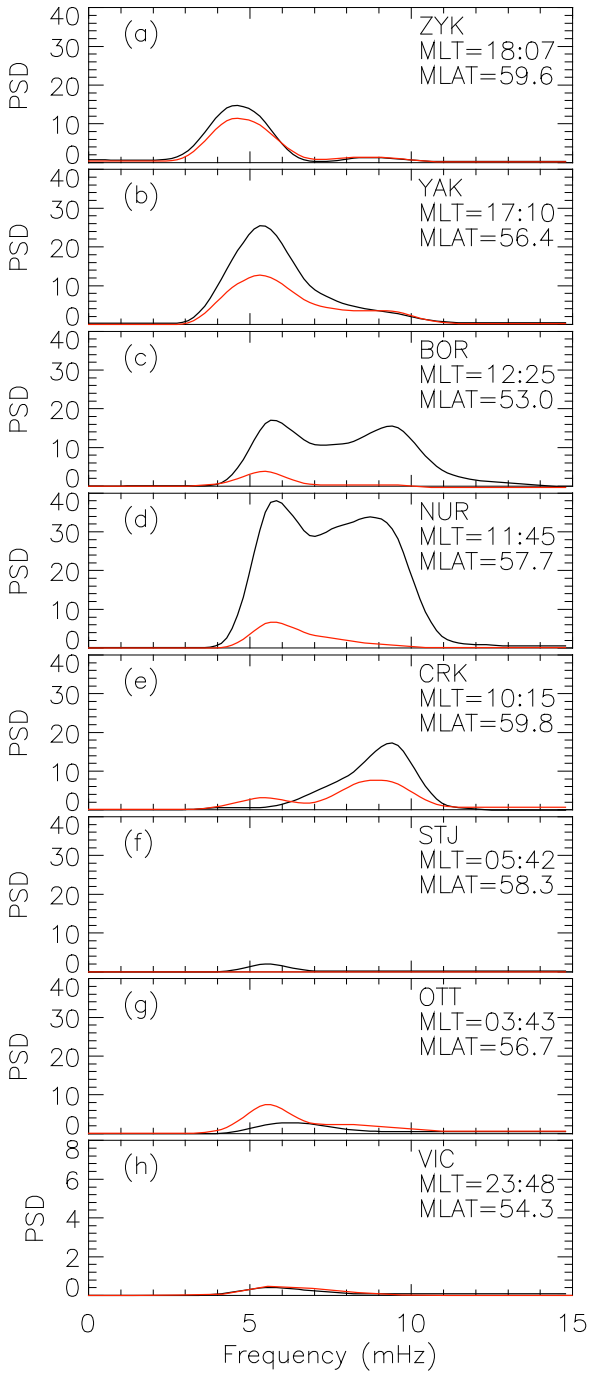

Fig.4.8 PSDs of H (black) and D (red) components at eight sub-auroral and auroral latitude stations during the interval 0912 UT-0924 UT on 24 August 2005.

4.2.4 The characteristics of pulsations at different latitudes around the same local times

In order to identify the generation mechanisms of these pulsations, we analyze the features of frequency and polarization of pulsations at approximately the same MLT but at different latitudes. Fig.4.9 shows the PSDs of H and D components at three dusk stations around 1700 MLT during the interval 0912-0924 UT on 24 August 2005. It can be seen that the PSDs of H and D components at three stations peak around 5.0 mHz. The PSD peak frequency increases slightly with decreasing magnetic latitude. For example, at TIX (MLAT=65.7°), the peak frequency is 4.3 mHz while at YAK (MLAT=56.4°), the peak frequency is 5.3 mHz. This result is in agreement with the resonance theory of eigen-oscillations of closed field lines in the magnetosphere mentioned in the introduction [*Southwood*, 1974; *Chen and Hasegawa*, 1974]. According to FLR theory, the resonant frequency is decided by the length of field line and the Alfven velocity on this line. The eigen frequency is inversely proportional to the length of field line. Therefore lower latitude means shorter length of field line and consequently higher resonant frequency. The PSD peak values of H and D components are largest at ZGN. It is worth noting that at high latitude stations TIX and ZGN, the PSD peak values s of D components are larger than those of H components. Since the ground D component corresponds to the radial component of poloidal mood in space, this result is consistent with the geosynchronous observations of ULF waves driven by solar wind dynamic pressure variations. *Zhang et al.* [2010] once found that at geosynchronous orbit, the poloidal wave amplitudes are stronger than the toroidal wave amplitudes both in positive and negative solar wind impulse events.

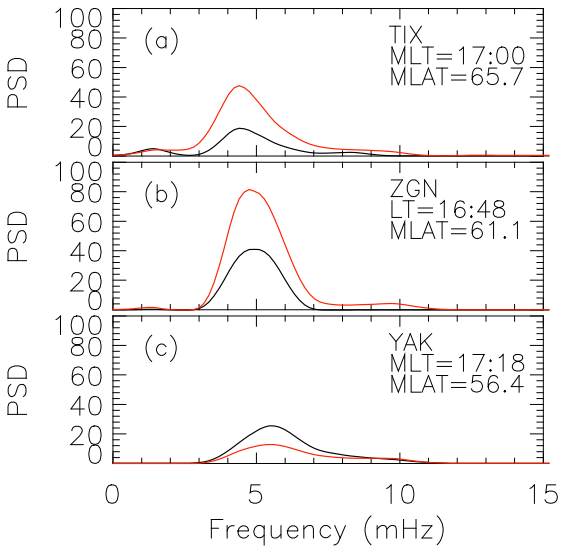

Fig.4.9 PSDs of H (black) and D (red) components at three dusk stations TIX, ZGN and YAK around 1700 MLT during the interval 0912 UT-0924 UT on 24 August 2005.

We further analyze the polarization features of pulsations at these three dusk stations. Fig.4.10 shows the hodograms of H and D components at three dusk stations around 1700 MLT during the interval 0913-0917 UT on 24 August 2005. The polarization of pulsation at YAK (MLAT = 56.4°) is roughly circularly polarized and clockwise. However at TIX (MLAT = 65.6°), the polarization is anticlockwise. At ZGN (MLAT = 61.1°), which is between TIX and YAK, the polarization of pulsation is unstable and oscillates between clockwise and anticlockwise polarizations. It is first clockwise, then anticlockwise and finally clockwise. This means that the station ZGN is located in a transition region from clockwise to anticlockwise polarizations. As seen in Fig.4.9, the PSDs of both H and D components at ZGN are larger than those at other two stations. The latitudinally narrow PSD peak accompanied by a significant latitudinal phase shift indicates that the source of pulsation is much likely field line resonance, and the footprint of the resonant L-shell is between YAK and TIX, and very close to ZGN.

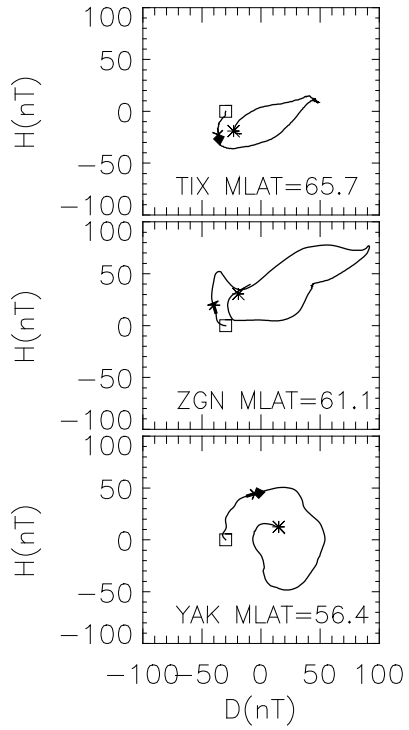

Fig.4.10 Hodograms of H and D components at three dusk stations TIX, ZGN and YAK around 1700 MLT during the interval 0913-0917 UT on 24 August 2005. The symbols square and asterisk denote beginning and ending of magnetic field line respectively.

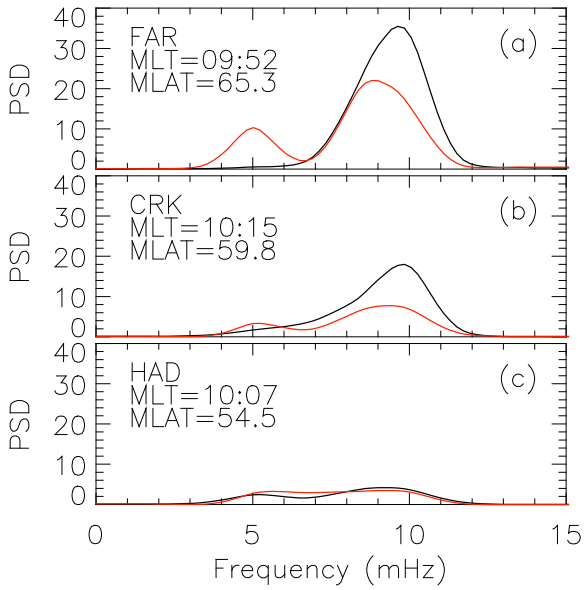

Fig.4.11 PSDs of H (black) and D (red) components at three morning stations FAR, CRK and HAD around 1000 MLT during the interval 0912 UT-0924 UT on 24 August 2005.

Fig.4.11 shows the PSDs of H and D components at three morning stations around 1000 MLT during the same interval as in Fig.4.9. The PSD at lower latitude station HAD is very small compared to those at other two higher latitude stations FAR and CRK. What is new is that the behavior of the PSDs of H and D are different. The PSDs of H components have only one peak whose frequency is about 9.8 mHz. The PSDs of D components have two peaks: one peak is located at 5 mHz and the other is located around 9.6 mHz. This means that besides pulsation at fundamental frequency 5 mHz, there exists a second harmonic wave.

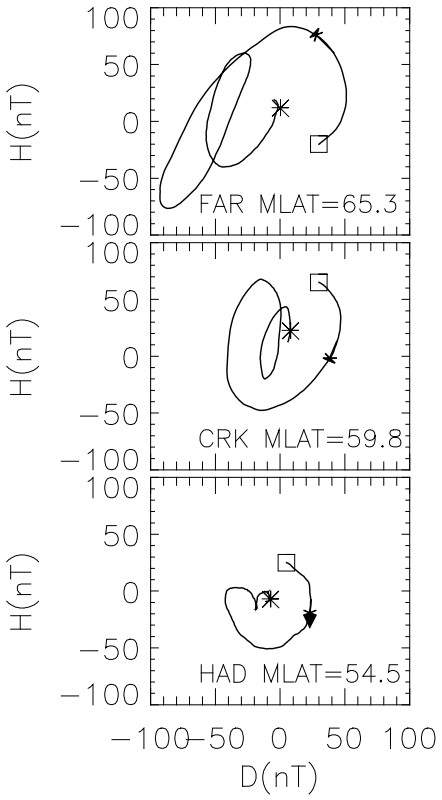

Fig.4.12 Hodograms of H and D components at three morning stations FAR, CRK and HAD around 1000 MLT during the interval 0913-0917 UT on 24 August 2005. The symbols square and asterisk denote beginning and ending of magnetic field line respectively.

Fig.4.12 shows the hodograms of H and D components at three morning stations around 1000 MLT during the interval 0913-0917 UT on 24 August 2005. The polarization of pulsation at CRK and HAD are clockwise while that at FAR is

anticlockwise. The reversal of polarizations between two stations is a feature of field line resonance. According to the theory of field line resonance, the footprint of resonant field line should be located between FAR and CRK.

Fig.4.13 shows the PSDs of H and D components at three noon stations around 1200 MLT during the same interval as in Fig.4.9. The PSDs of H at three noon stations all peak at two frequencies: 5.5 mHz and 9.4 mHz albeit the 9.4 mHz peak of PSD of H at KIL is not very clear. At two lower latitude stations NUR and NCK, the PSDs of H are much larger than those of D. However at higher latitude station KIL, the PSD of H is smaller than that of D. This result is similar to that in Fig.4.9. Fig.4.14 shows the hodograms of H and D components at three noon stations around 1200 MLT during the interval 0913-0917 UT on 24 August 2005. The polarizations of pulsation at NUR and NCK are clockwise while that at KIL is anticlockwise. This is once again an evidence of a reversal of the sense of polarizations.

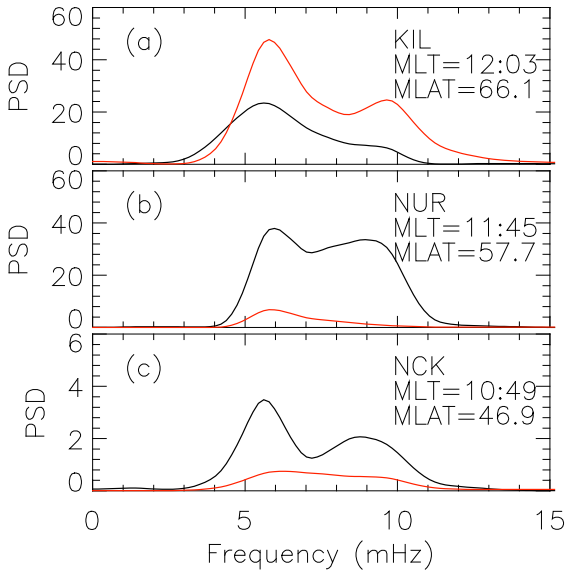

Fig.4.13 PSDs of H (black) and D (red) components at three magnetic local noon stations KIL, NUR and NCK around 1200 MLT during the interval 0912 UT-0924 UT on 24 August 2005.

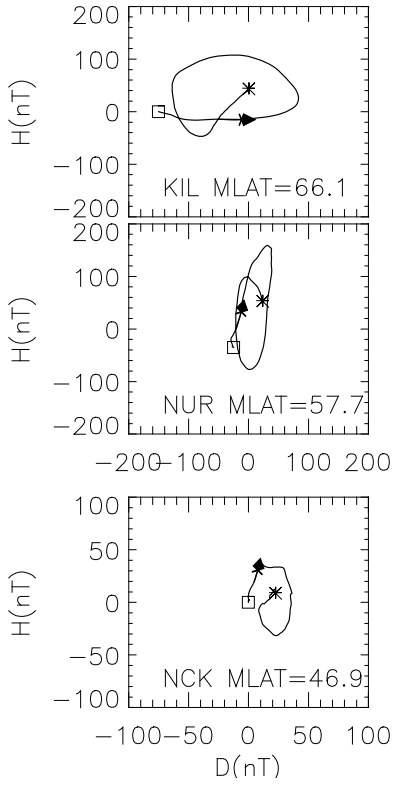

Fig.4.14 Hodograms of H and D components at three magnetic local noon stations KIL, NUR and NCK around 1200 MLT during the interval 0913-0917 UT on 24 August 2005. The symbols square and asterisk denote beginning and ending of magnetic field line respectively.

4.2.5 Comparison between the pulsations driven by sharp increase and sharp decrease of P_{sw}

Not like the sharp decrease of solar wind dynamical pressure, the sharp increase of solar wind dynamical pressure at 0858 UT excite pulsations with regular waveforms only at morning and pre-noon stations NUR, CRK, HAD and FAR. In order to compare the pulsations driven by sharp increase and sharp decrease of P_{sw}, we plot together the PSDs of H and D components at NUR and CRK during two intervals (0901-0908 UT and 0912-0924 UT) in Fig.4.15.

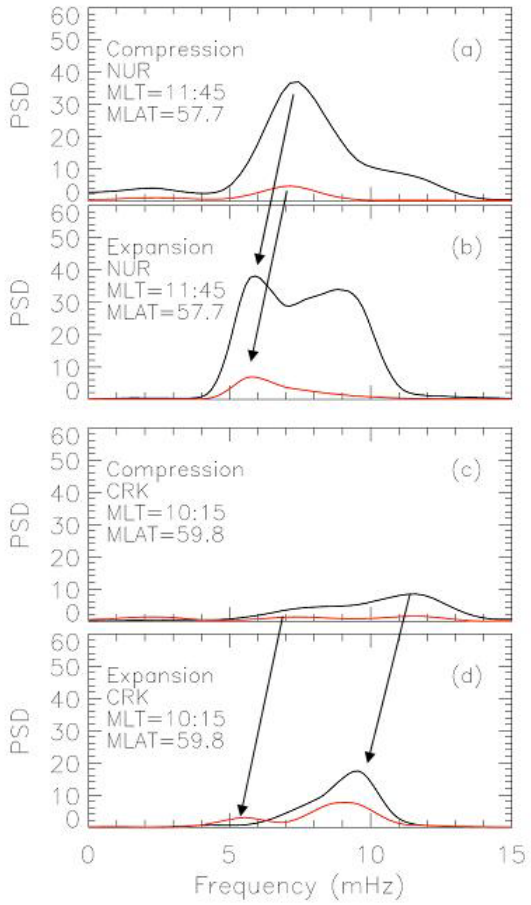

Fig.4.15 PSDs of H (black) and D (red) components at NUR and CRK during two intervals (0901-0908 UT and 0912-0924 UT) on 24 August 2005.

As seen in Fig.4.15, the shapes of PSDs of H and D components of the pulsations driven by magnetospheric compression and expansion are very similar. However the peak frequencies of PSDs of pulsations driven by magnetospheric compression are larger than those driven by magnetospheric expansion. At NUR, the peak frequencies of PSDs of pulsations driven by magnetospheric compression and expansion are 7.2 mHz and 5.8 mHz respectively. At CRK, these two frequencies are 11.6 mHz and 9.5 mHz respectively. The ratios of the PSD peak frequency of pulsation driven by magnetospheric compression to that of pulsation driven by magnetospheric expansion at NUR and CRK are almost the same (1.24 at NUR and 1.22 at CRK). This means that the expansion of magnetosphere make the resonant

frequency of magnetospheric cavity/waveguide at different magnetic local times decrease by the same factor.

The above results indicate that the resonant frequencies of magnetospheric cavity/waveguide are dependent on solar wind parameters. When the magnetosphere is compressed by the sharp increase of solar wind dynamical pressure and the magnetospheric cavity becomes small (the subsolar standoff distance of magnetopause decreases from 6.94 to 6.10 R_E), the resonant frequency of cavity/waveguide increases. In contrast, when the magnetosphere expands due to sharp decrease of solar wind dynamical pressure and the magnetospheric cavity becomes large (the subsolar standoff distance of magnetopause increases from 6.11 to 6.82 R_E), the resonant frequency of cavity/waveguide decreases.

4.3 Discussion

In Section 4.2 we analyze the latitudinal distributions of characteristics of pulsations around three magnetic local times (1700MLT, 1000MLT and 1200 MLT). The reversal of polarizations between two auroral latitude stations, larger PSD close to resonant latitude and increasing frequency with decreasing latitude indicates that the observed pulsations are associated with field line resonance. The results presented in Fig.4.9-Fig.4.14 also show that at the same magnetic local time, the pulsations at different latitudes basically have the same frequency features. Therefore the PSDs of H and D at different magnetic local times in Fig.4.8 give out the magnetic local time distribution of frequencies of pulsations driven by negative solar wind dynamical pressure impulse. From Fig.4.8, we can infer that the pulsations at all local times have a fundamental resonant frequency between 4.3-5.8 mHz. This fundamental frequency is largest on the noon side. Besides in the daytime sector, there exist second harmonic mode waves whose frequencies are around 10 mHz. The second harmonic waves are heavily attenuated on the dawn, dusk and night sides (see Fig.4.8a, b, f and g).

The field line theory can well explain the above observations. The sharp decrease of solar wind dynamical pressure causes an expansion of the magnetosphere. The outward motion of magnetopause then produces a rarefactional wave of the compressional mode [*Sato et al.*, 2001]. This compressional mode wave excites global cavity/waveguide mode wave which oscillate at the eigenfrequencies of magnetospheric cavity. The cavity is radially bounded by the magnetopause on one side and the turning points of compressional wave (i.e., the inner boundary) on the other side [*Kivelson et al.*, 1984]. The cavity mode compressional waves stand radially, but propagate azimuthally [*Samson et al.*, 1992]. The inner boundary allows the energy to leak out of the cavity. The evanescent compressional waves can couple to the field line resonance at points where their frequencies match the field line eigen frequencies. Therefore on the ground, a global pulsation at about 5 mHz is observed. Since the tail is open and the waves are lost in the tail, the pulsations at night stations VIC are very weak. Since the size of cavity is local time dependent and is usually smallest on the noon, the fundamental resonant frequency is largest on the noon.

Note that the incoming rarefactional wave used to be a wide band source. Thus on the dayside, it is possible to observe second harmonic mode pulsations if the second harmonic frequency is inside the wide band. The attenuation of second harmonic mode wave on the dawn, dusk and night sides are possibly related with the accessibility of incoming compressional waves in the magnetosphere. Therefore the disappearance of second harmonic reported here indicate that the second harmonic part of incoming ULF waves cannot penetrate into the magnetosphere as deep as the fundamental part.

4.4 Conclusions

In this work using the geomagnetic field data from 15 ground stations and the data from Geotail, TC-1 and TC-2, we studied the global geomagnetic pulsations at subauroral and auroral latitudes driven by the sharp decrease of solar wind dynamic

pressure on 24 August 2005. The sharp decrease solar wind dynamical pressure can excite global pulsations at subauroral and auroral latitudes. The analysis of PSDs and polarizations of pulsations indicate the pulsations are related with Field Line Resonance. The compressional mode waves needed for exciting FLR in the magnetosphere are from the rapid expansion of magnetosphere rather than from the K-H instability at the magnetosphere because the observed pulsations are strongest not on the dawn and dusk flanks but on the magnetic local noon.

The fundamental resonant frequency, which is between 4.3-5.8 mHz, is magnetic local time dependent and largest around magnetic local noon. This feature is due to the fact that the size of magnetospheric cavity is local time dependent and smallest on the noon side. A second harmonic wave at about 10 mHz is also observed, which is strongest in the daytime sector, and is heavily attenuated in the dawn and dusk sectors. The comparison between the pulsations driven by sharp increase and sharp decrease of P_{sw} shows that the peak frequencies of PSDs of pulsations driven by magnetospheric compression are larger than those driven by magnetospheric expansion, as indicating that the frequencies of pulsations are closely dependent on the size of magnetosphere.

Conclusions et perspectives

Les satellites Cluster et Double Star TC1 fournissent une bonne opportunité d'étudier la dynamique de la magnétosphère. En examinant les spectrogrammes énergie-temps des ions enregistrés par l'instrument CIS de Cluster, nous avons trouvé une structure spécifique de flux d'énergie qui apparaît de façon répétée dans la couche de plasma proche de la terre et dans le courant annulaire. Après l'examen approfondi des caractéristiques de ces structures de flux et en utilisant différentes méthodes d'analyse (analyse des ondelettes, analyse de gyrophase, calculs analytiques et simulations), nous concluons que la structure des flux est due aux accélérations non adiabatiques des ions associées aux fluctuations du champ magnétique.et de plus ce résultat montre que les ondes accélèrent les ions non adiabatiquement près de la Terre. Les caractéristiques de ces structures de flux peuvent être résumées ainsi:

(1) Décroissance brutale des flux (appelée 'trous de flux") de 10 eV-20 keV dans le spectrogramme énergie-temps des ions.

(2) Dans les trous de flux, des ions entre 500 eV-5 keV sont présents (appelés "ions sporadiques"). Ces ions sporadiques ont un angle d'attaque entre 130° et 180° et des phases de gyration en groupe.

(3) Le flux différentiel des protons de plus grandes énergies (28-92 keV) augmente en même temps.

(4) Des ondes électromagnétiques cyclotroniques ioniques (EMIC) près des girofréquences des H^+ et des He^+ accompagnent les variations de flux des ions.

Les explications des observations sont résumées ainsi: des ondes à large bande de fréquence sont générées pendant la phase de dipolarisation en raison des instabilités dans la couche de plasma. Les champs électriques impulsifs induits par les fluctuations du champ magnétique près de la gyrofréquence des ions violent le premier invariant adiabatique des ions dans la couche de plasma. Par conséquent les ions sont accélérés à des énergies plus grandes laissant une structure "trou d'énergie"

dans la gamme 10 eV-20 keV et en même temps le flux des ions dans la gamme d'énergie 28-92 keV augmente. Les ions sporadiques dans le "trou d'énergie" sont accélérés depuis les énergies plus faibles. Leurs angles d'attaque et leurs phases de gyration sont bien en accord avec ce que l'on attend de la théorie de l'accélération non adiabatique.

Une autre recherche dans cette thèse est aussi liée à l'activité des ondes, mais survenant dans le champ géomagnétique, qui sont enregistrées par les magnétomètres dans les stations au sol. Différentes des ondes dans la queue magnétique, les pulsations géomagnétiques sont plus fortement contrôlées par l'interaction du vent solaire avec la magnétopause. En utilisant des stations au sol à différents temps locaux et différentes latitudes et des données de satellites à la fois à la magnétopause et dans la magnétosphère interne, nous étudions les distributions de fréquence globales des pulsations géomagnétiques déclenchées par la décroissance brutale de la pression dynamique du vent solaire. Dans l'analyse des ondes de densité spectrale de puissance et des polarisations, on trouve que les pulsations géomagnétiques ont les caractéristiques suivantes:

(1) La fréquence résonante fondamentale, qui est entre 4,3-5,8 mHz dépend du temps magnétique local et est maximale autour du midi local magnétique.

(2) Une autre onde (harmonique) est aussi observée à environ 10 mHz, onde qui est la plus forte dans le secteur du matin et est très atténuée dans les secteurs aube et crépuscule.

(3) Les polarisations des pulsations entre 2 stations de latitudes aurorales au même temps local sont opposées; les densités spectrales de puissance près de la latitude résonante sont plus grandes; et la fréquence augmente lorsque la latitude diminue.

(4) La comparaison entre les pulsations déclenchées par augmentation brutale ou diminution brutale de P_{sw} (P_{sw} varie d'environ 40 nPa en 5 minutes) montre que le pic de fréquences dans la densités spectrales de puissance déclenchées par compression

magnétosphérique sont plus grandes que celles déclenchées par expansion magnétosphérique.

Les explications correspondantes pour les caractéristiques des pulsations géomagnétiques sont les suivantes: Les caractéristiques de la fréquence résonante fondamentale montrent que la dimension de la cavité magnétosphérique dépend du temps local et est la plus petite du côté midi. Les pulsations d'harmonique sont observées car sa fréquence se trouve dans la bande large des ondes de raréfaction arrivant à la magnétopause, et leur atténuation aux côtés aube, crépuscule et nuit indique que la partie harmonique des ondes UBF arrivant ne peut pas pénétrer dans la magnétosphère aussi profondément que la partie fondamentale. L'inversion des polarisations entre deux stations de latitudes aurorales, de plus grande densité spectrale de puissance près de la latitude de résonance et la fréquence augmentant avec la diminution de la latitude indiquent que les pulsations sont associées avec la résonance de ligne de champ (FLR). Les ondes de compression nécessaires pour exciter la FLR dans la magnétosphère viennent de l'expansion rapide de la magnétosphère plutôt que de l'instabilité K-H à la magnétosphère car les pulsations observées sont les plus intenses non pas sur les flancs aube et crépuscule mais au midi local magnétique. En outre, puisque la FLR est excitée par compression de la cavité/ondes de guide d'onde, les résultats ci-dessus indiquent que la fréquence de résonance dans la cavité magnétosphérique/guide d'onde est due non seulement aux paramètres du vent solaire mais aussi au temps magnétique local du point d'observation. Les variations de fréquence des pulsations dues à l'augmentation brutale et à la décroissance brutale de P_{sw} indiquent en outre que les fréquences des pulsations sont étroitement dépendantes des dimensions de la magnétosphère.

Les activités des ondes dans la magnétosphère sont un sujet fondamental de science spatiale, les instabilités de MHD reliées et les interactions ondes-particules sont importantes pour comprendre la dynamique et le processus de transformation de l'énergie dans la magnétosphère. Bien que nos études aient donné des résultats intéressants, il y a encore des questions auxquelles il faudrait répondre.

(1) La structure spécifique en énergie du flux des ions a aussi été observée dans le sud de la couche de plasma mais avec des caractéristiques différentes de celle observée dans le nord de la couche de plasma telles que (1) les ions sporadiques dans les trous d'énergies n'étaient pas visibles et (2) la densité spectrale de puissance (PSD) des fluctuations du champ magnétique n'était pas dominante dans les composantes toroïdales et poloïdales, mais distribuée également entre les 3 composantes. Comme ceci n'est pas un cas isolé, les caractéristiques différentes des ondes devraient être expliquées. Si ce n'est pas à cause de la transformation de mode d'onde entre les deux côtés de la couche de plasma; il devrait y avoir des mécanismes différents d'excitation des ondes. Nous prévoyons de faire plus de recherche sur ce point.

(2) La frontière entre partie ouverte et partie fermée (OCB) dans la magnétosphere est une séparation entre les lignes de champ magnétique ouvertes aux hautes latitudes des lignes de champ plus fermées aux latitudes plus basses. Du côté jour la frontière est toujours identifiée vers le pôle par la limite de piégeage des electrons énergétiques (quelques keV) piégés sur les lignes de champ magnétique fermées (*Evans and Stone*, 1972). Alors que du côté nuit cette limite de piégeage marque la separation entre les lignes de champ magnétique dipolaires et étirées, et aussi correspond à la frontière entre les aurores diffuses et les aurores discrètes dans l'ionosphère. Quand l'accélération non adiabatique survenaient dans les évènements précédents, nous avons été surpris de trouver que les satellites étaient toujours localisés à la limite de la frontière de piégeage des electrons de quelques keV. C'est probablement parce que l'accélération non adiabatique se produit toujours pendant la dipolarisation quand les electrons piégés bougent avec les lignes de champ dépolarisé et rencontre les satellites (voir Fig. 4.16). Nous prévoyons de démontrer la relation entre les fluctuations du champ magnétique, la dipolarisation magnétosphérique, les variations des flux en énergie des ions et la frontière de piégeage des electrons.

(3) Comme il a été vu dans cette étude, les ondes jouent un rôle significatif sur les variations des flux des ions; cependant nous n'avons pas encore une connaissance claire de l'origine et du mécanisme de génération des ondes (spécialement les ondes

EMIC). On devrait vérifier si les structures caractéristiques des flux permettent encore de reconnaître le processus dynamique non adiabatique dans d'autres régions de la magnétosphère, si les électrons peuvent être accélérés de la même façon non adiabatique que les ions.

(4) En plus des impulsions de pression dynamique du vent solaire, la rotation du champ magnétique interplanétaire peut aussi déclencher les pulsations géomagnétiques. Dans une autre étude de cas, une série d'impulsions Pi2 a été observée par les stations au sol de moyennes latitudes du côté jour. Chacune des impulsions géomagnétiques débute en même temps qu'une rotation du champ magnétique interplanétaire est observée par Geotail près de la magnétopause. Ces bonnes corrélations impliquent que la rotation du champ magnétique interplanétaire peut stimuler les impulsions géomagnétiques. Ce processus physique devra être expliqué en détail.

Finalement, nous continuerons nos recherches pour avoir une meilleure connaissance des sujets traités dans cette thèse, en utilisant davantage de moyens au sol et dans l'espace.

Conclusions and perspectives

The Cluster and Double Star TC-1 spacecraft supply a good opportunity to study the dynamic of the magnetosphere. When examining the energy-time spectrogram of ions recorded by the Cluster CIS instrument, we found a specific energy flux structure of ions repeatedly appearing in the near-Earth plasma sheet/ring current. After careful examinations of the characteristics of these energy flux structures and deep investigations on the background field/plasma situations through various methods (wavelet analysis, gyrophase analysis, analytic computations and simulations), we conclude that the energy flux structure is formed by the ion nonadiabatic accelerations associated with the magnetic field fluctuations. The characteristics of the energy flux structures can be summarized as follows:

(1) Abrupt energy flux decrease (referred to as the 'energy flux holes') over 10 eV-20 keV in the energy-time spectrogram of ions.

(2) Inside the energy flux holes, scatted some ions over 500 eV-5 keV (referred to as the 'sporadic ions'). These sporadic ions have a pitch angle between 130° and 180° and bunched gyration phases.

(3) The proton differential flux in higher energy (28-92 keV) increase at the same time.

(4) ElectroMagnetic Ion Cyclotron (EMIC) waves near the gyrofrequencies of H^+ and He^+ accompany the ion energy flux variations.

The explanations for the observations are summarized as: broadband frequency waves are stimulated during dipolarization phase due to the instabilities in the plasma sheet. The impulsive electric fields induced by the magnetic field fluctuations near ion gyrofrequencies violate the first adiabatic invariant of ions in the plasma sheet. Consequently the ions are accelerated up to higher energy, leaving an 'energy flux hole' structure over 10 eV-20 keV and at the same time making the ion fluxes in higher energy (28-92 keV) increase. The sporadic ions inside the 'energy flux hole'

are accelerated from lower energy. Their pitch angles and gyration phases both agree well with the expectations from the nonadiabatic acceleration theory.

Another research in this doctoral dissertation is also related to wave activities, but occurring in the geomagnetic field, which are monitored by the magnetometers at the ground stations. Different from waves in the magnetotail, the geomagnetic pulsations are more highly controlled by the interaction of solar wind with the magnetopause. By using ground stations at different magnetic local times and latitudes, and data from spacecraft both at the magnetopause and in the inner magnetosphere, we investigate the global frequency distributions of geomagnetic pulsations driven by the sharp decrease of solar wind dynamic pressure. Through the wave analysis of PSDs and polarizations, it is found that the geomagnetic pulsations have characteristics as follows:

(1) The fundamental resonant frequency, which is between 4.3-5.8 mHz, is magnetic local time dependent and largest around magnetic local noon.

(2) A second harmonic wave at about 10 mHz is also observed, which is strongest in the daytime sector, and is heavily attenuated in the dawn and dusk sectors.

(3) The polarizations of pulsations between two auroral latitude stations at the same local time are reversed; the Power Spectral Densities (PSDs) close to resonant latitude are larger; and the frequency increases with decreasing latitude.

(4) The comparison between the pulsations driven by sharp increase and sharp decrease of P_{sw} (P_{sw} varied about 40 nPa in 5 minutes) shows that the peak frequencies of PSDs of pulsations driven by magnetospheric compression are larger than those driven by magnetospheric expansion.

The corresponding explanations for the characteristics of the geomagnetic pulsations are given as: The features of the fundamental resonant frequency indicate the fact that the size of magnetospheric cavity is local time dependent and smallest on the noon side. The second harmonic mode pulsations are observed because the second harmonic frequency is inside the wide band of the incoming rarefactional waves at the

magnetopause, and their attenuation at the dawn, dusk and night sides indicate the second harmonic part of incoming ULF waves cannot penetrate into the magnetosphere as deep as the fundamental part. The reversal of polarizations between two auroral latitude stations, larger Power Spectral Density (PSD) close to resonant latitude and increasing frequency with decreasing latitude indicate that the pulsations are associated with Field Line Resonance (FLR). And the compressional mode waves needed for exciting FLR in the magnetosphere are from the rapid expansion of magnetosphere rather than from the K-H instability at the magnetosphere because the observed pulsations are strongest not on the dawn and dusk flanks but on the magnetic local noon. Besides, since the FLR is excited by compressional cavity/waveguide waves, the above results indicate that the resonant frequency in the magnetospheric cavity/waveguide is decided not only by solar wind parameters but also by magnetic local time of the observation point. The frequency variations of the pulsations driven by sharp increase and sharp decrease of P_{sw} further indicate that the pulsation frequencies are closely dependent on the size of magnetosphere.

Wave activities in the magnetosphere are a fundamental subject of the space physics. The related MHD instabilities and the wave-particle interactions are significant for the understanding of the dynamics and the energy transformation process in the magnetosphere. Although our studies have given some interesting results, there are still questions to be resolved.

(1) The specific energy flux structure of ions was also observed by Cluster in the south of the plasma sheet, but has different characteristics with the one observed in the north of the plasma sheet, such as (1) the sporadic ions inside the energy flux holes did not show up and (2) the PSDs of the magnetic field fluctuations were not dominant in the toroidal and poloidal components, but equally distributed in the three components. As this is not just an isolated case, the different wave features should be explained. If it is not due to the wave mode transformation between the two sides of the plasma sheet, there should be other wave exciting mechanisms. We plan to make a further research about this issue.

(2) The open-closed boundary (OCB) in the magnetosphere is a demarcation which separates the open magnetic field lines at higher latitudes from more closed field lines at lower latitudes. In the day side, the OCB is always indentified by the poleward boundary of high energy electron (a few keV) trapped on closed magnetic field lines (*Evans and Stone*, 1972). While in the nightside, this trapping boundary marks the demarcation between dipolar and stretched magnetic field lines, and also corresponds to the boundary between diffuse and more discrete aurora in the ionosphere. When the nonadiabatic acceleration occurred in the previous events, we were surprised to find that the spacecraft were always located at the edge of the several keV electron trapping boundary. It is probably because that the nonadiabatic acceleration always occurs during dipolarization when the trapped electrons co-move with the dipolarized field lines and encounter with the spacecraft (see Fig.4.16). We plan to make sure the relationship between the magnetic field fluctuations, magnetospheric dipolarization, ion energy flux variations and the electron trapping boundary, etc..

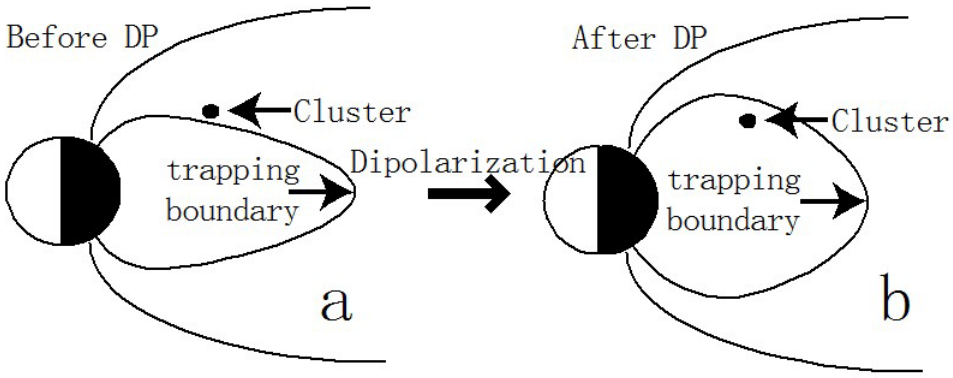

Fig.4.16 Schematic diagrams to illustrate the encounter of the spacecraft and the electrons trapping boundary during magnetospheric dipolarization. The Cluster spacecraft are indicated by the black circle dot.

(3) As already seen above in the study, the fluctuations in magnetic field play a significant role for the energy flux variations of ions, however, we still have no clear knowledge of the origin and generation mechanism of the fluctuations (especially the EMIC waves). And it should be verified whether the characteristic energy flux structures still validate as a proxy to recognize the nonadiabatic dynamic process in

other regions of the magnetosphere, whether the electrons can be accelerated in the same non-adiabatic way as the ions.

(4) Beside the solar wind dynamic pressure pulses, the interplanetary magnetic field rotation can also trigger the geomagnetic pulsations. We find in another case study that a series of Pi2 pulses are observed by the dayside mid-latitude ground stations and each of the geomagnetic pulses starts at the same time with an interplanetary magnetic field rotation observed by Geotail near the magnetopause. The good correlations imply the interplanetary magnetic field rotation might stimulate the geomagnetic pulses. This physical process will be explained in detail.

In the end, we look forward to make better knowledge of the subjects mentioned in the thesis, based on more detections both on ground and in space.

References

Allan, W., White, S. P., and Poulter, E. M.: Impulse-excited hydromagnetic cavity and field-line resonances in the magnetosphere, Planet. Space Sci., 34, 371–385, 1986.

Anderson, B. J., and Fuselier, S. A.: Response of thermal ions to electromagnetic ion cyclotron waves, *J. Geophys. Res.*, 99(A10), 19,413-19,425, 1994.

Andréeová, K., Pulkkinen, T. I., Laitinen, T. V., and Přech, L.: Shock propagation in the magnetosphere: Observations and MHD simulations compared, J. Geophys. Res., 113, A09224, doi:10.1029/2008JA013350, 2008.

Araki, T.: A physical model of the geomagnetic sudden commencement, in Solar Wind Sources of Magnetospheric Ultra-Low-Frequency Waves, Geophys. Monogr. Ser., vol. 81, edited by M. J. Engebretson, K. Takahashi, and M. Scholer, p. 183, AGU, Washington, D. C., 1994.

Baker, Gregory J., Donovan, E. F., and Jackel, Brian J.: A comprehensive survey of auroral latitude Pc5 pulsation characteristics, J. Geophys. Res, 108A10, 1384, doi:10.1029/2002JA009801, 2003.

Balogh, A., et al.: The Cluster magnetic field investigation: Overview of in-flight performance and initial results, *Ann. Geophys., 19*, 1207–1217, 2001.

Baumjohann, W. and Treumann, Rudolf A.: Basic space plasma physics, Imperial College Press, London, 1996.

Birn, J., and M. Hesse: Particle Acceleration in the Dynamic Magnetotail: Orbits in Self-Consistent Three-Dimensional MHD Fields, *J. Geophys. Res.*, 99(A1), 109–119, doi:10.1029/93JA02284, 1994.

Bogdanova, Y. V., et al.: Correlation between suprathermal electron bursts, broadband extremely low frequency waves, and local ion heating in the midaltitude

cleft/low-latitude boundary layer observed by Cluster, *J. Geophys. Res., 109*, A12226, doi:10.1029/2004JA010554, 2004.

Borodkova N. L., et al.: Geosynchronous magnetic field response to the large and fast solar wind dynamic pressure change, Adv. Space Res., 41(8), 1220-1225, 2008.

Büchner, J., and Zelenyi, L. M.: Regular and chaotic charged particle motion in magnetotail like field reversals: 1. Basic theory of trapped motion, *J. Geophys. Res.*, 94, 11,821-11,824, 1989.

Chen, L., and Hasegawa, A.: A theory of long period magnetic pulsations 1. Steady state excitation of field line resonaces, J. Geophys. Res., 79, 1024-1037, 1974a.

Chen, L., and Hasegawa, A.: A theory of long period magnetic pulsations 2. Impulse excitations of surface eigenmode, J. Geophys. Res., 79, 1024-1037, 1974b.

Chen, J., and Palmadesso, P. J.: Chaos and Nonlinear Dynamics of Single-Particle Orbits in a Magnetotaillike Magnetic Field, *J. Geophys. Res., 91*, A2, 1499–1508, 1986.

Chen, J., Burkhart, G. R., et al.: Observational signatures of nonlinear magnetotail particle dynamics, *Geophys. Res. Lett., 17*, 12, 2237-2240, 1990.

Christon, S. P., et al.: Spectral characteristics of plasma sheet ion and electron populations during disturbed geomagnetic conditions, *J. Geophys. Res., 96*, 1–22, doi:10.1029/90JA01633, 1991.

Coco, J., E. Amata, M. F. Marcucci, D. Ambrosino, J. P. Villain, and C. Hanuise: The effects of an interplanetary shock on the high-latitude ionospheric convection during an IMF By -dominated period, Annales Geophysicae, 26. 9. 2937–2951, 2008.

Cornilleau-Wehrlin, N., et al.: The Cluster Spatio-Temporal Analysis of Field Fluctuations (STAFF) Experiment, Space Science Reviews, 79, 107–136, 1997.

Daglis, I. A., Thorne, R. M., Baumjohann, W., and Orsini, S.: The terrestrial ring current: Origin, formation and decay, Rev. Geophys., 37, 407–438, doi:10.1029/1999RG900009, 1999.

Dandouras, I., H. Rème, J. B. Cao, P. Escoubet: Magnetosphere response to the 2005 and 2006 extreme solar events as observed by the Cluster and Double Star spacecraft, Adv. Space Res., 43(4), 618-623, 2009.

Décréau, P. M. E., et al.: Whisper, a Resonance Sounder and Wave Analyzer: Performances and Perspectives for the Cluster Mission, Space Science Reviews, 79, 157–193, 1997.

Delcourt, D. C., Sauvaud, J. A., and Pedersen, A.: Dynamics of simple-particle orbits during substorm expansion phase, *J. Geophys. Res.*, *95*, 20,853– 20,865, doi:10.1029/JA095iA12p20853, 1990.

Delcourt, D. C., and Moore, T. E.: Precipitation of ions induced by magnetotail collapse, *J. Geophys. Res.*, *97*, 6405, 1992.

Delcourt, D. C., Martin Jr., R. F.: Application of the centrifugal impulse model to particle motion in the near-Earth magnetotail, *J. Geophys. Res., 99*, 23,583-23,590, 1994.

Delcourt, D. C., and Sauvaud, J. A.: Plasma sheet ion energization during dipolarization events, *J. Geophys. Res., 99*, 97-108, 1994.

Delcourt, D. C., Martin Jr., R. F., and Alem, F.: A simple model of magnetic moment scattering in a field reversal, *Geophys. Res. Lett., 21*, 1543, 1994.

Delcourt, D. C., Sauvaud, J. A., and Moore, T. E.: Phase bunching during substorm dipolarization, *J. Geophys. Res., 102*, 24,313–24,324, doi:10.1029/97JA02039, 1997.

Dungey, J. W.: Electrodynamics of the outer atmosphere, Vol.69 of Ionosphere Research Laboratory Science Report, Pennsylvania State University, Pennsylvania, 1954.

Eastman T. E., R. R. Anderson, AND L. A. Frank, Upstream Particles Observed in the Earth's Foreshock Region, *J. Geophys. Res., VOL. 86*, NO. A6, PAGES 4379-4395, JUNE 1, 1981.

Engebretson, M. J., et al.: Pc1-Pc2 waves and energetic particle precipitation during and after magnetic storms: Superposed epoch analysis and case studies, *J. Geophys. Res., 113*, A01211, doi:10.1029/2007JA012362, 2008.

Erlandson, R. E., et al.: Observations of solar wind pressure initiated fast mode waves at geostationary orbit and in the polar cap, J. Atmos. Terr. Phys., 53, 231–239, 1991.

Escoubet C. P., Fehringer, M., and Goldstein M.: The Cluster mission, *Ann. Geophys., 19*, 1197–1200, 2001.

Evans, L. C. And Stone, E. C.: Electron polar cap and the boundary of open geomagnetic field lines, J. Geophys. Res., 77, 5580–5585, 1972.

Farrugia, C. J., et al.: Pressure driven magnetopause motions and attendant response on the ground, Planet. Space Sci., 37, 589-607, 1989.

Fraser, B. J., et al.: Storm time observations of electromagnetic ion cyclotron waves at geosynchronous orbit: GOES results, *J. Geophys. Res., 115*, A05208, doi:10.1029/2009JA014516, 2009.

Fuselier S. A., M. F. Thomsen, S. P. Gary, S. J. Bame, C. T. Russell and G. K. Parks: The Phase Relationship Between Gyrophase-Bunched Ions And MHD-Like Waves, *Geophys. Res. Lett., VOL. 13*, NO. 1, PAGES 60-63, JANUARY, 1986.

Fuselier, S. A., and Anderson B. J.: Low-energy He^+ and H^+ distributions and proton cyclotron waves in the afternoon equatorial magnetosphere, *J. Geophys. Res., 101(A6)*, 13,255-13,265, 1996.

Gurnett, D. A., R. L. Huff, and D. L. Kirchner: The Wide-Band Plasma Wave Investigation, *Space Science Reviews*, 79, 195–208, 1997.

Gurgiolo, C., G.K. Parks, B. H. Mauk and C.S. Lin: Non-ExB Ordered Ion Beams Upstream of the Earth's Bow Shock, *J. Geophys. Res., VOL. 86*, NO. A6, PAGES 4415-4424, JUNE 1, 1981.

Gustafsson, G., et al.: First results of electric field and density observations by Cluster EFW based on initial months of operation, *Ann. Geophys., 19*, 1219–1240, 2001.

Harrold, B. G. and Samson, J. C.: Standing ULF modes of the magnetosphere: a theory, *Geophys. Res. Lett., 19*, 1811–1814, 1992.

Hughes, W. J.: Magnetospheric ULF waves: A tutorial with a historical perspective, in Solar Wind Sources of Magnetospheric ULF Waves, Geophysical Monogr. Ser., vol. 81, (Eds.) Engebretson, M. J., Takahashi, K., and Scholer, M., 1–11, AGU, Washington, D.C., 1994.

Johnstone, A. D., C. Alsop, S. Burge, P. J. Carter, A. J. Coates, A. J. Coker, A. N. Fazakerley, M. Grande, R. A. Gowen, C. Gurgiolo, B. K. Hancock, B. Narheim, A. Preece, P. H. Sheather, J. D. Winningham and R. D. Woodliffe: PEACE: A Plasma Electron and Current Experiment, Space Sci. Rev., 79, 351-398, 1997.

Jordanova, V. K., et al.: Relativistic electron precipitation by EMIC waves from self-consistent global simulations, *J. Geophys. Res., 113*, A00A10, doi:10.1029/2008JA013239, 2008.

Keika, K., et al.: Response of the inner magnetosphere and the plasma sheet to a sudden impulse, J. Geophys. Res., 113, A07S35, doi:10.1029/2007JA012763, 2008.

Kennel, C. F., and Petschek, H. E.: Limit on stably trapped particle fluxes, *J. Geophys. Res.*, 71, 1-27, 1966.

Kepko, L., et al.: ULF Waves in the Solar Wind as Direct Drivers of Magnetospheric Pulsations, Geophys. Res. Lett., 29(8), 1197-1200, 2002.

Kim, K.-H., et al., Magnetospheric responses to sudden and quasiperiodic solar wind variations, J. Geophys. Res., 107(A11), 1406, doi:10.1029/ 2002JA009342, 2002.

Kivelson, M.G., J. Etcheto, and J.G. Trotignon, Global compression oscillations of the terrestrial magnetosphere: The evidence and a model, J. Geophys. Res., 89, 9851, 1984.

Kivelson, M. G., Etcheto, J., and Trotignon, J. G.: Global compressional oscillations of the terrestrial magnetosphere: the evidence and a model, J. Geophys. Res., 89, 9851–9856, 1984.

Kivelson, M. G. and Southwood, D. J.: Resonant ULF waves: A new interpretation, Geophys. Res. Lett., 12, 49–52, 1985.

Kivelson, M. G. and Southwood, D. J.: Coupling of global magnetospheric MHD eigenmodes to field line resonances, J. Geophys. Res., 91, 4345–4351, 1986.

Kivelson, Margaret G. and Russell, Christopher T.: Introduction to space physics, Cambridge University Press, New York, 1995.

Korotova G. I., and D. G. Sibeck, Generation of ULF magnetic pulsations in response to sudden variations in solar wind dynamic pressure, in Solar Wind Sources of Magnetospheric Ultra-Low-Frequency Waves, pp. 265-271, American Geophysical Union, 1994.

Koskinen, Hannu E. J.: Energetic particle losses from the inner magnetosphere: The inner magnetosphere: physics and modeling, *Geophysical Monograph Series*, 155, 318 PP., 2005.

Lee, D.-H. and Lysak, R. L.: Impulsive excitation of ULF waves in the three-dimensional dipole model: the initial results, J. Geophys. Res., 96, 3479–3486, 1991a.

Lee, D.-H. and Lysak, R. L.: Monochromatic ULF wave excitation in the dipole magnetosphere, J. Geophys. Res., 96, 5811–5817, 1991b.

Lee, D.-H. and Lysak, R. L.: Magnetospheric ULF wave coupling in the dipole field: the impulsive excitation, J. Geophys. Res., 94, 17 097–17 103, 1989.

Lee, D.-Y., and L. R. Lyons, Geosynchronous magnetic field response to solar wind dynamic pressure pulse. J. Geophys. Res. 109, A04201, doi:10.1029/2003JA010076, 2004.

Li, X., et al.: Energetic particle injections in the inner magnetosphere as a response to an interplanetary shock, J. Atmos. Sol. Terr. Phys., 65, 233–244, 2003.

Lin, R. L., X. X. Zhang, S. Q. Liu, Y. L. Wang, and J. C. Gong, A three-dimensional asymmetric magnetopause model, J. Geophys. Res., 115, A04207, doi:10.1029/2009JA014235, 2010.

Liu, Z. X., Escoubet, C. P., Pu, Z., Laakso, H., Shi, J. Q., Shen, C., and Hapgood, M.: The Double Star mission, Ann. Geophys., 23, 2707–2712, 2005.

Lui, A. T. Y., McEntire, R. W., Krimigis, S. M., and Keath, E. P.: Acceleration of energetic oxygen (E > 137 keV) in the storm-time ring current, in Ion Acceleration in the Magnetosphere and Ionosphere, Geophys. Monogr. Ser., 38, 149, 1986.

Lui, A. T. Y., et al.: A case study of magnetotail current sheet disruption and diversion, *Geophys. Res. Lett.*, *15*, 721-724, doi:10.1029/GL015i007p00721, 1988.

Lui, A. T. Y.: Current controversies in magnetospheric physics, Rev. Geophys., 39, 535, 2001.

Lysak, R. L., and Lee, D.: Response of the dipole magnetosphere to pressure pulses, Geophys. Res. Lett., 19(9), 937– 940, 1992.

Lysak, R. L., Y. Song, and Lee, D.: Generation of ULF waves by fluctuations in the magnetopause position, in Solar Wind Sources of Magnetospheric ULF Waves, Geophys. Monogr. Ser., vol. 81, edited by M. J. Engebretson, K. Takahashi, and M. Scholer, pp. 273– 281, AGU, Washington, D. C, 1994.

Mauk, B. H.: Quantitative modeling of the "convection surge" mechanism of ion acceleration, *J. Geophys. Res.*, *91*, 13,423-13,431, 1986.

Mead, G. D., and Fairfield, D. H.: A quantitative magnetospheric model derived from spacecraft magnetometer data, *J. Geophys. Res.*, *80*, 523, 1975.

Mishin, V. V.,:Accelerated motions of the magnetopause as a trigger of the Kelvin-Helmholtz instability, J. Geophys. Res., 98, 21365-21371, 1993.

Nosé, M., Ohtani, S., Lui, A. T. Y., Christon, S. P., McEntire, R. W., Williams, D. J., Mukai, T., Saito, Y., and Yumoto, K.: Change of energetic ion composition in the plasma sheet during substorms, *J. Geophys. Res.*, *105*, 23,277– 23,286, doi:10.1029/2000JA000129, 2000.

Nosé, M., Y. Ono, S. P. Christon, and A. T. Y. Lui, Revisiting the role of magnetic field fluctuations in nonadiabatic acceleration of ions during dipolarization, J. Geophys. Res., 117, A02207, doi:10.1029/2012JA017518, 2012.

Ohtani, S., et al.: Magnetic fluctuations associated with tail current disruption: Fractal analysis, *J. Geophys. Res.*, *100*, 19135-19145, doi:10.1029/95JA00903, 1995.

Ono, Y., Nosé, M., Christon, S. P., and Lui, A. T.: The role of magnetic field fluctuations in nonadiabatic acceleration of ions during dipolarization, *J. Geophys. Res.*, *114*, A05209, doi:10.1029/2008JA013918, 2009.

Otto, A.: The Magnetosphere, *Lecture Notes in Physics, 656,* 943-970, doi:10.1007/978-3-540-31534-6_5, 2005.

Parkhomov, V.A., et al., Long-period geomagnetic pulsations caused by the solar wind negative pressure impulse on 22 March1979 (CDAW-6). Ann. Geophys., 16, 134–139, 1998.

Paschmann, G., et al.: The Electron Drift Instrument for Cluster, Space Science Reviews, 79, 233–269, 1997.

Pedersen, A.: Substorm electric and magnetic field signatures on GEOS 1, GEOS 2, and ISEE 1, in Proceedings of the International Workshop on "Substorms," Eur. Space Agency Spec. Publ., ESA SP-335, 237, 1992.

Pedersen, A., et al.: The Wave Experiment Consortium (wec), Space Science Reviews, 79, 93–106, 1997.

Pedersen, A., et al.: Electron density estimations derived from spacecraft potential measurements on Cluster in tenuous plasma regions. J. Geophys. Res.,113, A07S33, doi:10.1029/2007JA012636, 2008.

Quinn, J. M., and McIlwain, C. E.: Bouncing ion clusters in the Earth's magnetosphere, J. Geophys. Res., 84, 7365, 1979.

Quinn, J. M., and Southwood, D. J.: Observations of parallel ion energization in the equatorial region, *J. Geophys. Res., 87*, 10,536-10,540, 1982.

Rème, H., et al.: The Cluster Ion Spectrometry (CIS) Experiment, Space Science Reviews, 79, 303–350, 1997.

Rème, H., et al.: First multispacecraft ion measurements in and near the Earth's magnetosphere with the identical CLUSTER Ion Spectrometry (CIS) Experiment, *Ann. Geophys., 19*, 1303–1354, 2001.

Rème, H., I. Dandouras, C. Aoustin, J. M. Bosqued, J. A. Sauvaud, C. Vallat, P. Escoubet, J. B. Cao, J. Shi, M. B. Bavassano-Cattaneo, G. K. Parks, C. W. Carlson, Z. Pu, B. Klecker, E. Moebius, L. Kistler, A. Korth, R. Lundin, and the HIA team, The HIA instrument on board the Tan Ce 1 Double Star near-equatorial spacecraft and its first results, Annales Geophysicae, 23, 2757–2774, 2005.

Riedler, W., et al.: Active Spacecraft Potential Control, Space Science Reviews, 79, 271–302, 1997.

Sergeev, V. A., Sazhina, E. M., Tsyganenko, N. A., Lundblad J. A. and F. Soraas: Pitch-angle scattering of energetic protons in the magnetotail current sheet as the dominant source of their isotropic precipitation into the ionosphere, *Planet. Space Sci.*, 31, 1147, 1983.

Samson, J. C., Jacobs, J. A., and Rostoker, G.: Latitude-Dependent Characteristics of Long-Period Geomagnetic micropulsations, J. Geophys. Res., 76, 3675-3683, doi:10.1029/JA076i016p03675, 1971.

Samson, J. C., Harrold, B. G., Ruohoniem, J. M., Greenwald, R. A., and Walker, A. D. M.: Field line resonances associated with MHD waveguides in the magnetosphere, Geophys. Res. Lett., 19, 441–444, 1992.

Samsonov, A. A., Z. Nemecek, and J. Safrankova, Numerical MHD modeling of propagation of interplanetary shock through the magnetosheath, J. Geophys. Res., 111, A08210, doi:10.1029/2005JA011537, 2006.

Sarafopoulos, D. V.: Long duration Pc 5 compressional pulsations inside the Earth's magnetotail lobes, Ann. Geophys., 13, 926–937, 1995.

Sarafopoulos, D. V.: A case study testing the cavity mode model of the magnetosphere, Ann. Geophys., 23, 1867–1880, 2005.

Sato, N., Y. Murata, H. Yamagishi, A. S. Yukimatu, M. Kikuchi, M. Watanabe, K. Makita, H. Yang, R. Liu, and F. J. Rich, Enhancement of optical aurora triggered by the solar wind negative pressure impulse (SI_), Geophys. Res. Lett., 28, 127, 2001.

Shen, C., et al.: Analyses on the geometrical structure of magnetic field in the current sheet based on Cluster measurements, *J. Geophys. Res., 108(45),* 1168, doi:10.1029/2002JA009612, 2003.

Shen, C. and Liu, Z.-X.: Double Star project – master science operations plan, Ann. Geophys., 23, 2851–2859, 2005.

Shen, C., et al.: Magnetic field rotation analysis and the applications, *J. Geophys. Res., 112, A06211*, doi:10.1029/2005JA011584, 2007.

Shue, J.H., et al.: Magnetopause location under extreme solar wind conditions, J. Geophys. Res., 103(A8), 17,691–17,700, doi:10.1029/98JA01103, 1998.

Southwood, D.J., Some features of field line resonances in the magnetosphere, Planet. Space Sci., 22, 483, 1974.

Speiser, T. W.: Particle trajectories in model current sheets, 1, Analytical solutions, *J. Geophys. Res.,* 70, 4219, 1965.

Takeuchi, T., T. Araki, A. Viljanen, and J. Watermann, Geomagnetic negative sudden impulses: Interplanetary causes and polarization distribution, J. Geophys. Res., 107(D7), 1096, doi:10.1029/2001JA900152, 2002

Taylor, J. R., et al.: The response of the magnetosphere to the passage of a coronal mass ejection on March 20-21 1990, Ann. Geophys., 15, 671-684, 1997.

Tamao, T.: Transmission and coupling resonance of hydrodynamic disturbances in the non-uniform Earth's magnetospherer, Sci. Rep. Tohoku Univ., Fifth Ser., 17,43-72, 1965.

Thorne, R. M.: Radiation belt dynamics: The importance of wave-particle interactions, *Geophys. Res. Lett., 37,* L22107, doi:10.1029/2010GL044990, 2010.

Ukhorskiy, A. Y., et al.: Rapid scattering of radiation belt electrons by storm-time EMIC waves, Geophys. Res. Lett., 37, L09101, doi:10.1029/2010GL042906, 2010.

Vontrat-Reberac, A., Cerisier, J.-C., Sato, N., and Lester, M.: Noon ionospheric signatures of a sudden commencement following a solar wind pressure pulse. Ann. Geophys., 20, 639-645, 2002.

Wang, C., et al.: Geospace magnetic field responses to interplanetary shocks, J. Geophys. Res., 114, A05211, doi:10.1029/2008JA013794, 2009.

Wilken, B., C. K. Goertz, D. N. Baker, P. R. Higbie, and T. A. Fritz, The SSC on July 29, 1977 and its propagation within the magnetosphere, J. Geophys. Res., 87, 5901–5910, doi:10.1029/JA087iA08p05901, 1982.

Wilken, B., et al.: RAPID - The Imaging Energetic Particle Spectrometer on Cluster, Space Science Reviews, 79, 399–473, 1997.

Wilken, B., et al.: First results from the RAPID imaging energetic particle spectrometer on board Cluster, Ann. Geophys., 19, 1355–1366, 2001.

Wing, S., Sibeck, D. G., Wiltberger, M., et al., Geosynchronous magnetic field temporal response to solar wind and IMF variations. J. Geophys. Res. 107 (A8), 1222, doi:10.1029/2001JA009156, 2002.

Woolliscroft, L. J. C., et al.: The Digital Wave-Processing Experiment on Cluster, Space Science Reviews, 79, 209–231, 1997.

Zesta, E., and Sibeck, D. G.: A detailed description of the solar wind triggers of two dayside transients: Events of 25 July 1997, J. Geophys. Res., 109, A01201, doi:10.1029/2003JA009864, 2004.

Zhang, J. C., et al.: A case study of EMIC wave-associated He^{+} energization in the outer magnetosphere: Cluster and Double Star 1 observations, *J. Geophys. Res.*,*115*,A06212,doi:10.1029/2009JA014784,2010.

Zhang, X. Y., Q.-G. Zong, Y. F. Wang, H. Zhang, L. Xie, S. Y. Fu, C. J. Yuan, C. Yue, B. Yang, and Z. Y. Pu, ULF waves excited by negative/positive solar wind dynamic pressure impulses at geosynchronous orbit, J. Geophys. Res., 115, A10221, doi:10.1029/2009JA015016, 2010.

Zolotukhina, N., et al., Response of the inner and outer magnetosphere to solar wind density fluctuations during the recovery phase of a moderate magnetic storm, J. Atmos. Sol. Terr. Phys., 69, 1707–1722, 2007.

Zong, Q., et al., Energetic electron response to ULF waves induced by interplanetary shocks in the outer radiation belt, J. Geophys. Res., 114, A10204, doi:10.1029/2009JA014393, 2009.

Publications of Zhiqiang WANG

1. Wang Z. Q., Cao J. B., ULF waves associated with the periodical high speed flows in magnetotail plasma sheet, *Chinese J. Geophys.*, Vol.53, No.1, 2010, 35-41

2. Cao J. B., Wang Z. Q., Ma Y. D., et al. Differences between onset times of bursty bulk flows (BBFs) of two Cluster satellites in the magnetotail. *Sci China Tech Sci*, 2012, 55, doi: 10.1007/s11431-012-4783-z.

3. Cao J. B., Yan C. X.,…, Wang Z. Q. (2010), Geomagnetic signatures of current wedge produced by fast flows in a plasma sheet, *J. Geophys. Res.*, 115, A08205, doi:10.1029/2009JA014891.

4. Zhi-Qiang WANG, Henri Rème, Iannis Dandouras, Jin-Bin Cao, Nonadiabatic acceleration of plasma sheet ions associated with magnetic field fluctuations, *J. Geophys. Res.*. (under review)

5. Jin-Bin CAO, Zhi-Qiang Wang, et al., Global frequency distributions of pulsations driven by sharp decrease of solar wind dynamic pressure, *Ann. Geophys.*. (under review)

Participations of Conferences

1. The 2nd International Space Weather Conference, in Nanjing, China, October 17-21, 2009, (poster)

2. The 7th National Space Weather Symposium, in Shanghai, China, July 27-August 2, 2010, (oral presentation)

3. Conference of ‘ESLAB 2011/Cluster 21’, in Brugge, Belgium, 19-23 September 2011, (poster)